

UNIVERSITY OF THE WESTERN CAPE

A study of the angular momentum content of early-type galaxies

Author:
Unarine Tshiwawa

Supervisor:
Dr E. Elson
Co-supervisor:
Prof. R. Maartens

*A thesis submitted in fulfillment of the requirements
for the degree of M.Sc.*

UNIVERSITY *of the*
in the
WESTERN CAPE

Department of Physics & Astronomy

July 2019

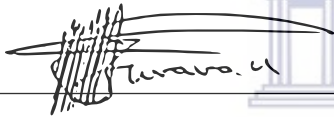


UNIVERSITY *of the*
WESTERN CAPE

Declaration of Authorship

I, Unarine Tshiwawa, declare that this thesis titled, "A study of the angular momentum content of early-type galaxies" and the work presented in it is my own. I confirm that this work submitted for assessment is my own and is expressed in my own words. Any uses made within it of the works of other authors in any form (e.g., ideas, equations, figures, text, tables, programs) are properly acknowledged at any point of their use. A list of the references employed is included.

Signed: _____



UNIVERSITY *of the*
WESTERN CAPE

Date: 15-07-2019

Abstract

This study presents an investigation of baryonic specific angular momentum (j_b) as a function of baryonic mass (M_b) spanning a range, $9.4 \lesssim \log_{10}(M_b/M_\odot) \lesssim 11.0$ in the sample of eleven nearby early-type disk galaxies. This study is based on 30 arcsec resolution archival data observed as part of the Westerbork HI Survey of Spiral and Irregular galaxies Project (WHISP). In order to accurately model well-resolved HI kinematics of each galaxy used in this study, intermediately inclined ($40^\circ < i < 75^\circ$) with an HI major axis diameter greater than 180 arcsec (6 beams) were considered from a larger sample of early-type disk galaxies studied by Noordermeer et al. (2005), (N05). A subset of 11 galaxies was recovered from N05 sample that serve as a primary sample for this study. All HI data products (HI total intensity maps, HI velocity fields, and HI velocity dispersion maps) were re-derived by parameterising the WHISP HI data cubes by fitting a single Gaussian to every line profile with peak amplitude greater than 3σ . ROTCUR routine in GIPSY has been used to generate HI rotation curve for each galaxy. All dynamical models have been compared directly to the HI data in order to check their accuracy. HI imaging was used to calculate the contribution of gas component (neutral hydrogen and helium gas) to the angular momentum of each galaxy. To calculate the contribution of stars to the angular momentum, WISE $3.4 \mu\text{m}$ imaging was used. HI and stellar mass surface density profiles were combined to generate baryonic mass profiles for the galaxies. The baryonic mass surface density profile for each galaxy was used with HI rotation curve for each galaxy to generate the total specific baryonic angular momentum profile for each galaxy. The sample of early-type disk galaxies in this study was found to lie systematically in the same relation followed by late-type galaxies in the $j_b - M_b$ plane. The power-law relation was found to be, $j_b \propto M_b^\alpha$ over the entire baryonic mass range, with slope $\alpha \approx 0.46$. The $j_b - M_b$ relation in this work was found to be shallower than the $j_\star - M_\star$ relation obtained by Fall (1983), (F83). The lack of an offset in this work is because, high-precision measurements (taking into account most HI masses at the outer-most radius) of baryonic angular momentum-mass relation approach were performed while in F83's work, stellar angular momentum-mass relation of early-type galaxies were performed based on low-precision measurements. Hence this work suggest that angular momentum-mass relation depend on the nature of the method used.

Acknowledgements

First and foremost, I would like to express my deepest gratitude to my parents who have always love and supported me. A special thanks to my daughter Shekinah, thank you for being my hope, courage and source of strength. To my siblings, thank you for the love and support you have shown me.

I would like to thank my supervisors, Dr E. Elson and Prof. R. Maartens for all their invaluable help, guidance, advice, ideas, and patience. I would like to acknowledge the National Astrophysics and Space Science Programme (NASSP) for funding this work, also with the help of Centre for Radio Cosmology (CRC). The anonymous referees are thanked for giving feedback and comments that greatly improved the overall quality for this thesis. A special thanks to Prof. S. Allie, thank you for your kindness and support you have shown to me from the day we met. A special thanks to Kimeel and all my colleagues.



Contents

Declaration of Authorship	i
Abstract	ii
Acknowledgements	iii
Contents	iv
List of Figures	vi
List of Tables	viii
1 Introduction	1
1.1 Galaxy morphology	2
1.2 Angular momentum history	2
1.2.1 Observational & theoretical study of $j - M$ relation	3
1.2.2 Traditional measurements of $j - M$ relation	3
1.2.3 High-precision measurements of $j_b - M_b$ relation	5
1.3 In this thesis	6
1.3.1 Thesis outline	6
2 Data and galaxy sample	7
2.1 HI imaging	7
2.2 Sample selection criteria	8
2.3 Noise estimations	10
2.4 HI line profiles parameterisations	11
2.5 HI data products	13
2.6 Comparisons to previous results	15
3 Modelling and analysis	28
3.1 HI mass surface density profiles	28
3.2 Stellar mass surface density profiles	29
3.3 Baryonic mass surface density profiles	31
3.4 Summary of all mass surface density profiles	32
3.5 HI rotation curves	35

3.6	Model-data comparisons	43
3.6.1	Velocity field comparisons	43
3.6.2	Three-dimensional comparisons	49
3.7	High-precision measurements of angular momentum	52
4	Results and discussion	54
4.1	Comparison between low- and high-precision measurements	57
4.2	Inner HI rotation curves inaccuracies	61
4.3	Investigating uncertainties on baryonic specific angular momentum from the stellar contribution	63
4.4	Difference between this work and Fall (1983)	65
5	Summary and conclusion	67
5.1	Future prospects	68
A		70
A.1	Baryonic mass surface density fitted with an exponential function	72
B		76
Bibliography		88



List of Figures

1.1	Total intrinsic stellar specific angular momentum of galaxies as a function of total stellar mass, reproduced from F83. Galaxy types are shown according to the legend in top left corner. Clearly, F83 found that early- and late-type galaxies have different amount of angular momentum. The dotted line shows a trend $j_{\star} \propto M_{\star}^{2/3}$ Romanowsky and Fall (2012).	4
2.1	Galaxy sample's characteristics	9
2.2	200 × 200 noise-filled pixels distribution in UGC02183	10
2.3	Single-pixel line profiles	11
2.4	Overall accuracy of the fitted Gaussians.	12
2.5	Illustration of V_{sys} and W_{50} measurements from HI spectra for UGC02183.	14
2.6	Intrinsic properties comparisons	16
2.7	Images and derived profiles for UGC02183.	17
2.8	Images and derived profiles for UGC03546.	18
2.9	Images and derived profiles for UGC03580.	19
2.10	Images and derived profiles for UGC05960.	20
2.11	Images and derived profiles for UGC06283.	21
2.12	Images and derived profiles for UGC06786.	22
2.13	Images and derived profiles for UGC06787.	23
2.14	Images and derived profiles for UGC11269.	24
2.15	Images and derived profiles for UGC11670.	25
2.16	Images and derived profiles for UGC11951.	26
2.17	Images and derived profiles for UGC12043.	27
3.1	Conversion of units of stellar surface brightness	31
3.2	Mass profiles derived and used in this work.	32
3.3	Mass profiles derived and used in this work continued.	33
3.4	Mass profiles derived and used in this work continued.	34
3.5	Full tilted ring model for UGC02183.	36
3.6	Full tilted ring model for UGC03546.	37
3.7	Full tilted ring model for UGC03580.	37
3.8	Full tilted ring model for UGC05960.	38
3.9	Full tilted ring model for UGC06283.	38
3.10	Full tilted ring model for UGC06786.	39
3.11	Full tilted ring model for UGC06787.	39
3.12	Full tilted ring model for UGC11269.	40
3.13	Full tilted ring model for UGC11670.	40
3.14	Full tilted ring model for UGC11951.	41

3.15	Full tilted ring model for UGC12043.	41
3.16	Velocity field comparisons	43
3.17	Comparison between observed and modelled HI velocity field for UGC03546.	44
3.18	Comparison between observed and modelled HI velocity field for UGC03580.	44
3.19	Comparison between observed and modelled HI velocity field for UGC05960.	45
3.20	Comparison between observed and modelled HI velocity field for UGC06283.	45
3.21	Comparison between observed and modelled HI velocity field for UGC06786.	46
3.22	Comparison between observed and modelled HI velocity field for UGC06787.	46
3.23	Comparison between observed and modelled HI velocity field for UGC11269.	47
3.24	Comparison between observed and modelled HI velocity field for UGC11670.	47
3.25	Comparison between observed and modelled HI velocity field for UGC11951.	48
3.26	Comparison between observed and modelled HI velocity field for UGC12043.	48
3.27	Three-dimensional comparisons.	51
3.28	Cumulative baryonic specific angular momentum as a function of radius.	52
3.29	Cumulative baryonic specific angular momentum as a function of radius continued.	53
4.1	Specific baryonic angular momentum as a function of baryonic mass	55
4.2	Baryon profile fitted to an exponential function	58
4.3	Low-precision j_b measurements as a function of high-precision measurements for the galaxies used in this work.	59
4.4	Low-precision j_b measurements as a function of high-precision measurements for the galaxies used in this work.	60
4.5	Quantifying the effects of inner HI rotation curve inaccuracies	62
4.6	Quantifying the effects of inner HI rotation curve inaccuracies continued.	63
4.7	Quantifying an uncertainty rises from mass-to-light ratio.	64
4.8	Gas fraction as a function of stellar mass for all galaxies in this work	65
A.1	Overall accuracy of the fitted Gaussians.	70
A.2	Overall accuracy of the fitted Gaussians continued.	71
A.3	Overall accuracy of the fitted Gaussians continued.	72
A.4	Baryonic mass surface density fitted with an exponential function.	72
A.5	Baryonic mass surface density fitted with an exponential function continued.	73
A.6	Baryonic mass surface density fitted with an exponential function continued.	74
A.7	Baryonic mass surface density fitted with an exponential function continued.	75
B.1	HI column density profiles.	76
B.2	HI column density profiles continued.	77
B.3	Three-dimensional comparisons.	78
B.4	Model-data comparison for UGC03580: channel maps & pv-slices.	79
B.5	Model-data comparison for UGC05960: channel maps & pv-slices.	80
B.6	Model-data comparison for UGC06283: channel maps & pv-slices.	81
B.7	Model-data comparison for UGC06786: channel maps & pv-slices.	82
B.8	Model-data comparison for UGC06787: channel maps & pv-slices.	83
B.9	Model-data comparison for UGC06283: channel maps & pv-slices.	84
B.10	Model-data comparison for UGC11670: channel maps & pv-slices.	85
B.11	Model-data comparison for UGC11951: channel maps & pv-slices.	86
B.12	Model-data comparison for UGC12043: channel maps & pv-slices.	87

List of Tables

2.1	Sample properties	8
2.2	Noise best-fit Gaussian parameters for the noise distributions.	11
2.3	HI properties of the sample of galaxies used in this study	14
3.1	Parameters to model the HI observations for all galaxies	50
4.1	High-precision measures of baryonic specific angular momentum for the sample of WHISP galaxies in this work.	54
4.2	Low-precision measures of baryonic specific angular momentum.	58
4.3	Investigating the effect of uncertainties from the stellar contribution into the total angular momentum of each galaxy.	64



*This thesis is dedicated to my parents, Nndavheleseni Frank
Tshiwawa and Tshilidzi Mercy Tshiwawa.*



UNIVERSITY *of the*
WESTERN CAPE

Chapter 1

Introduction

Galaxies are one of the most striking constituents of the Universe. There are many things that can be said about physical processes which created these objects and have governed their evolution. A typical galaxy is a collection of stellar and interstellar distribution of matter isolated in space and held together by its own gravity. These bound objects are thought to be embedded in non-spherical distributions of dark matter. Galaxies comes in different flavors of morphological class as a result of how they were formed, how they interact with their environment, how they were influenced by internal perturbation, etc (e.g., see [Abraham and van den Bergh 2001](#)). The classification schemes of galaxies were derived based on the optical appearance: bulge/disk ratio and prominence of spiral arms. Galaxy evolution history is an important subject towards understanding galaxy formation and attempting to understand how galaxies evolved is one of the critical goals in topics of research today. However angular momentum (per unit mass) probably mostly decides the form of a galaxy. The evolution of galaxies are thought to be governed by mass and angular momentum. Angular momentum and mass are thought to be fundamental properties of galaxies that depend primarily on their evolutionary history and are subjected to physical conservation laws.

In the Λ CDM framework of galaxy formation, tidal torquing from merger history should supply baryons and dark matter with similar amounts of angular momentum (thanks to the great universally recognized conservation laws of physics: mass, energy, and momentum). The specific angular momentum of the dark matter halo scales as its mass to the power $\frac{2}{3}$. This fundamental scaling relation was first introduced by [Fall \(1983\)](#), (F83). F83 shows that spiral and elliptical galaxies have different amount of angular momentum on

the $j - M$ plane defined by the scaling relation $j_{\star} = q M_{\star}^{\alpha}$ (where the subscript indicates quantities relating to the stellar component of a galaxy), with slope $\alpha \approx \frac{2}{3}$. Where j_{\star} is the stellar specific angular momentum, q is the scale factor, and M_{\star} is the stellar mass. Most significantly, the scale factor was found to be lower in elliptical galaxies signifying the loss of angular momentum as galaxies evolved. The current-day angular momentum content of a galaxy is thought to be a good tracer of a galaxy's formation history.

This thesis serves as an investigation of the angular momentum content of eleven early-type disk galaxies in the nearby Universe, through the observation of HI gas kinematics and spectroscopic techniques. Section 1.1 of this introduction will give a general overview of the origin of angular momentum in different morphological types of galaxies. Section 1.2 discuss briefly galaxy formation in Λ CDM and the origin of angular momentum.

1.1 Galaxy morphology

According to the interpretation of the Hubble tuning fork diagram there are mainly two types of galaxies known today: early-type galaxies, defined by the lack of spiral arms and late-type galaxies, defined by significant spiral arms in the optical band. Early-type galaxies in general have the shape of an oblate spheroid with different degrees of rotation; supported by random motions while late-type galaxies have flat disks mostly supported by rotation. Systems with disks (late-type galaxies) are expected to have higher angular momentum while those dominated by bulge (early-type galaxies) have low angular momentum. Primarily early-type galaxies are thought to be an outcome of major mergers while late-type galaxies are an outcome of minor mergers (e.g., [Steinmetz and Navarro 2002](#); see, [Toomre and Toomre 1972](#)).

1.2 Angular momentum history

The merger history plays a significant role in mass and angular momentum. In the Λ CDM scenario of galaxy formation, gravitation is thought to be the dominant force capable of transferring angular momentum to developing proto-galaxy formed by the merging of smaller units under the influence of gravity. A net tidal torque acting on a proto-galaxy will naturally cause the proto-galaxy to start rotating, thereby gaining angular momentum. So the current-day angular momentum content of a galaxy is therefore closely linked to its formation history ([Peebles, 1969](#)).

1.2.1 Observational & theoretical study of $j - M$ relation

Angular momentum has been studied from both theoretical and observational viewpoints. Peebles (1969) was the first to introduce the relationship between specific angular momentum j_h and mass M_h (where the subscript indicates quantities relating to dark matter halo) using theoretical perspective. For a galaxy which is formed through tidal torques, the specific angular momentum of the dark matter halo is related to the mass of the halo by the empirical relation as $j_h = k(\lambda)M_h^{2/3}$, with λ being the spin parameter of the dark matter halo that is independent of the mass (Peebles, 1969). The specific angular momentum of gas that collapses into dark matter halo, under hierarchical galaxy formation is conserved, is also expected to obey the same empirical relation for dark matter halo. Mass (M) and the specific angular momentum (j) are two parameters of galaxies that are strongly correlated with the morphological class of galaxies (Kormendy, 1990). The theoretical link between j and M was provided by both Romanowsky and Fall (2012) and Obreschkow and Glazebrook (2014). Obreschkow and Glazebrook (2014) also derived the relation linking j and M by assuming Hubble constant $H = 70 \text{ km s}^{-1} \text{ Mpc}^{-1}$ and show that the specific baryonic angular momentum scales with baryonic mass viz:

$$\frac{j_b}{10^3 \text{ kpc km s}^{-1}} = 1.96 \lambda f_j f_M^{-2/3} \left(\frac{M_b}{10^{10} M_\odot} \right)^{2/3}, \quad (1.1)$$

where f_j denotes the specific angular momentum of baryons divide by the specific angular momentum of the CDM halo, f_M denotes the mass of baryons divided by the mass of the halo, and λ is the dimensionless spin parameter associated with the angular momentum of the galaxy (see Peebles (1969)). So for baryons $j_b \propto M_b^{2/3}$ (where the subscript indicates quantities relating to baryon matter).

1.2.2 Traditional measurements of $j - M$ relation

Fall (1983), (F83) was the first to look at the stellar component in a sample of 100 galaxies and show that both spiral and elliptical galaxies occupy distinct regions in the $\log j_\star - \log M_\star$ plane. An empirical relation $j_\star \propto M_\star^\alpha$ with log-slope $\alpha \approx$ of 0.6 was obtained for both elliptical and spiral galaxies. However, elliptical galaxies were found to have low amount of angular momentum as compared to spiral galaxies. This is clearly depicted in Figure 1.1.

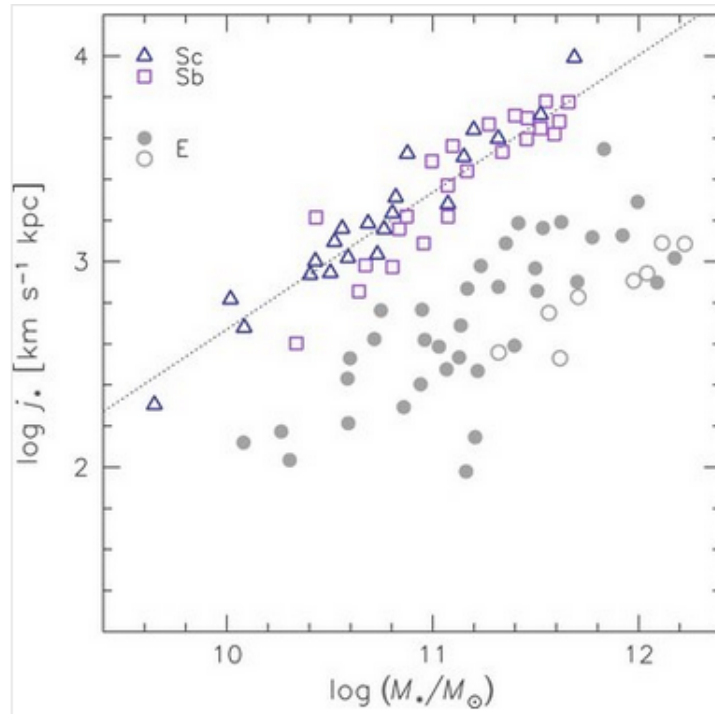


Figure 1.1: Total intrinsic stellar specific angular momentum of galaxies as a function of total stellar mass, reproduced from F83. Galaxy types are shown according to the legend in top left corner. Clearly, F83 found that early- and late-type galaxies have different amount of angular momentum. The dotted line shows a trend $j_* \propto M_*^{2/3}$ Romanowsky and Fall (2012).

This relation was also confirmed by Romanowsky and Fall (2012) focusing chiefly on a sample of early-type galaxies. In a range of different morphological class of elliptical and spiral galaxies, galaxies were separated into their respective components (pure disks and bulges) and it was found that both disks and bulges naturally follow similar relation obtained by F83 - thus extending the work of F83. However, an offset factor of ~ 6 between parallel sequences formed by both pure disks and bulges was obtained. It was found that both bulges and disks in stellar components follow the similar trend introduced by F83. Both Romanowsky and Fall (2012) and Fall and Romanowsky (2013) studies obtained similar $j_* \propto M_*^{2/3}$ scaling relation claimed by F83; the only difference was that an offset factor of 5 between parallel sequence formed by disk-dominated and elliptical galaxies was later obtained in Fall and Romanowsky (2013) study. The revision work of Fall and Romanowsky (2013) shows that specific angular momentum and mass relation of the stellar matter distribution of different morphological types follows the parallel sequence relation nearly similar for both elliptical and disk-dominated galaxies. These studies estimate the measure of the angular momentum content based on assumptions from F83.

F83 study assumed an exponential disk rotating at a constant velocity (i.e. flat rotation curve) and shows that the total angular momentum is given by,

$$\bar{j}_* = 2\bar{R}_* V_{\text{flat}}, \quad (1.2)$$

where V_{flat} is the constant velocity estimate from the velocity width measurements. And \bar{R}_* in equation 1.2 is an estimate of the exponential scale radius of the galaxy disk.

1.2.3 High-precision measurements of $j_b - M_b$ relation

Obreschkow and Glazebrook (2014) was the first to present high precision measurements, using full rotation curves and full radial mass profiles, of the relation between specific baryonic angular momentum (j_b) and baryonic mass M_b using the kinematics of 16 nearby spiral galaxies with baryon mass ranging, $10^9 - 10^{11}$ and bulge mass fraction up to 0.32 from the THINGS survey Walter et al. (2008). They performed an integration of full rotation curves and full radial mass profiles numerically over the galactic disk to find the total angular momentum. They also study the correlation between baryonic mass, specific baryonic angular momentum and bulge fraction and found a tight correlation supported and understood in the Λ CDM models. Chowdhury and Chengalur (2017) also derived specific baryonic angular momentum from HI kinematics combined with stellar mass profiles of five gas rich dwarf galaxies in voids. They found that $j_b - M_b$ relation obtained from their sample deviates significantly from those of spiral galaxies and the probability for dwarf galaxies to follow spiral galaxies' relation much smaller. Elson (2017) study was based on 37 nearby galaxies from the WHISP survey. Over ~ 3 order of magnitude in M_b , the j_b was found to be consistent with the theoretical expected relation of $j_b \propto M_b^{2/3}$. This results is consistent with higher mass spiral galaxies from Obreschkow and Glazebrook (2014). Then Butler et al. (2016) also investigated the relation between M_b and j_b using the LITTLE THINGS sample containing 14 rotating dwarf irregular galaxies. They found that dwarf galaxies systematically show higher j_b values than expected from the spiral scaling relation of $j_b \propto M_b^{2/3}$. Their results are consistent with those obtained by Chowdhury and Chengalur (2017). High-precision measurements of baryonic specific angular momentum as a fraction of baryonic mass of Dwarf galaxies in void were studied by Kurapati et al. (2018), (K18). Their sample was drawn from Lynx Cancer void, located in the nearby Universe. Over the range $10^{7.3} \lesssim M_b/M_\odot \lesssim 10^{9.4}$ in baryonic mass, the baryonic specific angular momentum was found to be high, but comparable to other dwarf galaxies that lie outside the voids.

1.3 In this thesis

This thesis aims to study the angular momentum content of early-type galaxies. The baryonic specific angular momentum as a function of baryonic mass in the sample containing 11 early-type galaxies is investigated in order to constrain whether their angular momentum properties differ significantly from the late-type galaxies that have already been studied in the literature.

1.3.1 Thesis outline

- Chapter 2 present a description of the galaxy sample used in this work. The explanation of HI data cube parameterisations of each galaxy are presented here. This chapter presents all the final standard HI data products required for this work.
- In Chapter 3, the HI data are used to provide a full kinematic study of all galaxies in the sample. HI total intensity maps presented in the previous chapter were used to generate HI mass surface density profiles. The surface brightness from WISE $3.4\mu\text{m}$ imaging have been used together with an assumed mas-to-light ratio to generate stellar mass surface density profiles. HI mass surface density profiles and stellar mass surface density were combined to generate baryonic mass surface density profiles. HI rotation curves are generated by fitting a tilted ring model to the HI velocity fields. Also the details of the methods used to compare the dynamical models to the HI data are presented. The HI velocity fields and baryonic mass surface density profiles were used to construct the cumulative baryonic specific angular momentum profiles for each galaxy in the sample.
- Chapter 4, cumulative baryonic specific angular momentum profiles constructed in chapter 3 were used to study and discuss the distribution of the data points in the $j_b - M_b$ plane in the context of other results in the literature.
- Chapter 5 provide a summary and conclusion of the results obtained in this thesis.

Chapter 2

Data and galaxy sample

Observations of atomic hydrogen (HI) in nearby galaxies provide the basis upon which HI gas kinematics and properties can be unravelled. High angular and spectral resolution HI observations play a vital role in fully modelling the HI kinematics of gas in and around galaxies. This chapter presents the details of the galaxy sample used in this work.

Section 2.1 of this chapter briefly describe the HI imaging. Section 2.2 of this chapter present sample selection criteria. Section 2.3 describe how the noise level for each galaxy in HI data cubes was quantified. Section 2.4 describe how HI line profiles for HI data cubes in the sample were parameterised. Section 2.5 presents all standard HI data products for the sample presented in Section 2.2. Finally, in section 2.6, the intrinsic properties obtained in this work are compared with those obtained in Noordermeer et al. (2005), (N05).

2.1 HI imaging

This study is based on 30 arcsec resolution archival data from the Westerbork HI Survey of Spiral and Irregular galaxies Project (WHISP; Van der Hulst et al.). The HI data cubes were downloaded, and are available online for public use, from <http://wow.astron.nl>. WHISP is an imaging survey of the HI content of several hundreds of nearby galaxies observed with the Westerbok Synthesis Radio Telescope (WSRT) in the northern sky. The observations were carried out above a declination $\delta(2000) = 20^\circ$. This declination limit was carefully chosen in order to avoid degradation of the synthesized beam in the WSRT instrument. Observations were carried out between 1993 and 2002 aiming to investigate HI content and large-scale kinematics of almost 400 disk galaxies systematically

covering Hubble types ranging from S0 to Im (Noordermeer et al. 2005; Swaters et al. 2009). All WHISP galaxies were selected from the Uppsala General Catalogue to have an optical angular size greater than an arcmin along their major axis diameter ($D_{25} > 1'$), and lower line flux density limit greater than 20 mJy. For a full description of the survey and the data reduction process the reader is referred to Van der Hulst et al. (2001).

2.2 Sample selection criteria

The galaxy sample for the current study was selected from a larger sample presented by Noordermeer et al. (2005), (N05), who present HI observations of 68 early-type disk galaxies in a range of different morphological types. In order to accurately model the velocity field of each galaxy used in this study, intermediately inclined galaxies ($40^\circ < i < 75^\circ$) with an HI major axis diameter greater than 180 arcsec were selected from the full N05 sample. After applying the above-mentioned criteria to the N05 sample, a subset of 11 galaxies was recovered that serve as the primary sample for this study. Table 2.3 lists some of the main properties of our galaxy sample.

Table 2.1: (1) UGC number, (2) Alternative name, (3) RA, (4) Dec, (5) morphological type, (6) absolute B-band magnitude, (7) Heliocentric radial velocity from this study, (8) distance, (9) inclination angle from this study.

UGC	Alternative name	RA (2000) h m s	Dec (2000) ° ' "	Type	M_B	V_{hel} km s ⁻¹	D Mpc	i °
(1)	(2)	(3)	(4)	(5)	(6)	(7)	(8)	(9)
2183	NGC 1056	02 42 48.3	28 34 27	Sa	-19.60	1535	21.5	60
3546	NGC 2273	06 50 8.7	60 50 45	SB(r)a	-20.16	1838	27.3	50
3580	-	06 55 30.8	69 33 47	SA(s)a pec	-18.19	1199	19.2	66
5960	NGC 3413	10 51 20.7	32 45 59	SO	-17.39	643	10.5	63
6283	NGC 3600	11 15 52.0	32 45 59	Sa	-17.17	713	12.0	71
6786	NGC 3900	11 49 9.4	27 01 19	SA(R)0+	-19.94	1799	25.9	63
6787	NGC 3898	11 49 15.4	56 05 04	SA(s)ab	-20.25	1171	18.9	66
11269	NGC 6667	18 30 39.8	67 59 23	SABab? pec	-20.11	2581	38.3	63
11670	NGC 7013	21 03 33.6	29 53 51	SA(r)0/A	-19.53	775	12.7	68
11951	NGC 7231	22 12 30.1	45 19 42	SBa	-19.14	1086	17.4	67
12043	NGC 7286	22 27 50.5	29 05 45	SO/a	-17.15	1007	15.4	67

All columns (except column 7 and 9) are also shown in Table 1 of full N05 sample.

Figure 2.1 shows the distributions of some of the main galaxy properties from the full N05 sample (black histograms) and the sub-sample of 11 galaxies used in this work (red histograms).

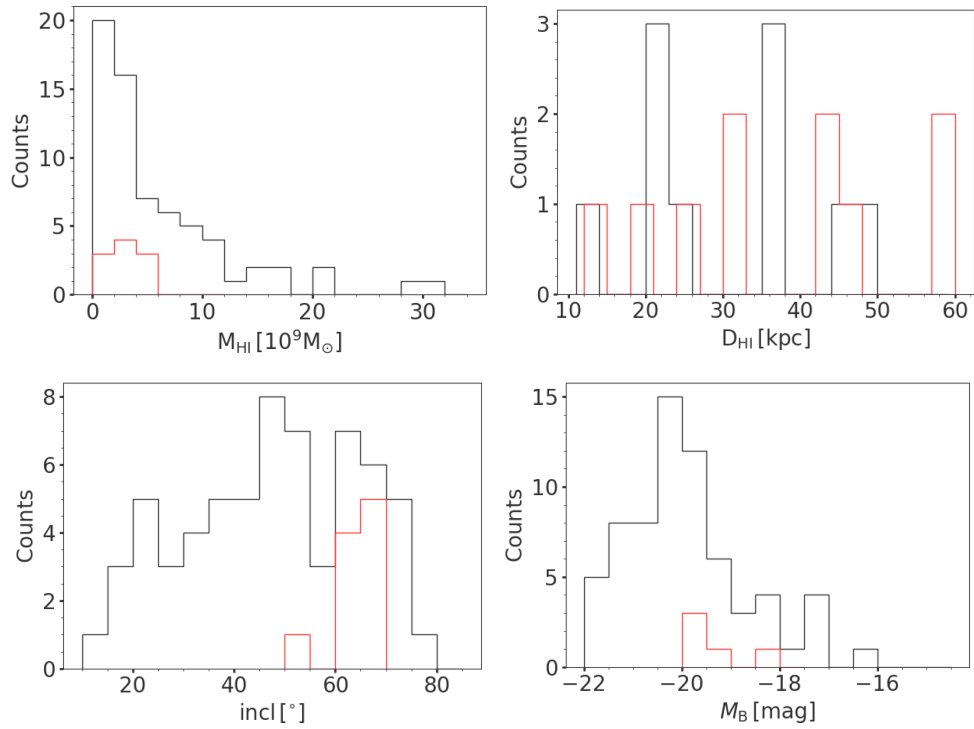


Figure 2.1: Distribution of various galaxy properties from the full N05 sample (black histograms) and sub-sample of 11 galaxies used in this study (red histograms). The top left panel shows the distributions of HI masses, the top right panel the distribution of HI diameters (as measured at an HI mass surface density level of $1 M_{\odot}/\text{pc}^2$), the bottom left panel the distribution of inclinations, and bottom right panel the distribution of B-band absolute magnitudes.

The sample containing 11 galaxies, which has been used to quantify angular momentum content in this work has been selected from a sample containing 68 galaxies in total. Figure 2.1, shows that HI masses, HI diameters and inclinations in this work represent the inner part of the sample obtained and used in N05.

2.3 Noise estimations

In this work, the noise level in each data cube was quantified as the standard deviation of the distribution of 200 X 200 line-free pixels spanning the full spectral range of the cube. Most data cubes contained artifacts or contaminated emissions near the start and end of the spectral axis. These channels were excluded from any form of noise calculations. Channels were removed symmetrically along the spectral axis: for instance UGC02183 contained 127 channels along the spectral axis, so 42 channels from the beginning and towards the end were removed and noise estimation for this galaxy was based on the central 43 channels.

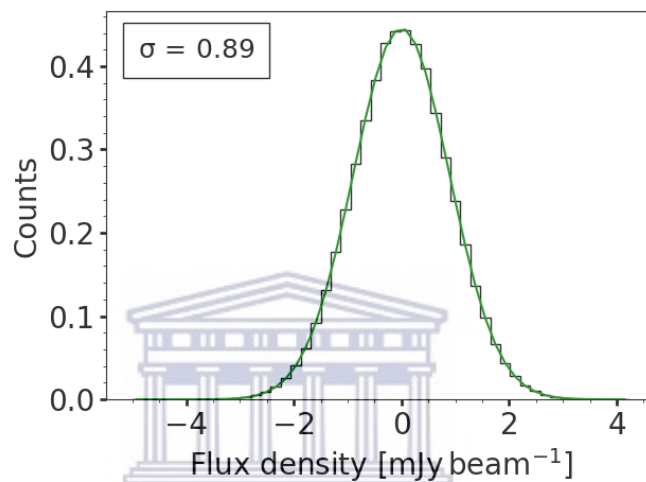


Figure 2.2: Distribution of noise pixels extracted from the HI data cube of UGC02183. The green curve is a fitted Gaussian. The histogram is normalized. The legend in top left corner of the figure indicates the standard deviation σ of the fitted Gaussian in units of mJy beam^{-1} .

The distribution of a noise-filled channels from the HI data cube of UGC02183 is shown in Figure 2.2. Shown as a green curve is Gaussian fitted to the distribution. The best-fitting mean and standard deviation of this Gaussian are $\bar{\mu} = -0.76 \mu\text{Jy beam}^{-1}$ and $\sigma = 0.89 \text{ mJy beam}^{-1}$, respectively. The fitted means and standard deviations for all of the galaxies used in this work are shown in column 2 and 3, respectively, of Table 2.2. For all HI data cubes, pixels below a threshold of 3σ were flagged as noise and were excluded from all data products generated from the HI data cubes (Section 2.4). Shown in Table 2.2 column 4 are the total number of channels used for each galaxy to estimate noise and generate all HI data products.

Table 2.2: Best-fit Gaussian parameters for the noise distributions of the galaxies used in this study. (1) UGC number, (2) mean, (3) standard deviation, (4) Number of channels.

UGC	$\bar{\mu}$	σ	Channels
(1)	$\mu\text{Jy beam}^{-1}$	mJy beam^{-1}	(4)
UGC02183	-0.76	0.89	43
UGC03546	0.80	0.66	49
UGC03580	0.82	3.10	65
UGC05960	0.10	1.37	49
UGC06283	0.32	0.73	57
UGC06786	2.18	0.85	67
UGC06787	-0.58	0.73	59
UGC11269	0.36	0.66	59
UGC11670	-1.38	0.82	47
UGC11951	-0.52	3.69	87
UGC12043	0.58	1.38	47

2.4 HI line profiles parameterisations

In order to generate new, accurate HI data products for the galaxy sample used in this study, the WHISP HI data cubes were parameterised by fitting a single Gaussian to every line profile at each position with peak amplitude higher than 3σ . Initial estimates for the amplitude, mean, and standard deviation of each fitted Gaussian were the peak flux density of the profile, the associated line-of-sight velocity, and 10 km s^{-1} , respectively.

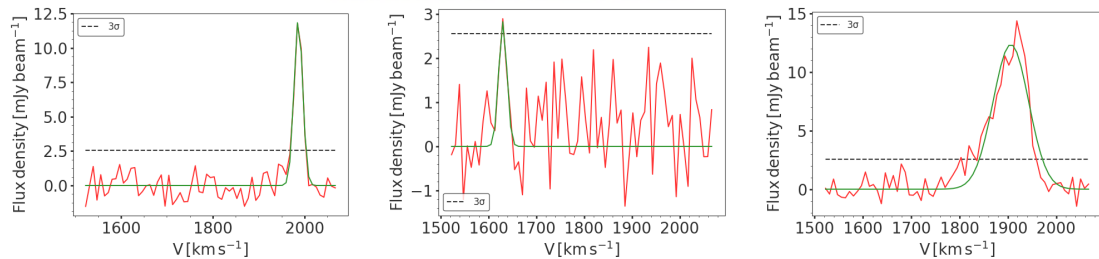


Figure 2.3: Various examples of single-pixel line profiles with fitted Gaussians, extracted from HI cube of UGC06786. Fitted Gaussians are indicated as green curves. Most galaxies have most of their HI line profiles well approximated by a single Gaussians. Shown on the left panel is a high signal-to-noise HI line profile. Shown in the middle panel is a low signal-to-noise line profile. Shown in the right panel is an asymmetric line profile. 3σ noise level is indicated by a black horizontal dotted line in each panel.

Figure 2.3 shows examples of various types of parameterised HI line profiles extracted from the HI data cube of UGC06786. The left panel is an example of a high signal-to-noise (S/N) profile. The middle panel shows a typical low S/N profile. In this case, the fitted Gaussian accurately picks out the position of the profile peak flux density. The right panel provides an example of a slightly asymmetric HI line profile, for which the fitted Gaussian does a reasonably good job of picking out the peak flux density position. In order to assess the overall accuracy of the fitted Gaussians, the left panel in Figure 2.4 shows the distribution of reduced chi-squared (χ_r^2) values for UGC06786. The centre panel shows the spatial distribution of the χ_r^2 values. Towards the centre of the galaxy where two HI over-densities regions are observed, the typical χ_r^2 value increases to approximately 2.

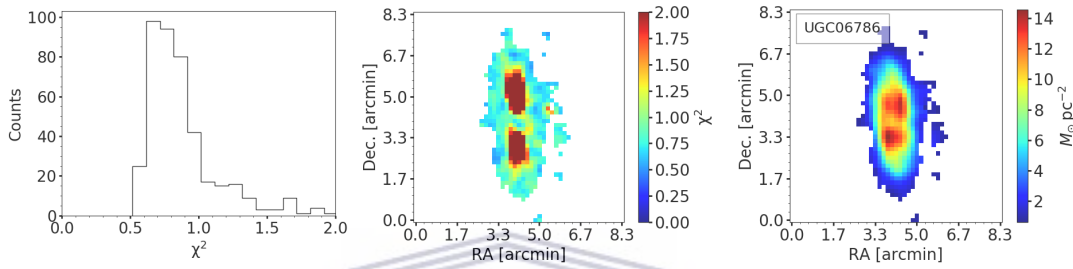


Figure 2.4: This figure illustrates the overall accuracy of the fitted Gaussians in HI data cube of UGC06786. Left panel shows the distribution of spatial χ_r^2 , middle panel shows χ_r^2 map, right panel shows HI total intensity map.

The distribution of χ_r^2 values and χ_r^2 map for each galaxy in this work is shown in Figures A.1 - A.3 in Appendix A.

In this work the χ_r^2 statistic has been used to quantify the goodness of the Gaussian fit, since the parameterisations were performed by approximating HI line profiles with single Gaussians. The χ_r^2 function in this work is defined as the sum of the squared difference between the data (X_i) and the fitted Gaussian (Y_i) divided by the degrees of freedom, DoF:

$$\chi_r^2 = \frac{\sum_i^n (X_i - Y_i)^2}{\text{DoF}} \quad (2.1)$$

DoF = N - n_p , where N is the number of data points and n_p is the number of independent fit-parameters (three parameters for Gaussian function). When $\chi_r^2 \approx 1$, the model reciprocates the data, and is acceptable. $\chi_r^2 < 1$ indicates an over-fitting, while $\chi_r^2 > 1$ indicates poor fit of the model to the data.

2.5 HI data products

The areas of the Gaussian fit to the HI profiles were used to generate HI total intensity maps for the galaxies in the sample by calculating all areas of the fitted Gaussians. HI maps were converted from units of mJy beam^{-1} to mJy , then to units of M_{\odot} using the following equation,

$$M_{\text{HI}} = 2.36 \times 10^5 D^2 \times \Sigma_i S_i \Delta v, \quad (2.2)$$

where D is the distance of the galaxy in megaparsec (Mpc), and $\Sigma_i(S_i \Delta v)$ is the summation over the total emission in each channel in units of Jy km s^{-1} .

All the total HI integrated flux measured in this work for each galaxy are shown in column 8 of Table 2.3.

Finally, the maps were converted to mass surface density units of $M_{\odot} \text{pc}^{-2}$. The total HI masses were measured as the sum of the total HI flux from the total HI intensity maps. All the total HI masses measured in this work are shown in column 9 of Table 2.3. All HI mass surface density maps are shown in middle left panels in Figures 2.7 - 2.17.

The means of the Gaussian fit to the HI profiles were used to generate an HI velocity field for the galaxies in our sample. All HI velocity fields are shown in middle right panels in Figures 2.7 - 2.17. The standard deviations of the Gaussian fit to the HI line profiles were used to generate HI velocity dispersion maps for the galaxies in our sample. All HI velocity dispersion maps are shown in bottom left panels in Figures 2.7 - 2.17.

All global profiles were derived from the 30 arcsec WHISP HI data cubes by summing all HI emission with peak flux density greater than 3σ . All HI spectra in this work exhibit "doubled horned" or "double peaked" shapes, this behaviour was suggested by Walter et al. (2008) as being indicative of nearly flat rotation curve. The systemic velocity (V_{sys}) for each galaxy in the sample was determined from 50% flux density level (e.g., Kamphuis et al. (1995)). The V_{sys} of each galaxy was determined as an average of the profile edges at 50% flux density level. Then 50% line width (W_{50}) in this work was measured as the difference between profile edges at 50% level. No attempt was made to correct for an instrumental broadening due to random motions of the gas. All V_{sys} and W_{50} measured in this work are shown in column 6 & 7 of Table 2.3, respectively. Figure 2.5 demonstrates how V_{sys} and W_{50} measurements were obtained. All HI global profiles are shown in bottom right panels in Figures 2.7 - 2.17.

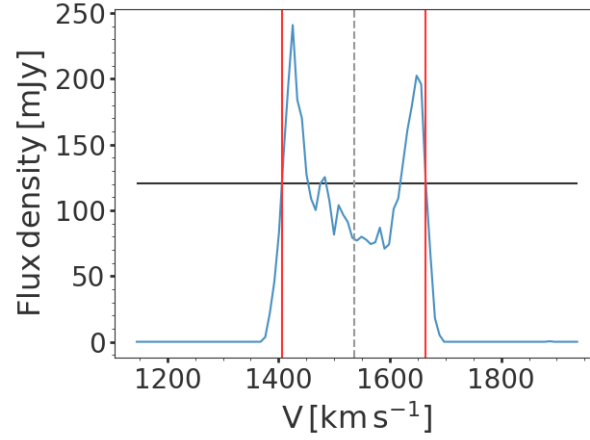


Figure 2.5: This figure demonstrates, by using UGC02183, how all the V_{Sys} and W_{50} for each galaxy were obtained in this work. Black solid line indicates 50% flux density level. Two solid red lines indicate profile edges at 50% flux density level. Grey dotted line indicates V_{sys} , obtained as an average of the profile edges at 50% level. The difference of the profile edges at 50% flux density level gives the W_{50} .

Table 2.3: HI properties of the sample of galaxies used in this study. (1) UGC number, (2) pixel size, (3) beam size, (4) noise level in the channel maps, (5) channel width (6) systemic velocity, (7) line width of global profile at the 50% level, (8) total integrated HI flux density, (9) total HI mass.

UGC	pixel size arcsec×arcsec	$B_{\text{maj}} \times B_{\text{min}}$ arcsec ×arcsec	σ mJy beam ⁻¹	dv km s ⁻¹	V_{sys} km s ⁻¹	W_{50} km s ⁻¹	$\int F dv$ Jy km s ⁻¹	M_{HI} $10^9 M_{\odot}$
(1)	(2)	(3)	(4)	(5)	(6)	(7)	(8)	(9)
2183	10×10	42.2×30.0	0.89	8.24	1535	256.0	42.0	4.6
3546	10×10	35.6×32.5	0.66	8.24	1834	336.0	16.3	2.9
3580	10×10	27.1×26.9	3.10	4.12	1198	164.0	45.0	3.9
5960	10×10	34.1×24.7	1.40	4.12	637	641.0	32.9	0.90
6283	10×10	29.8×29.6	0.73	4.12	710	204.0	58.0	2.0
6786	10×10	44.4×31.5	0.85	8.24	1790	399.0	25.0	4.0
6787	10×10	31.9×29.7	0.73	8.24	1168	461.0	56.8	4.8
11269	10×10	34.8×31.4	0.66	8.24	2633	351.0	38.3	13.2
11670	10×10	37.3×23.6	0.82	8.24	769	317.0	31.9	1.2
11951	10×10	27.0×27.0	3.70	4.12	1082	173.0	27.7	2.0
12043	10×10	37.8×24.6	1.40	4.12	1005	153.0	24.8	1.4

2.6 Comparisons to previous results

This section provides comparisons between intrinsic properties measured in this work and those obtained in N05. In this work the total HI mass (M_{HI}) for each galaxy was determined from the HI total intensity map, which is the sum of the integrated flux in the total integrated map. N05 derived their HI masses as the sum of the integrated flux from the HI global profile. Shown in column 9 of Table 2.3 are HI masses for all galaxies in the sample in this work. HI masses obtained in this work are higher than those obtained in N05. In top left panel of Figure 2.6 shows the comparison between M_{HI} in this work and N05. The systemic velocities (V_{sys}) in this work were measured from the HI global profile as the average of the profile edges at 50% levels. Shown in column 6 of Table 2.3 is the V_{sys} for each galaxy in the sample. In top right panel of Figure 2.6 shows the comparison between V_{sys} in this work and N05. The total HI integrated map in this work were generated as the summation of the fitted Gaussian over the total emission in each channel. Shown in column 8 of Table 2.3 is the total integrated HI flux (S_{ν}). In bottom left panel of Figure 2.6 shows the comparison between the total integrated flux S_{ν} in this work and N05, the values obtained are higher compared to those obtained in N05. Shown in column 8 of Table 2.3 is S_{ν} of each galaxy measured in this work. In bottom right panel of Figure 2.6 shows the comparison between the 50% line width of HI global profile (W_{50}) in this work and N05. In this work W_{50} was measured as the difference between profile edges at 50% levels. The W_{50} measurements from this work are lower to those obtained in N05, this is because of asymmetric in HI global profiles. Shown in column 7 of Table 2.3 is line width of HI global profile for each galaxy.

To quantify the relationship between the intrinsic properties obtained in this work and N05, the Pearson's R statistic was used to calculate the correlation coefficient. Pearson's correlation coefficient formula is given by,

$$r = \frac{N \sum xy - (\sum x)(\sum y)}{\sqrt{[N \sum x^2 - (\sum x)^2][N \sum y^2 - (\sum y)^2]}} \quad (2.3)$$

where N is number of pair of scores, $\sum xy$ is the sum of the products of pair scores, $\sum x$ is the sum of the x scores, $\sum y$ is the sum of the y scores, $\sum x^2$ is the sum of squared x scores, and $\sum y^2$ is the sum of squared y scores. The coefficient value range between -1 and 1. The negative range values indicates negative correlation (i.e. one value decreases and the other increases) between variables and positive range indicates positive correlation between variables (i.e. both variable decrease or increase together).

In each panel of Figure 2.6, a strong positive correlation between the measurements in this work and those obtained by N05 is observed. The correlation coefficient r ranges from 0.9692 to 0.9999 for all intrinsic properties.

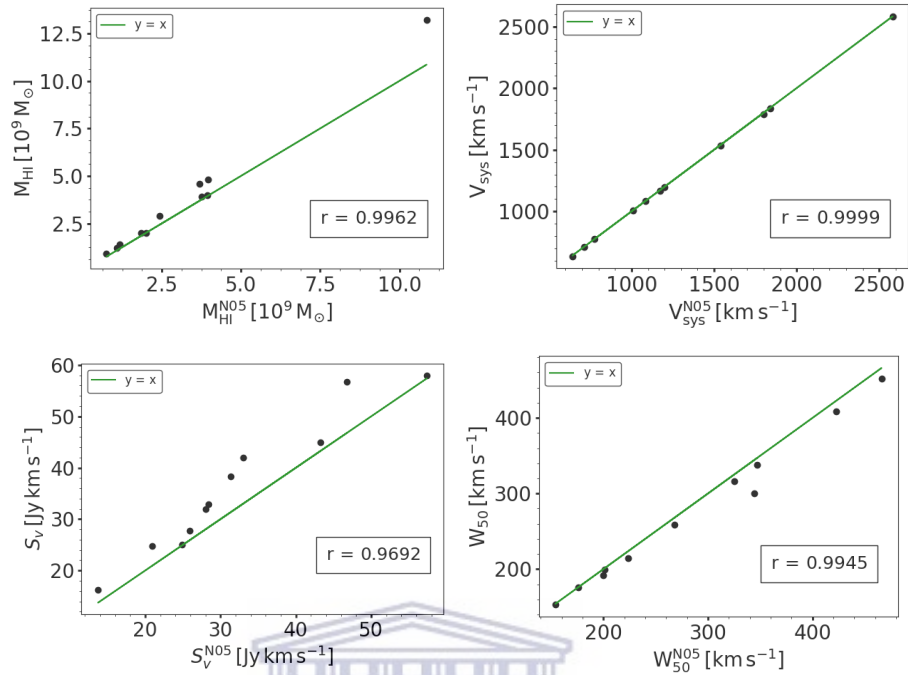


Figure 2.6: Intrinsic galaxies properties derived in this work compared with those obtained in N05. Top left panel shows the Total HI masses, top right panel shows systematic velocities, bottom left panel shows the HI total integrated fluxes, bottom right panel shows line width of global profiles at the 50%. The green line in all panels represents the line of equality. The legend in bottom right corner in all panels indicates the Pearson correlation coefficient (denoted by r) between the measurements obtained in this work and N05. The correlation coefficient value increase to ~ 1 . Clearly, there is a positive strong correlation between the measurements of intrinsic properties derived in this work and those obtained in N05.

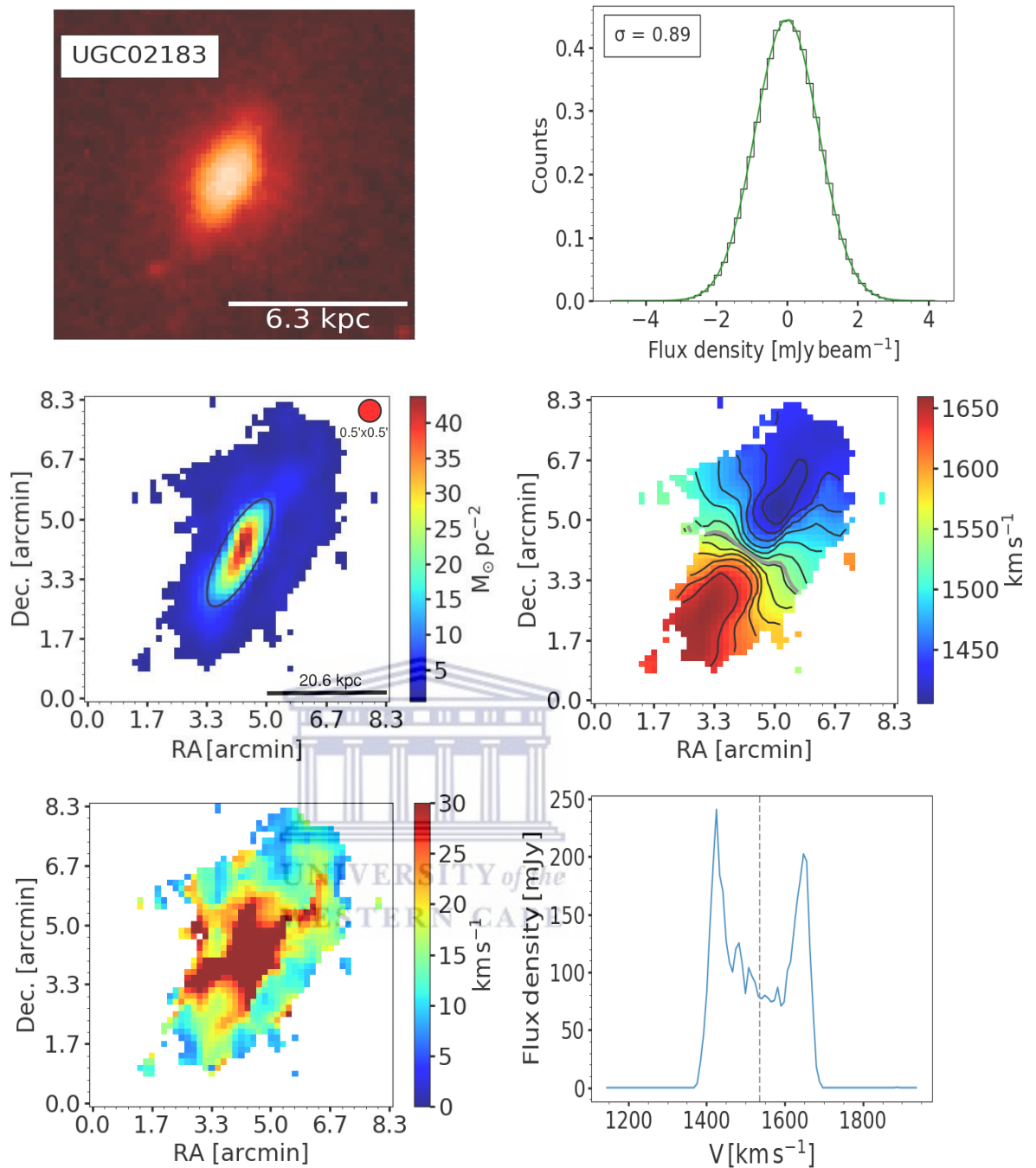


Figure 2.7: Top left panels: the first Digitized Sky Survey (DSS1) optical image. The angular size of each image in the optical is $2' \times 2'$. The ID is given in the upper left part. A scale in units of kiloparsec is indicated with white horizontal line in the bottom right. Top right panels: normalized histogram 200×200 noise pixels distribution, the legend on the upper left corner show 1σ noise level in channel maps in units of mJy beam^{-1} . Middle left panels: HI total intensity map. Black ellipse shown was used to obtain initial estimates for geometrical parameters for tilted-ring model discussed in next chapter. A scale in units of kiloparsec is indicated with black horizontal line in the bottom right. Beam size in units of arcmin(') is indicated with red filled circle in top right. Middle right panels: HI velocity field. The grey contour in the HI velocity field map represent systemic velocity (V_{sys}) and the black contours are spaced by 20 km s^{-1} . Bottom left panels: HI velocity dispersion map. Bottom right panels: HI global profile. Grey dotted line shown indicates systemic velocity.

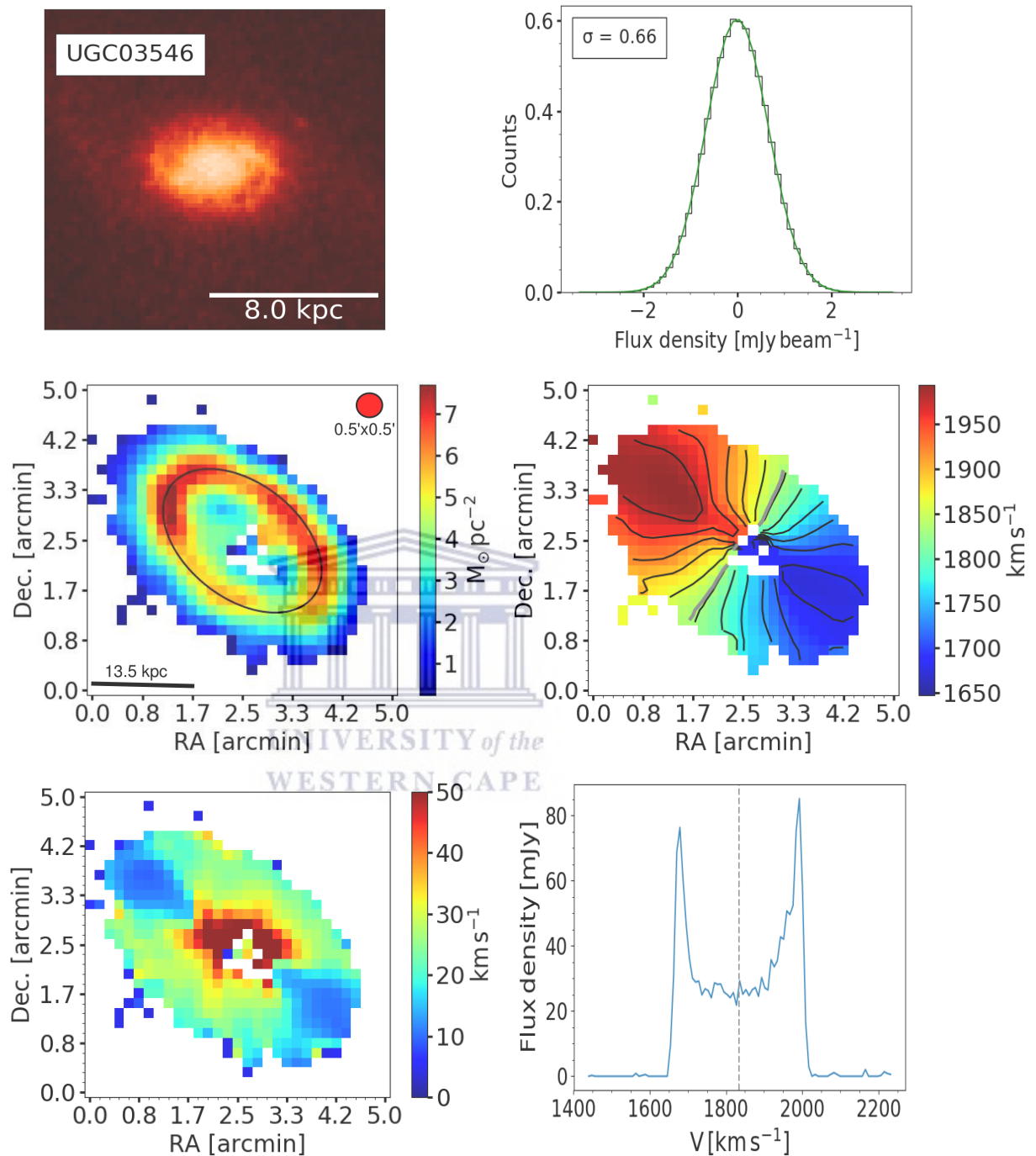


Figure 2.8: Images and derived profiles for UGC03546. A scale in units of kiloparsec is indicated with black horizontal line in the bottom right in HI total intensity map. The grey contour in the HI velocity field map represent systemic velocity (V_{sys}) and the black contours are spaced by 30 km s^{-1} . See Figure 2.7 caption for full details.

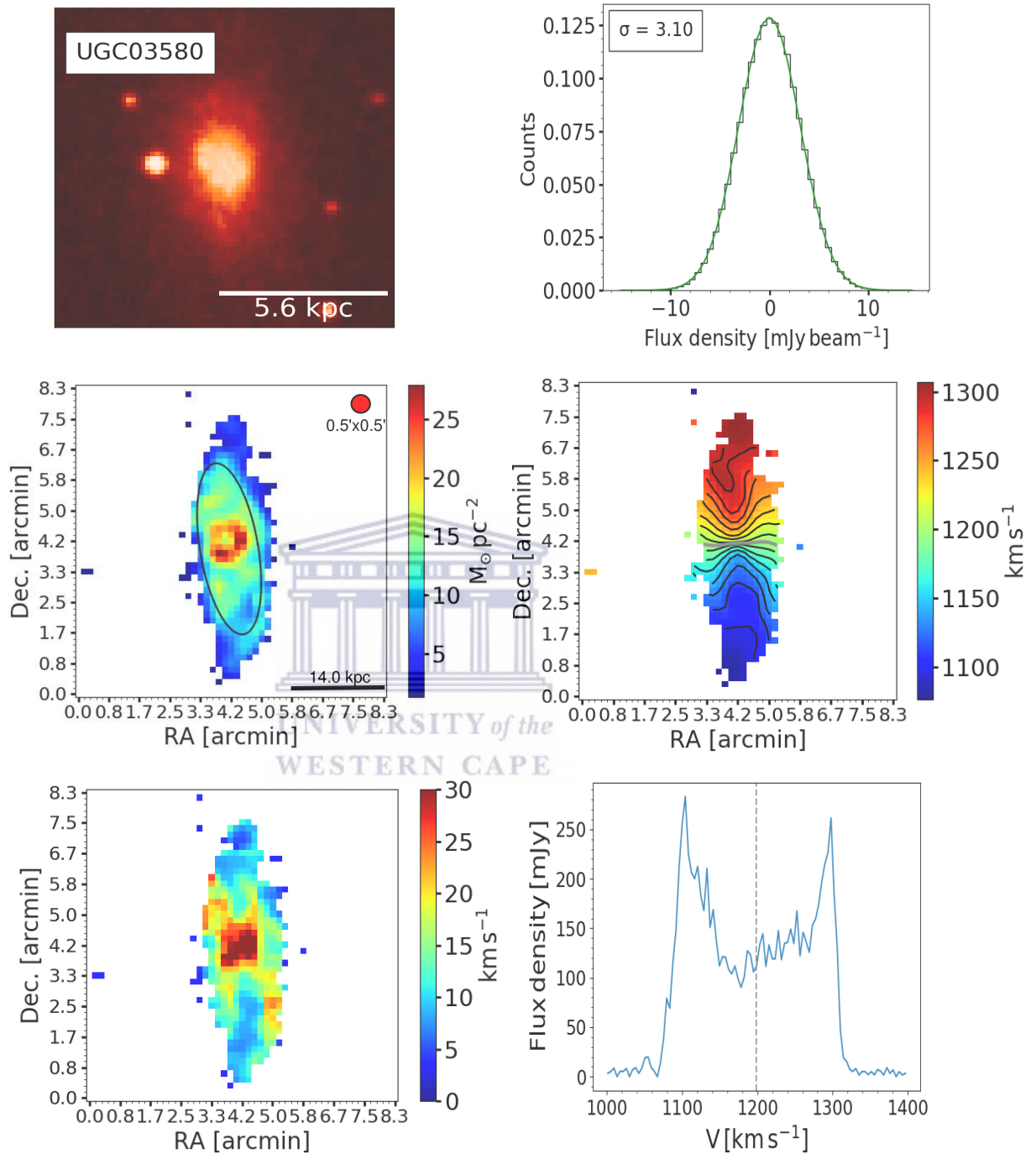


Figure 2.9: Images and derived profiles for UGC03580. The grey contour in the HI velocity field map represent systemic velocity (V_{sys}) and the black contours are spaced by 15 km s^{-1} . See Figure 2.7 caption for full details.

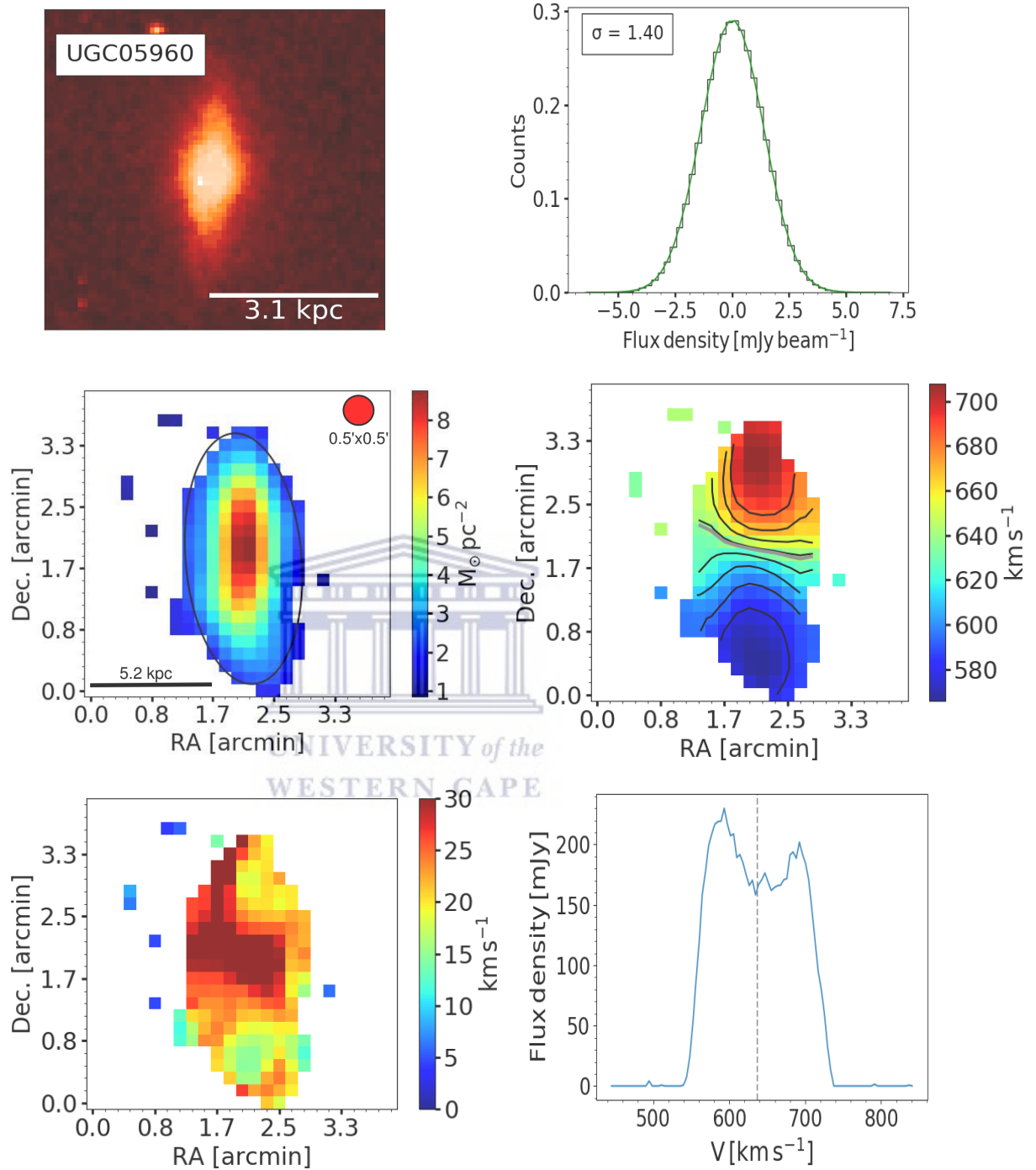


Figure 2.10: Images and derived profiles for UGC05960. A scale in units of kiloparsec is indicated with black horizontal line in the bottom right in HI total intensity map. The grey contour in the HI velocity field map represent systemic velocity (V_{sys}) and the black contours are spaced by 15 km s^{-1} . See Figure 2.7 caption for full details.

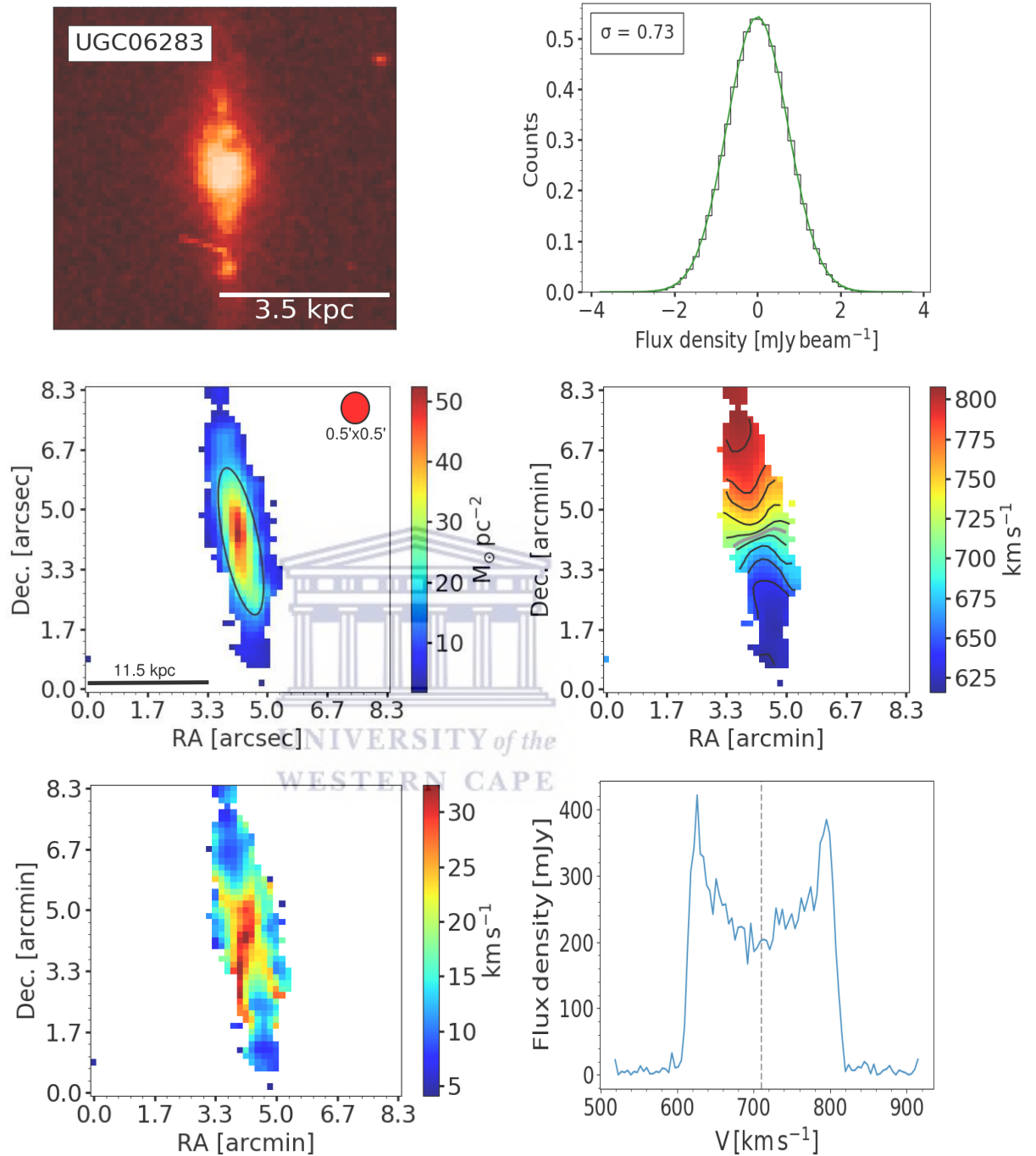


Figure 2.11: Images and derived profiles for UGC06283. A scale in units of kiloparsec is indicated with black horizontal line in the bottom right in HI total intensity map. The grey contour in the HI velocity field map represent systemic velocity (V_{sys}) and the black contours are spaced by 20 km s^{-1} . See Figure 2.7 caption for full details.

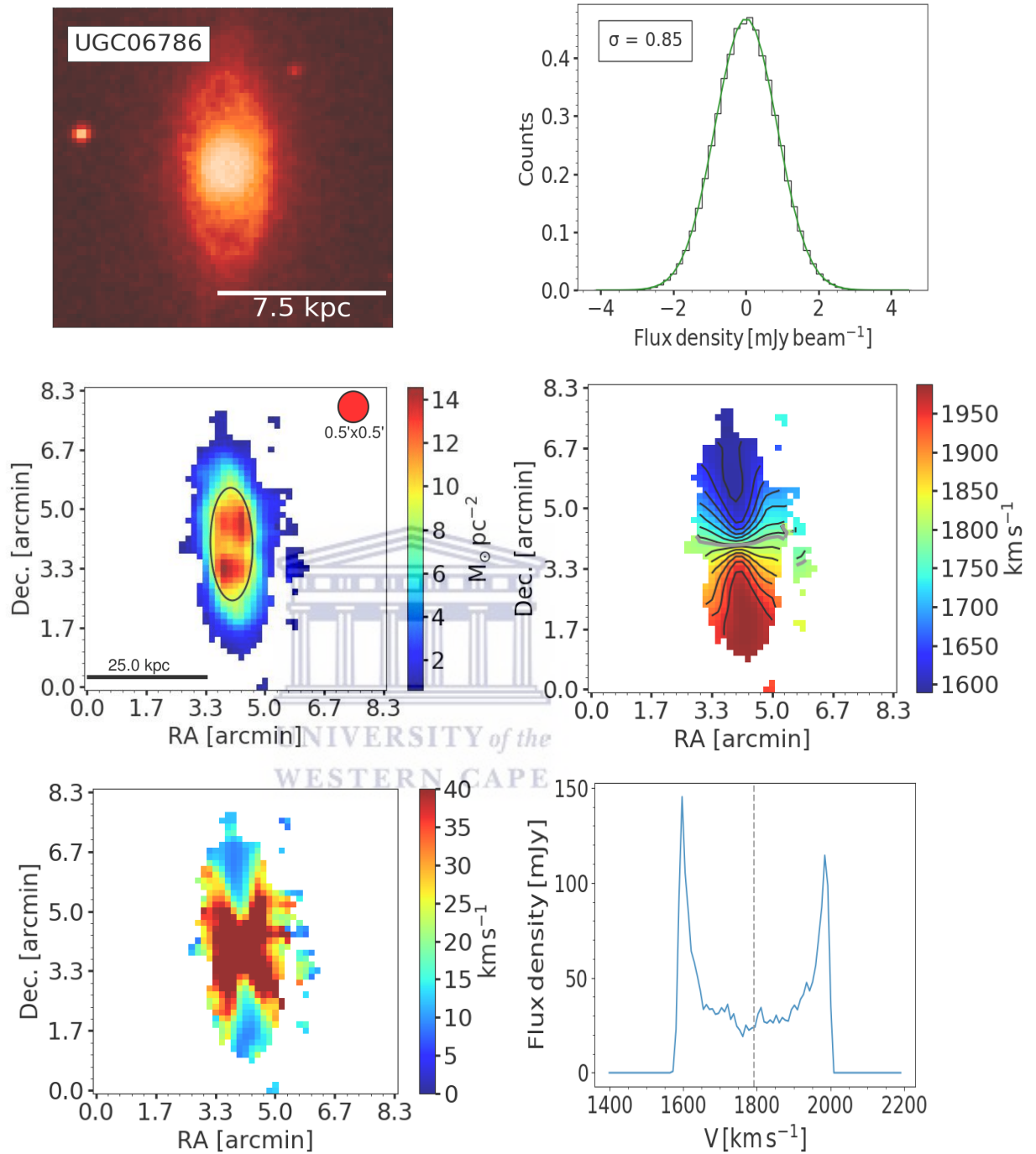


Figure 2.12: Images and derived profiles for UGC06786. A scale in units of kiloparsec is indicated with black horizontal line in the bottom right in HI total intensity map. The grey contour in the HI velocity field map represent systemic velocity (V_{sys}) and the black contours are spaced by 30 km s^{-1} . See Figure 2.7 caption for full details.

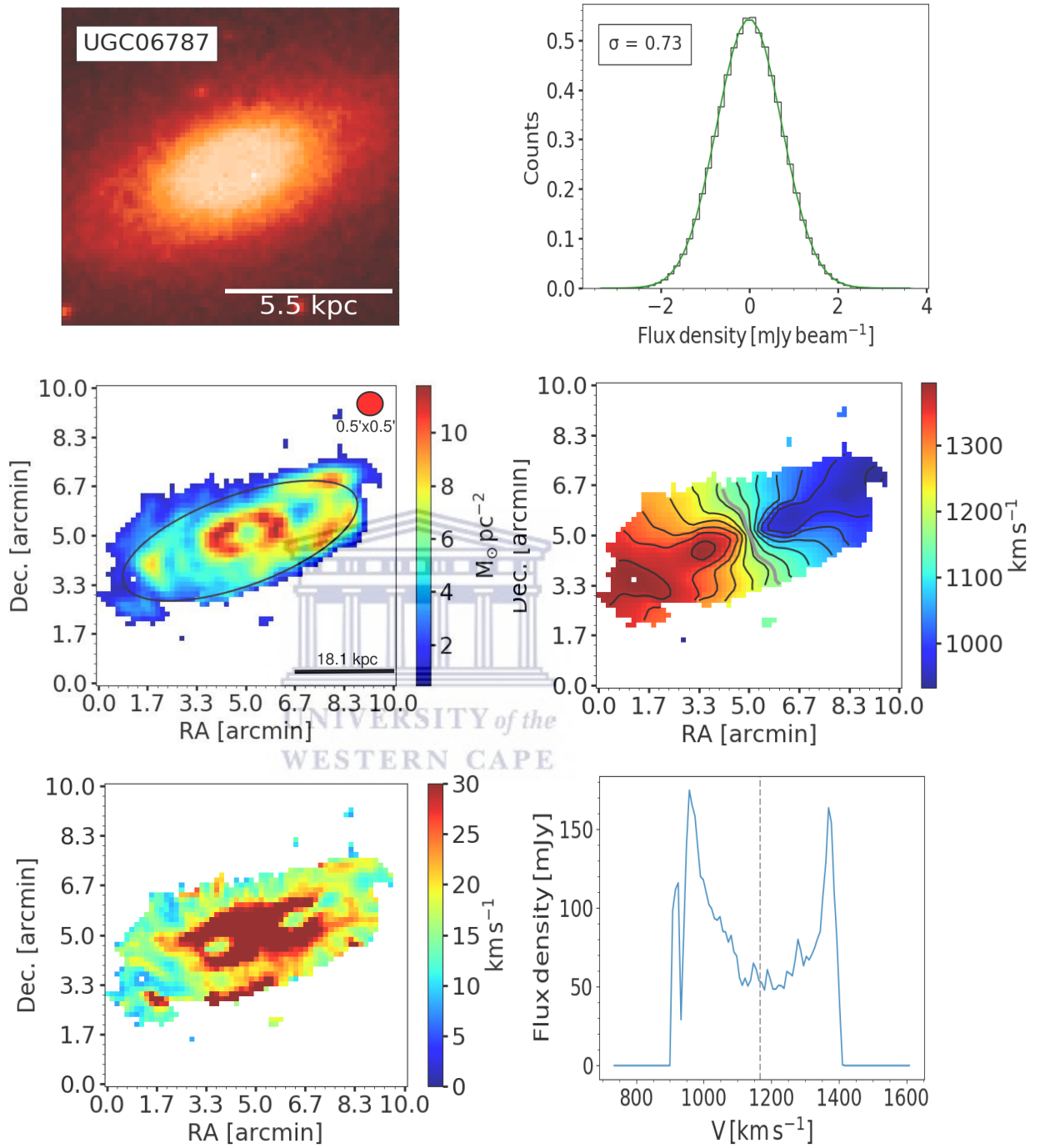


Figure 2.13: Images and derived profiles for UGC06787. The grey contour in the HI velocity field map represent systemic velocity (V_{sys}) and the black contours are spaced by 40 km s^{-1} . See Figure 2.7 caption for full details.

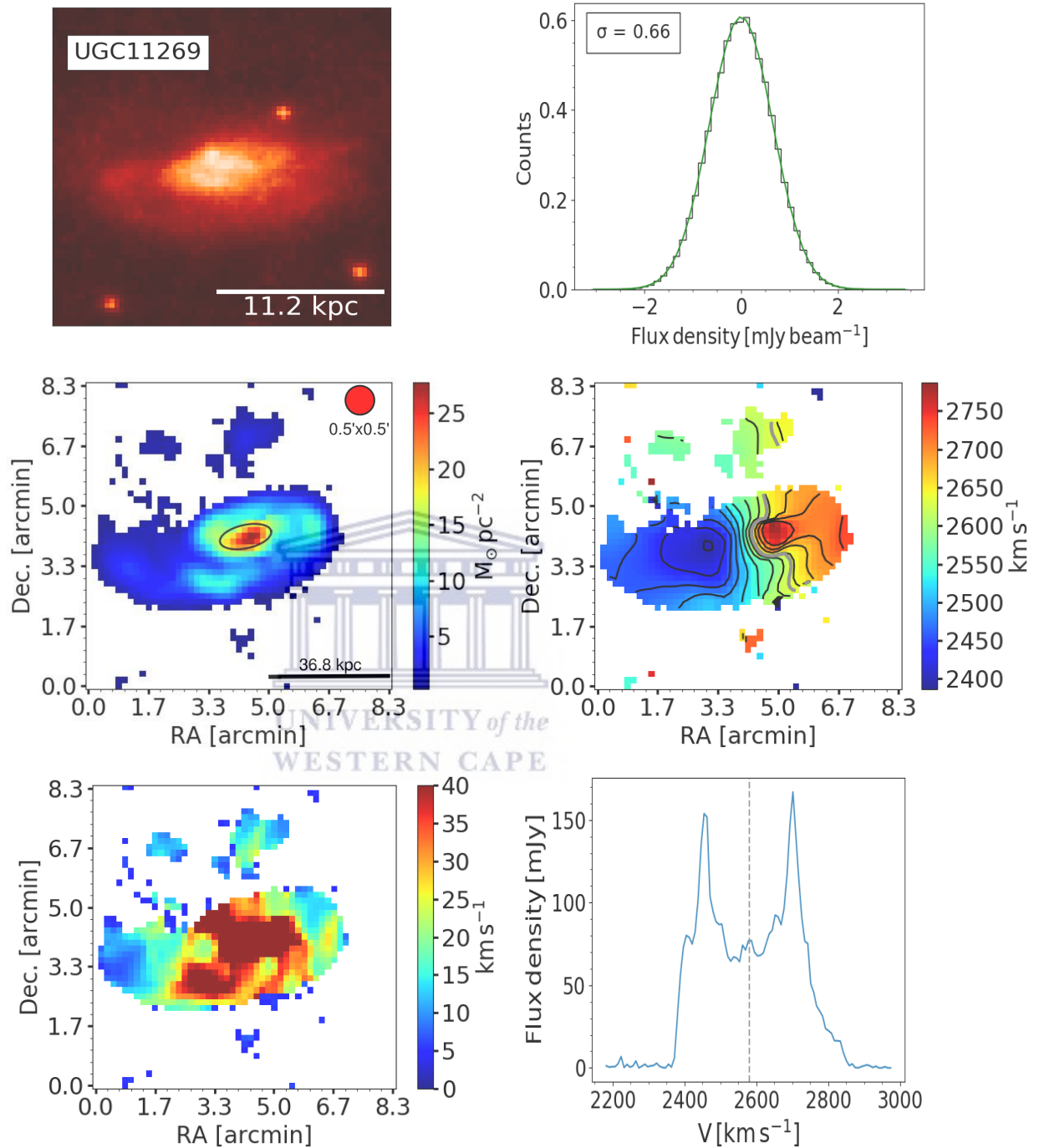


Figure 2.14: Images and derived profiles for UGC11269. The grey contour in the HI velocity field map represent systemic velocity (V_{sys}) and the black contours are spaced by 30 km s^{-1} . See Figure 2.7 caption for full details.

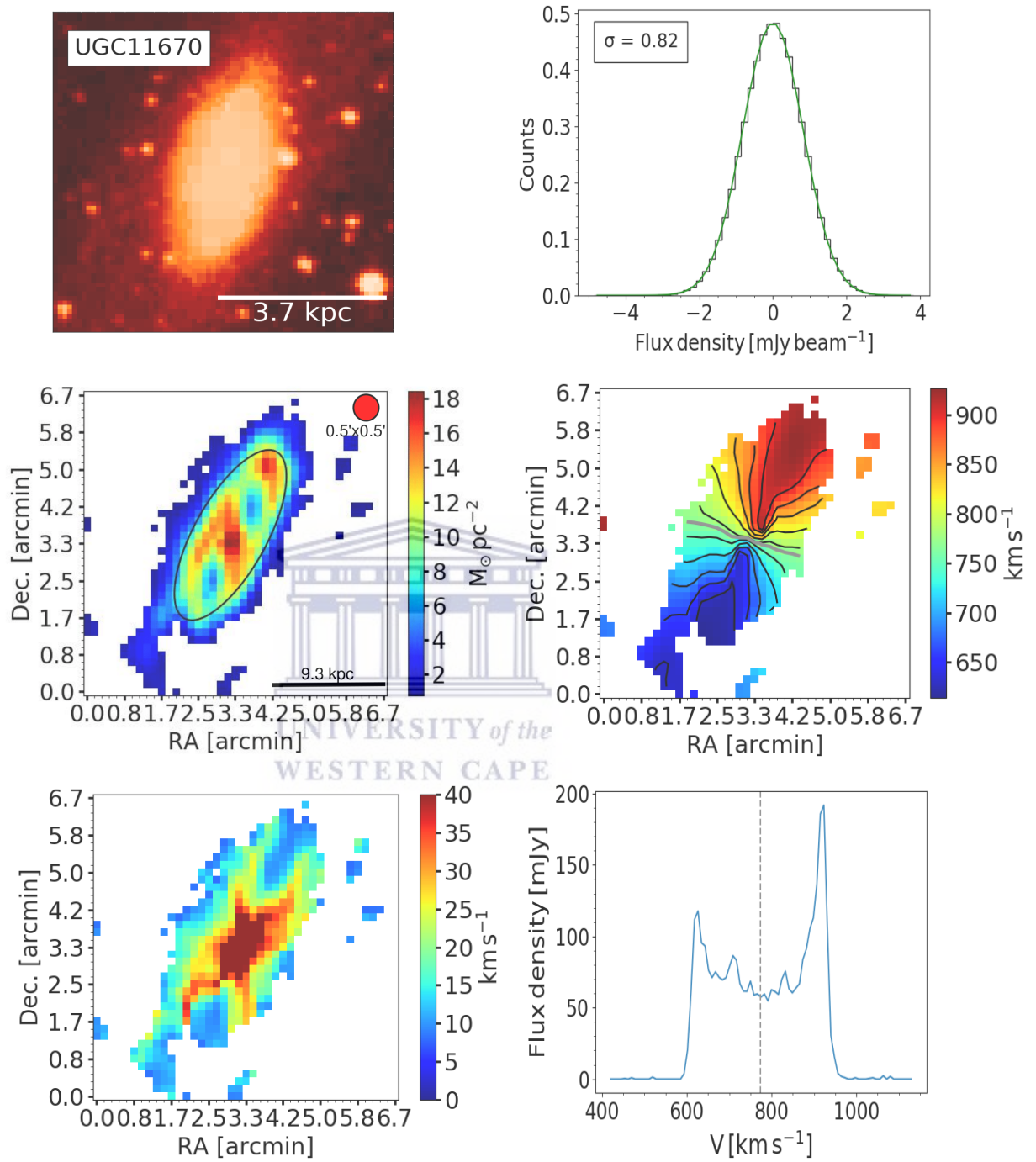


Figure 2.15: Images and derived profiles for UGC11670. The grey contour in the HI velocity field map represent systemic velocity (V_{sys}) and the black contours are spaced by 30 km s^{-1} . See Figure 2.7 caption for full details.

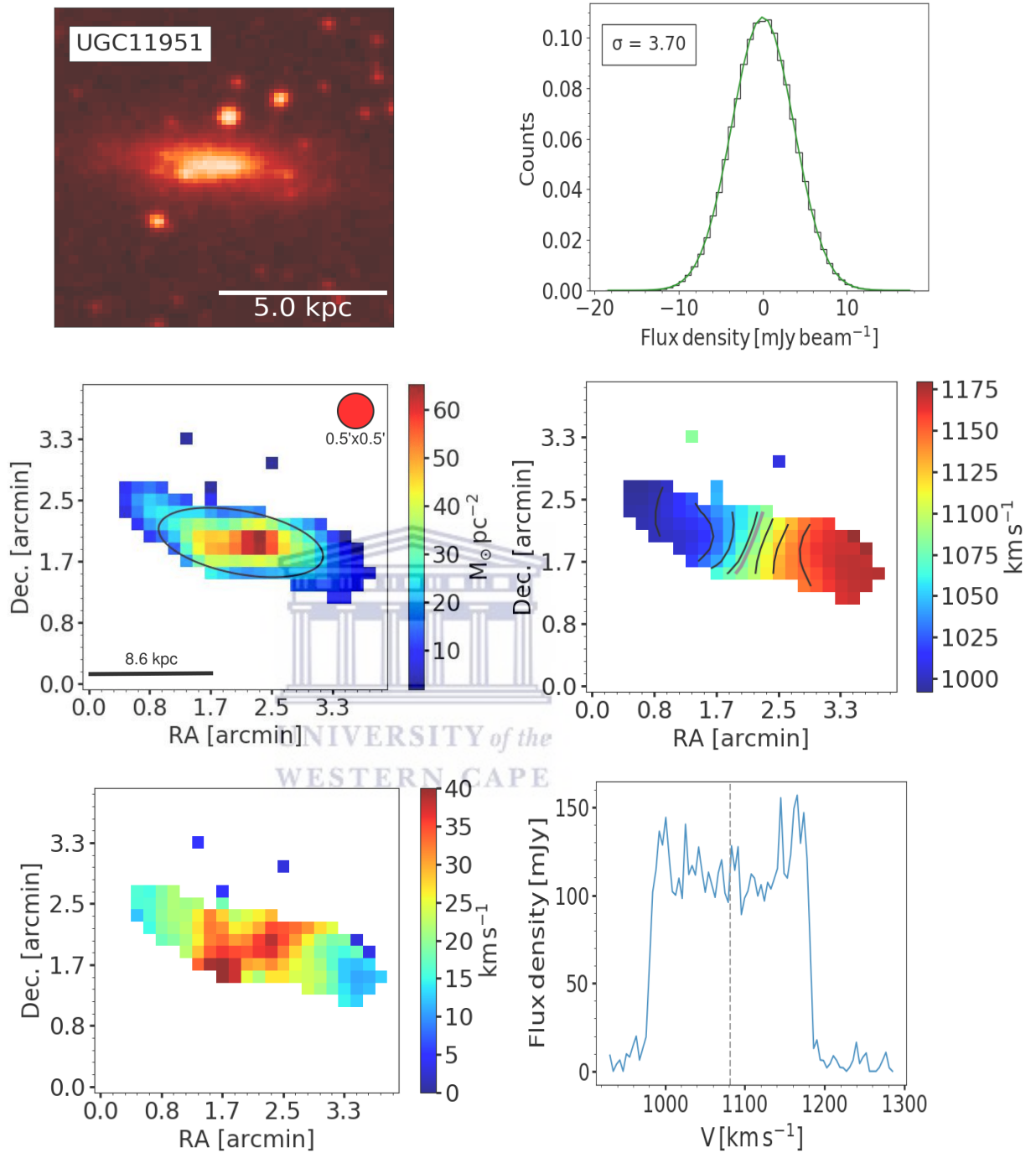


Figure 2.16: Images and derived profiles for UGC11951. A scale in units of kiloparsec is indicated with black horizontal line in the bottom right in HI total intensity map. The grey contour in the HI velocity field map represent systemic velocity (V_{sys}) and the black contours are spaced by 25 km s^{-1} . See Figure 2.7 caption for full details.

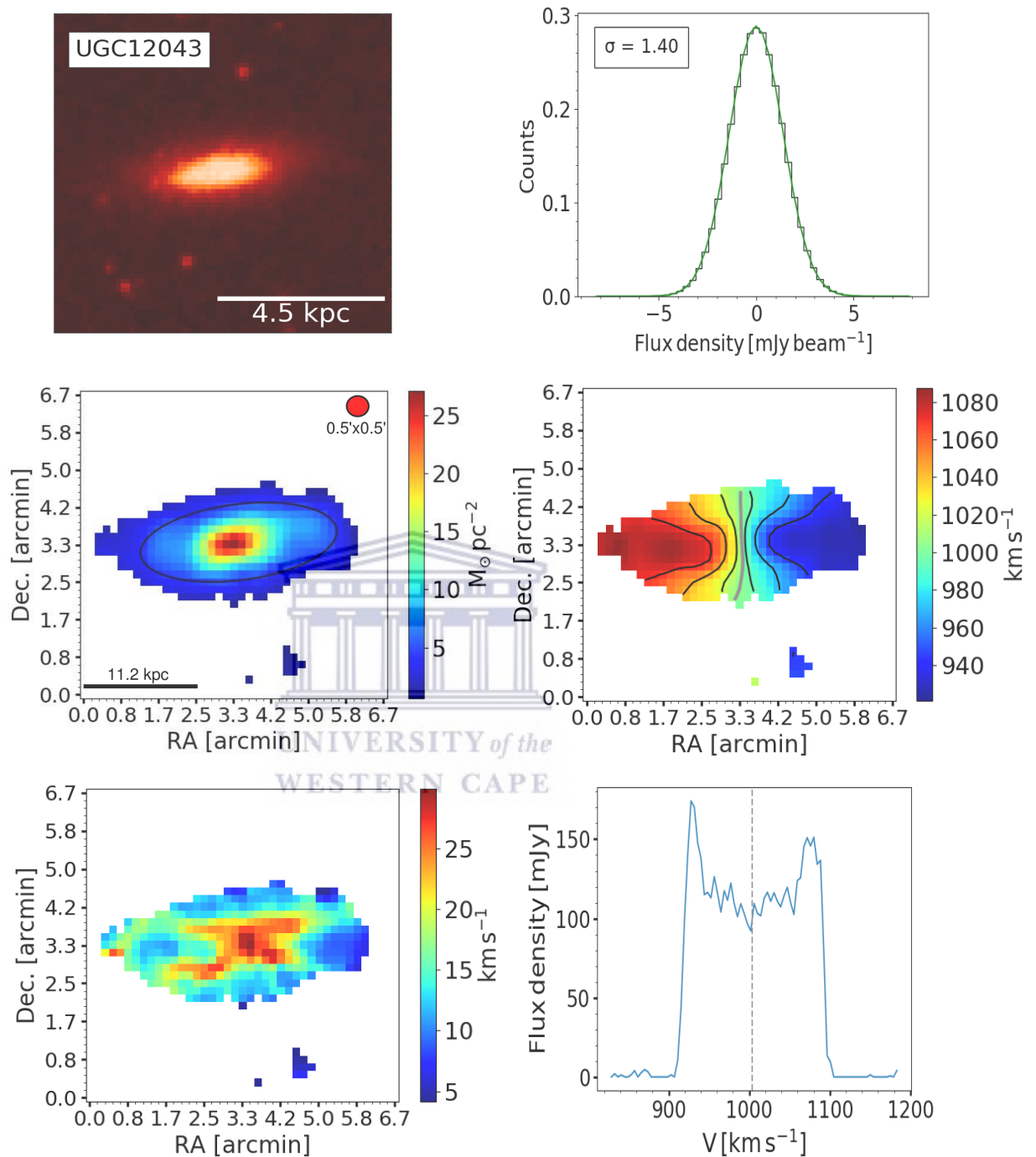


Figure 2.17: Images and derived profiles for UGC12043. A scale in units of kiloparsec is indicated with black horizontal line in the bottom right in HI total intensity map. The grey contour in the HI velocity field map represent systemic velocity (V_{sys}) and the black contours are spaced by 25 km s^{-1} . See Figure 2.7 caption for full details.

Chapter 3

Modelling and analysis

In this chapter the data products presented in chapter 2 are used to measure the total angular momentum content of each galaxy. In order to do this, the rotation curves and baryonic radial mass profiles of all galaxies are required. Section 3.1 of this chapter will discuss how HI mass surface density profiles for all galaxies from the sample were derived. Section 3.2 discuss how stellar mass surface density profiles were derived. Section 3.3 briefly discuss how the baryonic mass of each galaxy was calculated. Section 3.4 shows all mass profiles required in this study. Section 3.5 discuss how HI rotation curves for all galaxies in the sample were derived. It also details the methods used to compare the dynamical models to the data. Section 3.6 present total baryonic angular momentum measurements for each galaxy.

3.1 HI mass surface density profiles

The total HI intensity maps presented in chapter 2 section 2.5 were used to derive radial HI mass surface density profiles. Each galaxy was fragmented into concentric elliptical rings, using the orientation parameters derived from dynamical models fit to the HI velocity fields (see section 3.5). The width of each ring was set to be equal to half the spatial resolution of the data: half the synthetic beam size (i.e., $15''$). All blanked pixels were removed while the flux densities were azimuthally-averaged in concentric rings. All HI mass surface densities (Σ_{HI}) were inclination-corrected and scaled by a factor of 1.342 (Izotov et al., 2014) in order to account for the presence of helium (He) and fractions of other metals, such that $\Sigma_{\text{HI+He}} = 1.342 \times \Sigma_{\text{HI}}$. All $\Sigma_{\text{HI+He}}$ are shown as a red curve in left panels of figures 3.2 - 3.3.

The cumulative mass for HI and He within a galactocentric radius R was evaluated numerically using equation:

$$M_{\text{HI+He}} = \int_{15}^{R_{\text{out}}} \Sigma_{\text{HI+He}}(R) \cdot 2\pi R \cdot dR, \quad (3.1)$$

where R is galactocentric radius. $\Sigma_{\text{HI+He}}$ is the azimuthally-averaged surface density for HI and He in units of $M_{\odot} \text{pc}^{-2}$. Each profile was evaluated from an inner radius of 15 arcsec (i.e., one ring width). The total HI and He mass comes from setting the lower integration limit and upper limit of equation 3.1 to 15 arcsec and R_{out} , respectively. R_{out} is the radius at which Σ_{HI} drops to $1 M_{\odot} \text{pc}^{-2}$. All cumulative mass profiles are shown as a red curve in right panels of Figures 3.2 - 3.3.

3.2 Stellar mass surface density profiles

Stellar mass surface brightness profiles were obtained from WISE $3.4 \mu\text{m}$ imaging. Measured $3.4 \mu\text{m}$ surface brightness profiles were provided by Prof T. Jarrett (private communication) and converted from units of apparent magnitudes per arcsec² to absolute magnitudes per arcsec² using Equation 3.2,

$$M = m - 5\log_{10}D + 5, \quad (3.2)$$

where m is the apparent magnitude, M is the absolute magnitude, and D is the distance in units of parsecs (pc).

Then knowing that $W1_{\odot} = 3.24$ (Cluver et al., 2014) is the WISE W1 absolute magnitude of the Sun, the surface brightness profiles were converted from units of mag arcsec⁻² to $L_{\odot} \text{arcsec}^{-2}$ using Equation 3.3,

$$L_{\star} = 10^{\left(\frac{W_{\odot}-M}{2.5}\right)}. \quad (3.3)$$

Stellar mass content is best probed in infrared wavelengths (e.g., Verheijen 2001). Over the broad range of galaxy masses and different morphology the stellar masses at 3.4 microns remain nearly constant. This work assumed a constant stellar mass-to-light ratio of $0.47 \frac{M_{\odot}}{L_{\odot}}$ (e.g., McGaugh and Schombert 2014) at $3.4 \mu\text{m}$ for all the galaxies in the sample.

Surface brightness profiles obtained using Equation 3.3 together with an assumed mass-to-light ratio $\left(\frac{M}{L}\right)$ of $0.47 \frac{M_{\odot}}{L_{\odot}}$ were used to generate a stellar mass surface density profile for each galaxy, $\Sigma_{\star}(R)$, using the Equation 3.4,

$$\Sigma_{\star} = \frac{M}{L} \times L_{\star}, \quad (3.4)$$

where L_{\star} is the stellar luminosity profile obtained from Equation 3.3. The known distance of each galaxy (e.g., Noordermeer et al. 2005) was used to convert from units of $M_{\odot} \text{ arcsec}^{-2}$ to $M_{\odot} \text{ pc}^{-2}$ using Equation 3.4 were converted from units of $M_{\odot} \text{ arcsec}^{-2}$ to $M_{\odot} \text{ pc}^{-2}$. These profiles are shown as blue curves in left panels of Figures 3.2 - 3.3.

For each galaxy, the total stellar mass was calculated numerically by evaluating the following integral:

$$M_{\star} = \int_{15}^{R_{\text{out}}} \Sigma_{\star}(R) \cdot 2\pi R \cdot dR, \quad (3.5)$$

where Σ_{\star} is the stellar mass surface density in an anullus in units of $M_{\odot} \text{ arcsec}^{-2}$, R is the radius in units of arcsec, and dR is the width of an anullus in units of arcsec. It is clear that the Σ_{HI} profiles and Σ_{\star} profiles were sampled at two different sets of galactocentric radii. To make M_{\star} profiles, Equation 3.5, directly comparable to the $M_{\text{HI+He}}$ profiles, M_{\star} profiles were interpolated onto the set of galactocentric radii used for $M_{\text{HI+He}}$ profiles. Then the total stellar mass comes from setting the upper and lower integration limits in Equation 3.5 to $15''$ and R_{out} , respectively. Where R_{out} is the radius at which $\Sigma_{\text{HI+He}}$ drops to $1 M_{\odot} \text{ pc}^{-2}$. All stellar cumulative mass profiles are shown as blue curves in right panels of Figures 3.2 - 3.3.

WESTERN CAPE

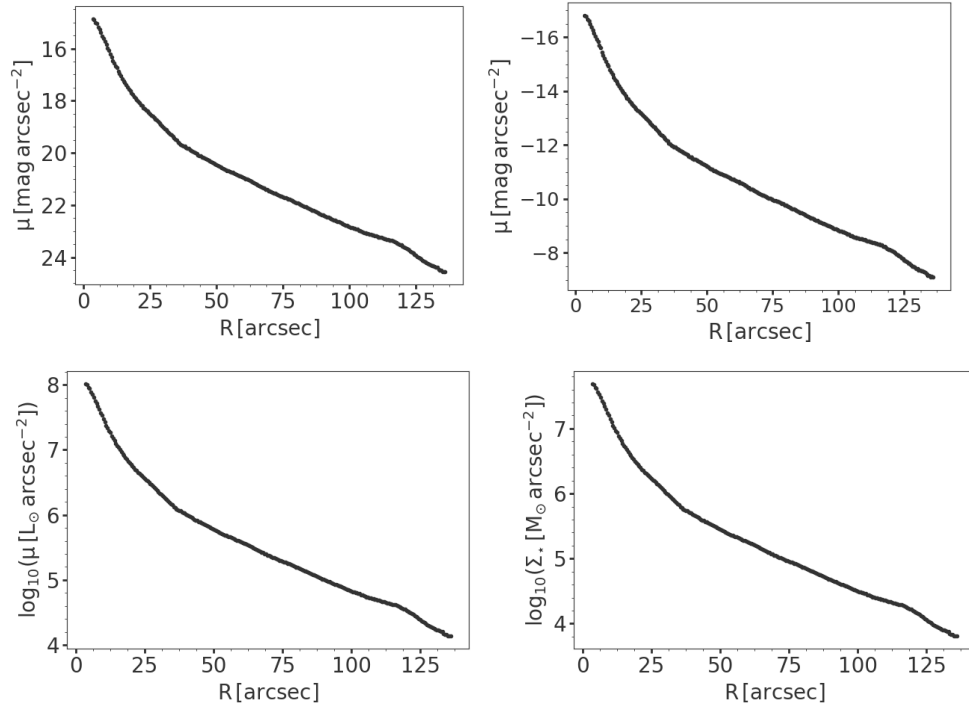


Figure 3.1: This illustrates how all stellar surface brightness profiles were converted to different units using UGC02183. Top left panel show surface brightness in units of apparent magnitudes per arcsec². Top right panel shows stellar surface brightness in units of absolute magnitudes per arcsec². Bottom left panel shows stellar surface brightness in units of L_{\odot} arcsec⁻². Then bottom right panel shows stellar surface brightness in units of M_{\odot} pc⁻².

UNIVERSITY of the

3.3 Baryonic mass surface density profiles

Total baryonic mass (M_b) for each galaxy was evaluated numerically using the following integral:

$$M_b = \int_{15}^{R_{out}} \Sigma_b(R) \cdot 2\pi R \cdot dR, \quad (3.6)$$

where R is galactocentric radius. Σ_b is the azimuthally-average baryonic mass surface density. In this work the azimuthally-average baryonic mass surface density is presented by $\Sigma_b(R) = \Sigma_{HI+He}(R) + \Sigma_{\star}(R)$. Then the total baryonic mass comes from setting the upper and lower integration limits in Equation 3.3 to 15'' and R_{out} , respectively. Where R_{out} is the radius at which Σ_{HI+He} drops to $1 M_{\odot} \text{pc}^{-2}$. All baryonic mass surface densities and cumulative baryonic mass profiles are shown as a black curve in left and right panels of Figures 3.2 - 3.3, respectively.

3.4 Summary of all mass surface density profiles

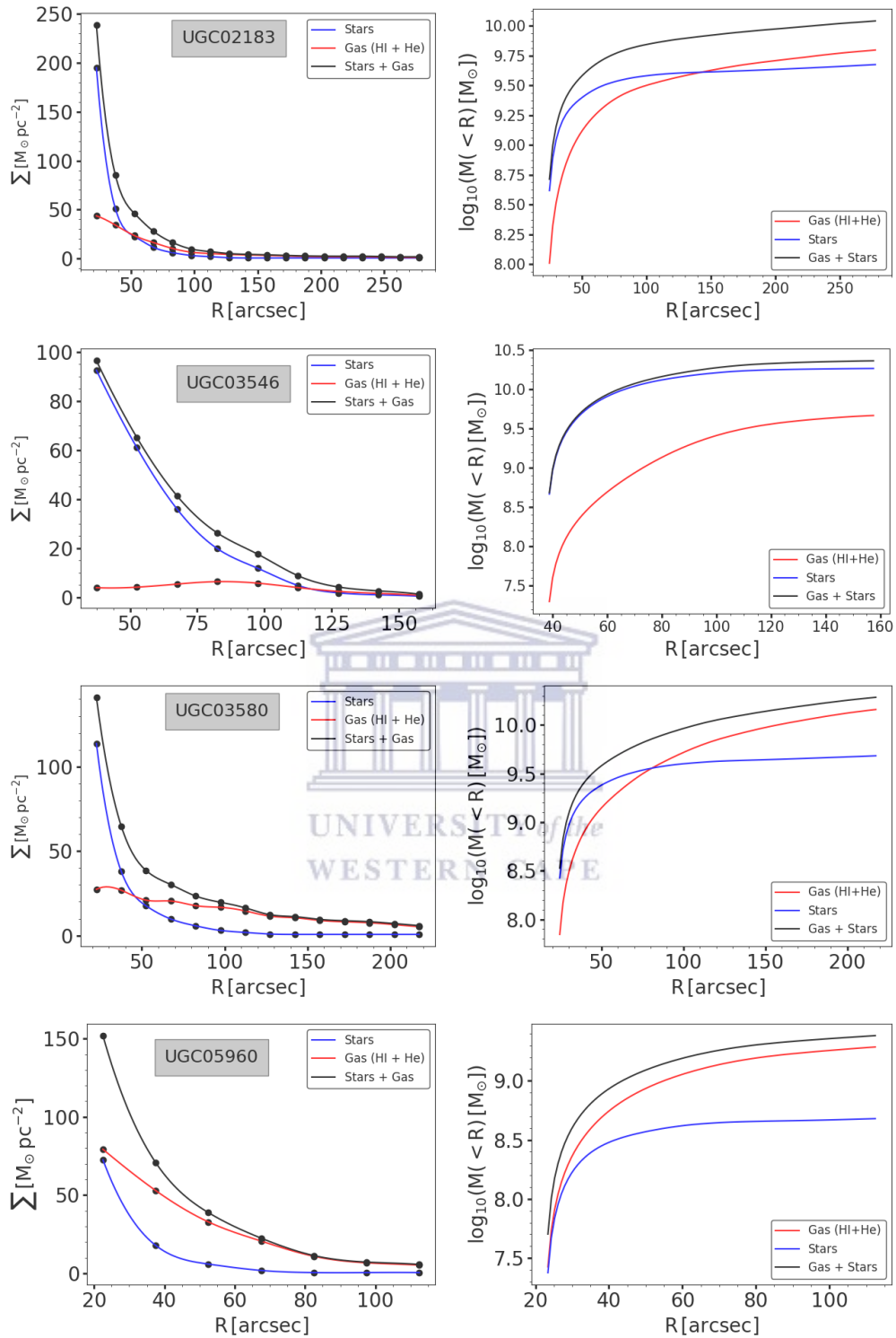


Figure 3.2: Mass profiles derived and used in this work. In the left panels, azimuthally-averaged mass surface density profiles for the gas, stars, and baryons are shown as the red, blue, and black curves, respectively. In the right panels, cumulative mass profiles for the gas, stars, and baryons are shown as the red, blue, and black curves, respectively. For all galaxies, it is clear that the baryon mass is dominated by gas at outer radii.

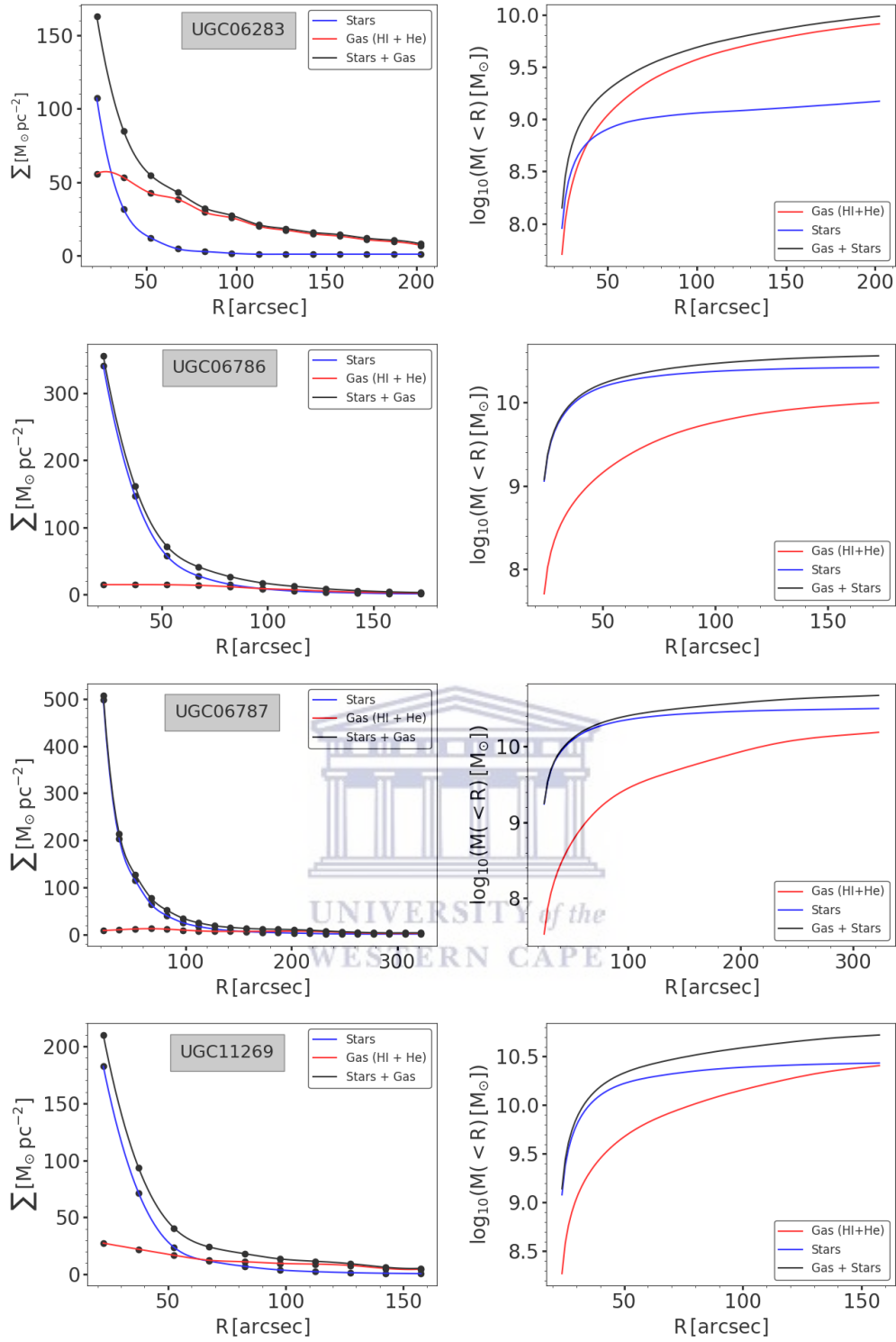


Figure 3.3: Mass profiles derived and used in this work continued. See Figure 3.2 caption for full details.

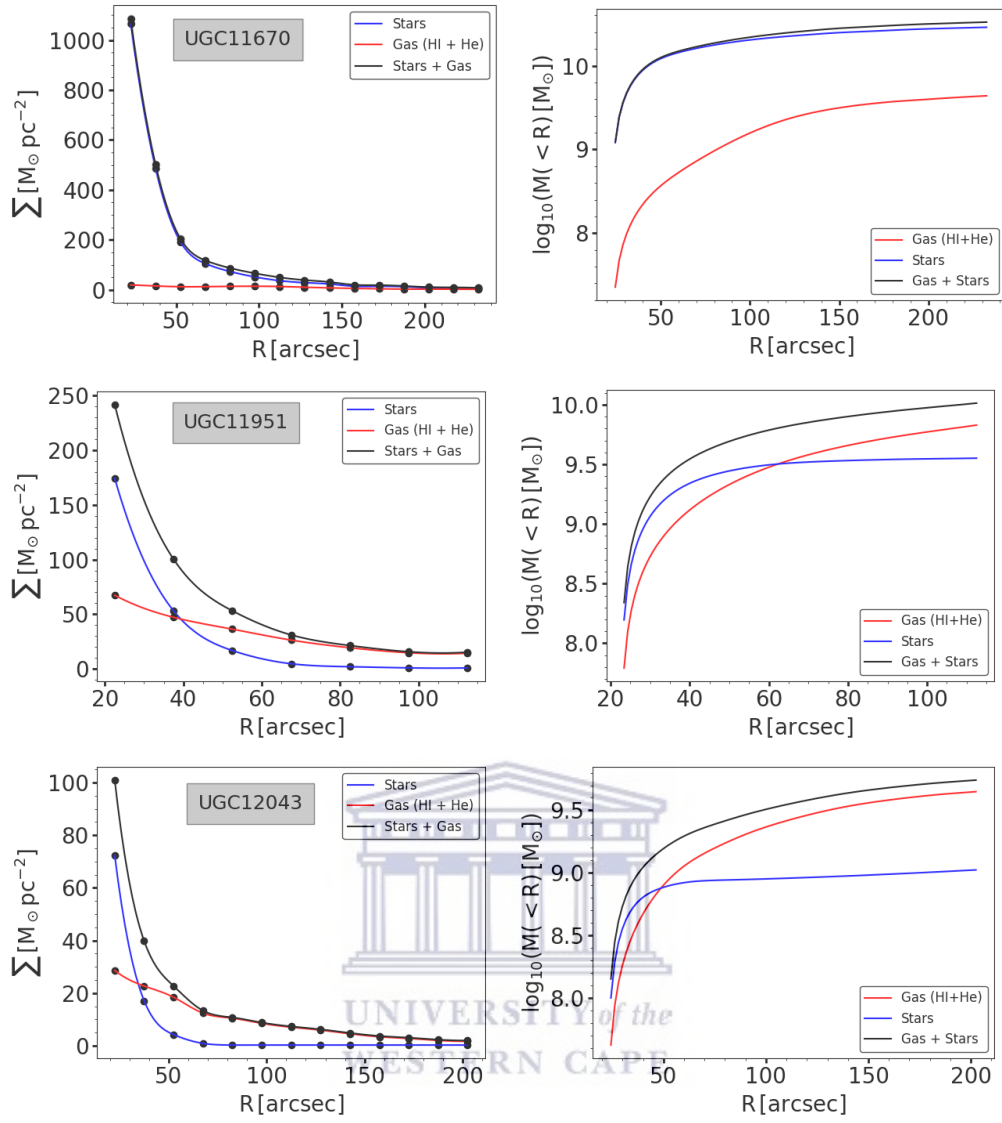


Figure 3.4: Mass profiles derived and used in this work continued. See Figure 3.2 caption for full details.

3.5 HI rotation curves

A traditional standard procedure to model gas kinematics in disk galaxies known as tilted ring modelling was performed to determine the rotational characteristics of the gas in each galaxy. This method was originally introduced by Rogstad et al. (1974), assuming that the galactic gas disk can be represented by a series of concentric rings each described by their own orientation and kinematic parameters; center position (x_c, y_c) , systemic velocity (V_{sys}), inclination (i), position angle (PA), and the rotation velocity (V_{rot}). The gas in concentric rings is assumed to be in purely circular motion. For any spatial position (x, y) in each ring with radius R the line-of-sight velocity is given by,

$$V_{\text{los}}(x, y) = V_{\text{sys}} + V_{\text{rot}}(R) \sin(i) \cos(\theta), \quad (3.7)$$

where θ is position angle with respect to the receding axis measured in the galactic plane. The true PA and i in the sky plane is related to equations,

$$\cos(\theta) = \frac{-(x - x_c) \sin(PA) + (y - y_c) \cos(PA)}{R}, \quad (3.8)$$

$$\sin(\theta) = \frac{-(x - x_c) \cos(PA) + (y - y_c) \sin(PA)}{R \cos(i)}, \quad (3.9)$$

where PA is measured anti-clockwise between north direction on the sky and the major axis of the receding half of the galaxy. This modelling deduce the variation of the rotation velocity of the gas disk with radius by performing a least-squares algorithm to the velocity field until an optimum fit is executed.

The ROTCUR routine in GIPSY package (Van der Hulst et al., 1992) has been used to generate a rotation curve of each galaxy in two iterations by fitting both halves (receding and approaching side) of each galaxy. The width of each ring was set at half the size of the HI beam. The radial velocities in each ring are weighted with $|\cos\theta|$ and points within a given angle from the minor axis, typically $15^\circ - 30^\circ$, are completely not considered to avoid errors that rise from deprojection. In the first iteration of ROTCUR run, all parameters were set free. Initial estimates for the systemic velocity were determined from the HI global profiles, while position angle, inclination, and dynamical centre for each galaxy were determined by fitting an ellipse to a thin ribbon of the HI flux emission in the outer disk.

These ellipses are shown as black ribbons in the total HI intensity maps presented in chapter 2 middle left panels of Figures 2.7 - 2.17. In all iterations, the expansion velocity was kept fixed at 0 km s^{-1} and all parameters were allowed to be free.

In the second iteration of ROTCUR run, All best-fitting values for all parameters (except rotation velocity) were set to median values in all radii from the previous iteration. An attempt to correct for non-circular, random motions in velocity field was not performed. The HI velocity fields presented in chapter 2 were used with ROTCUR to derive rotation curves for galaxies in this work. Shown in Figures 3.5 - 3.5 are the HI rotation curves for all galaxies in the sample which were used to calculate the angular momentum content.

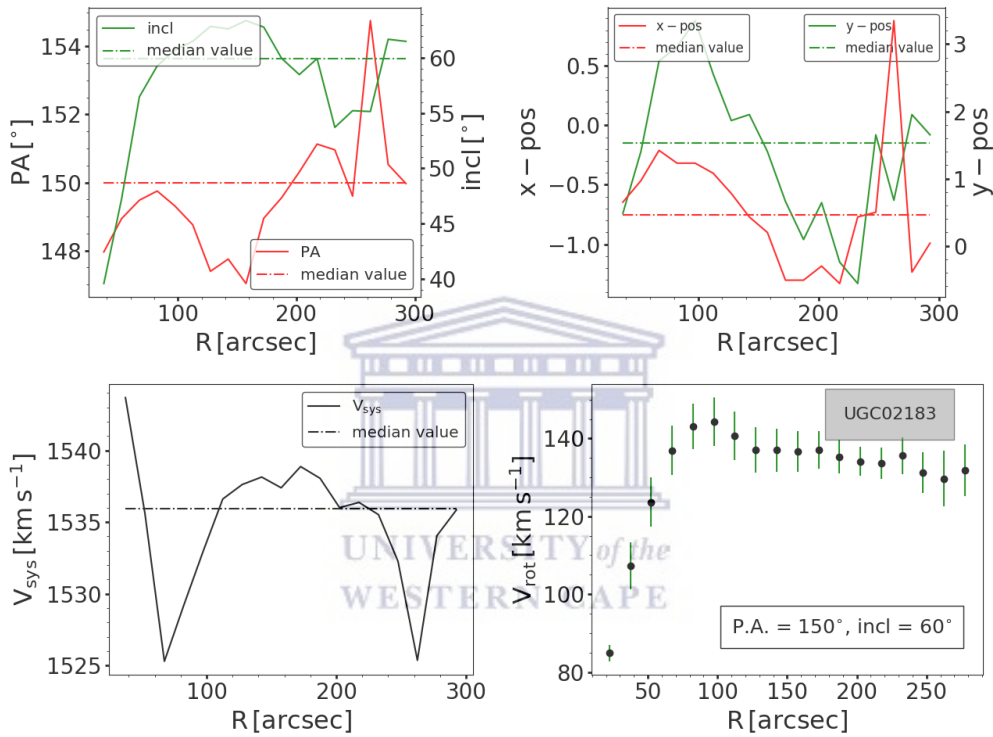


Figure 3.5: The radial variation of all parameters as a function of radius from ROTCUR iterations. In the top left panels, radial variation of position angle (PA) and inclination angle (incl) are shown as red and green curves when all parameters are set free, respectively. Dash-dotted red and green lines shows median values for PA and incl, respectively. Median values of PA and incl were used for the second ROTCUR iterations. In the top right panels, radial variation of center coordinates x_c and y_c are shown as red and green curves when all parameters are set free, respectively. Units for x_c and y_c are pixel. Median values of x_c and y_c were used for the second ROTCUR iterations. The bottom left panels shows the radial variation of systemic velocity (V_{sys}). Median values of V_{sys} were used in the second ROTCUR iteration and are indicated by a dash-dotted black lines. Bottom right panels shows HI rotation curves from tilted ring models fit to the HI velocity fields presented in section 2.7 - 2.17 of chapter 2. Filled black circles represent the average circular velocity in a ring of width 15 arcsec. Green error bars represented the standard deviation of the circular velocities in a ring.

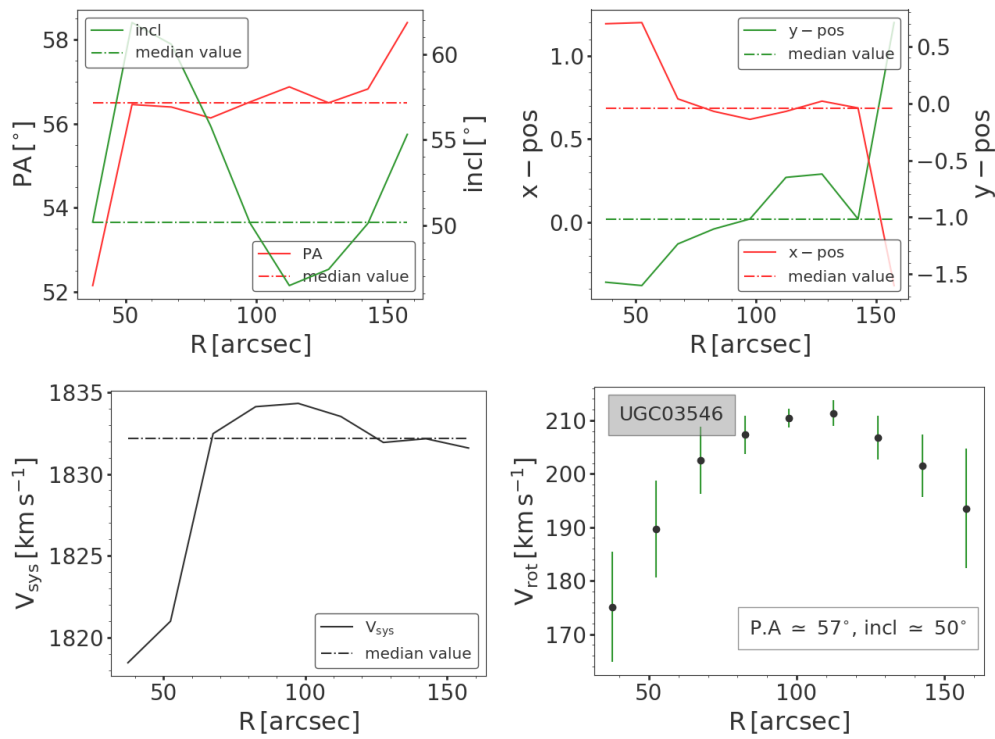


Figure 3.6: Full tilted ring model for UGC03546. See Figure 3.5 caption for full details.

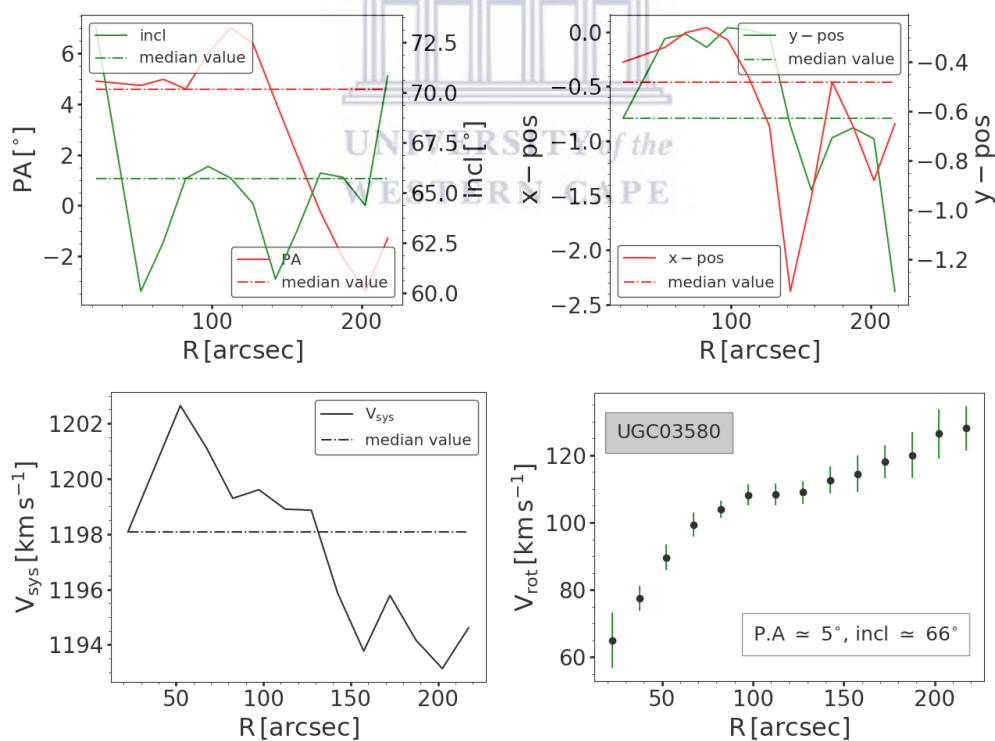


Figure 3.7: Full tilted ring model for UGC03580. See Figure 3.5 caption for full details.

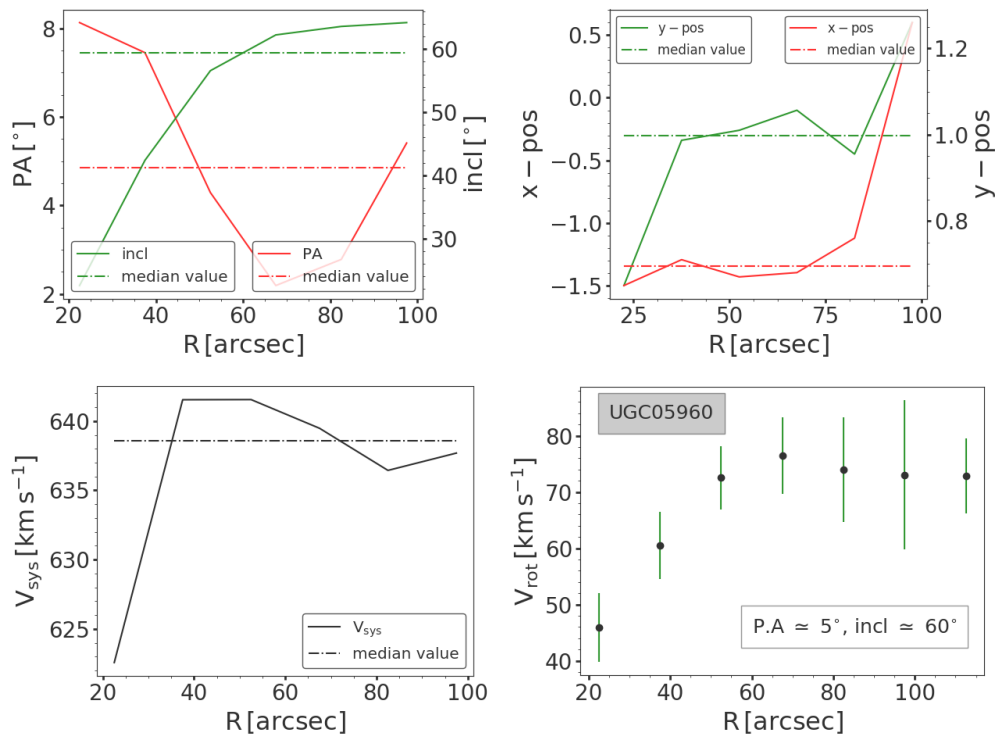


Figure 3.8: Full tilted ring model for UGC05960. See Figure 3.5 caption for full details.

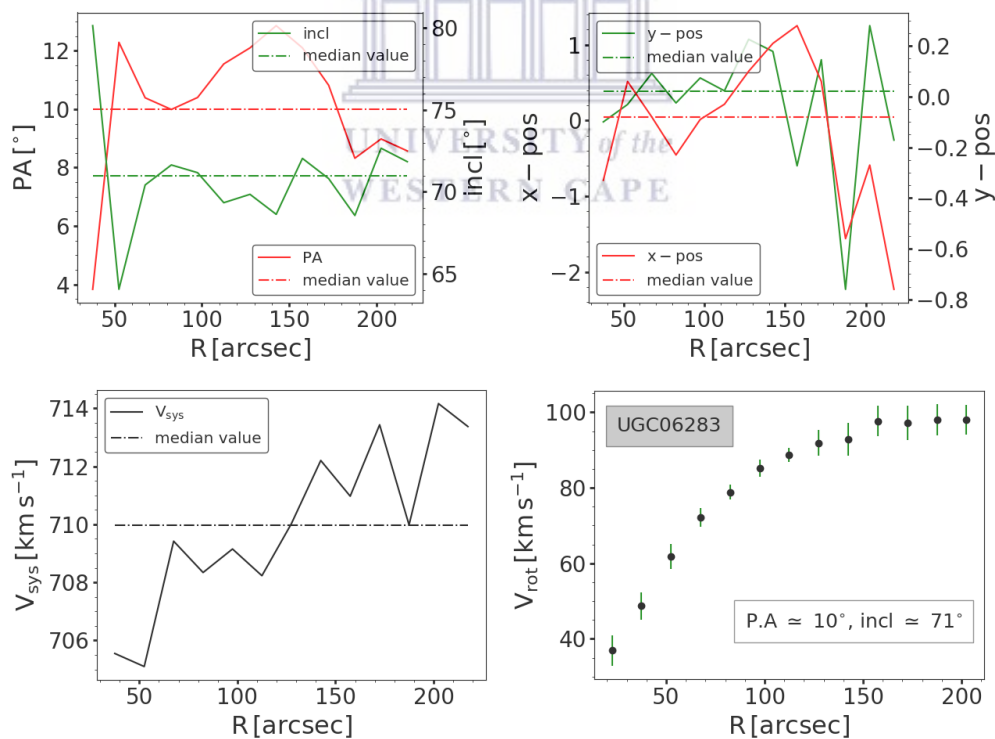


Figure 3.9: Full tilted ring model for UGC06283. See Figure 3.5 caption for full details.

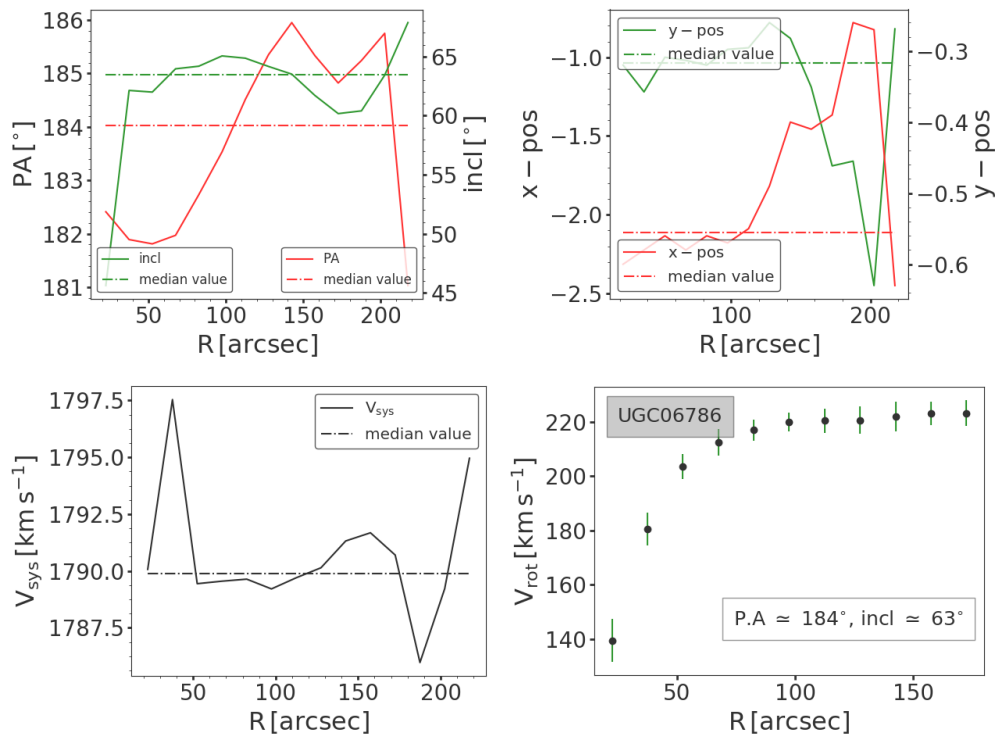


Figure 3.10: Full tilted ring model for UGC06786. See Figure 3.5 caption for full details.

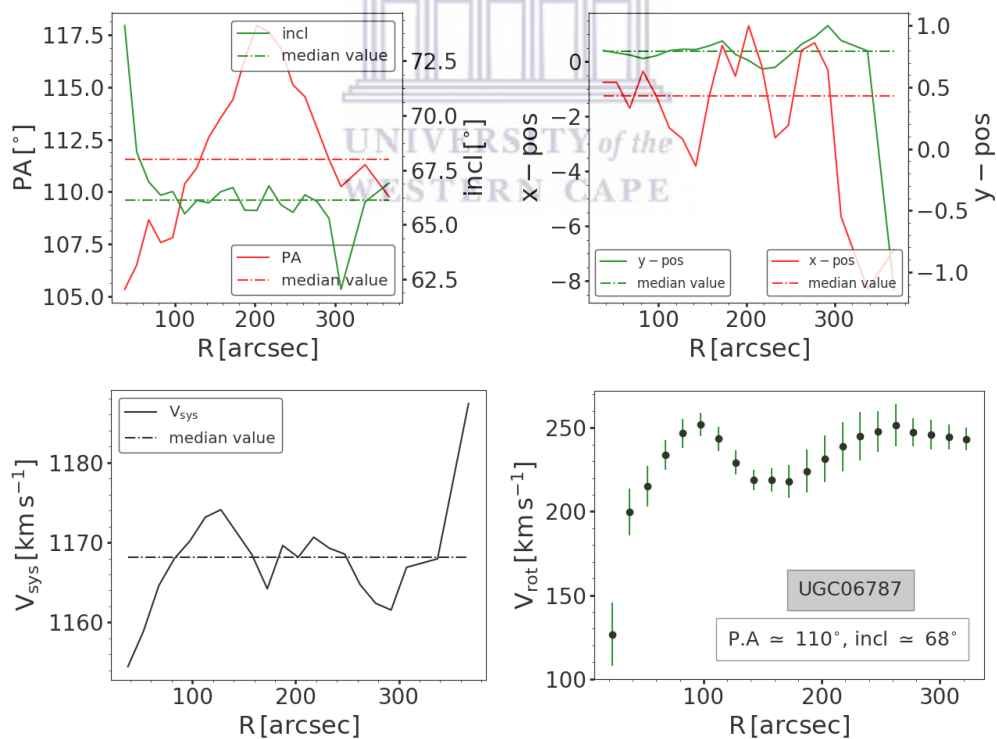


Figure 3.11: Full tilted ring model for UGC06787. See Figure 3.5 caption for full details.

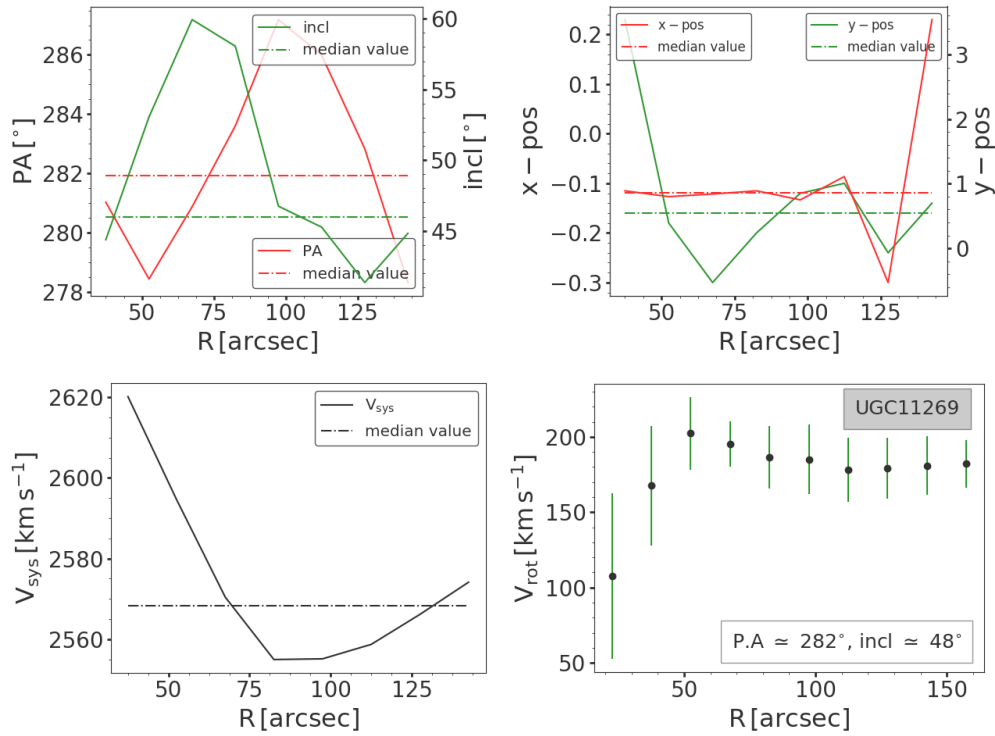


Figure 3.12: Full tilted ring model for UGC11269. See Figure 3.5 caption for full details.

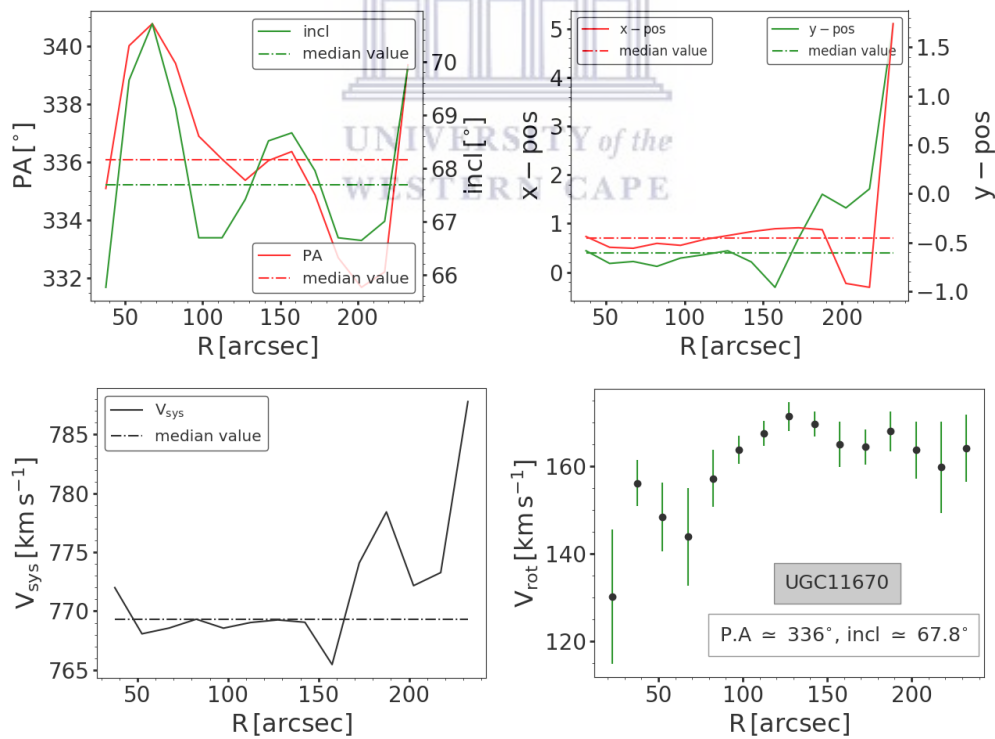


Figure 3.13: Full tilted ring model for UGC11670. See Figure 3.5 caption for full details.

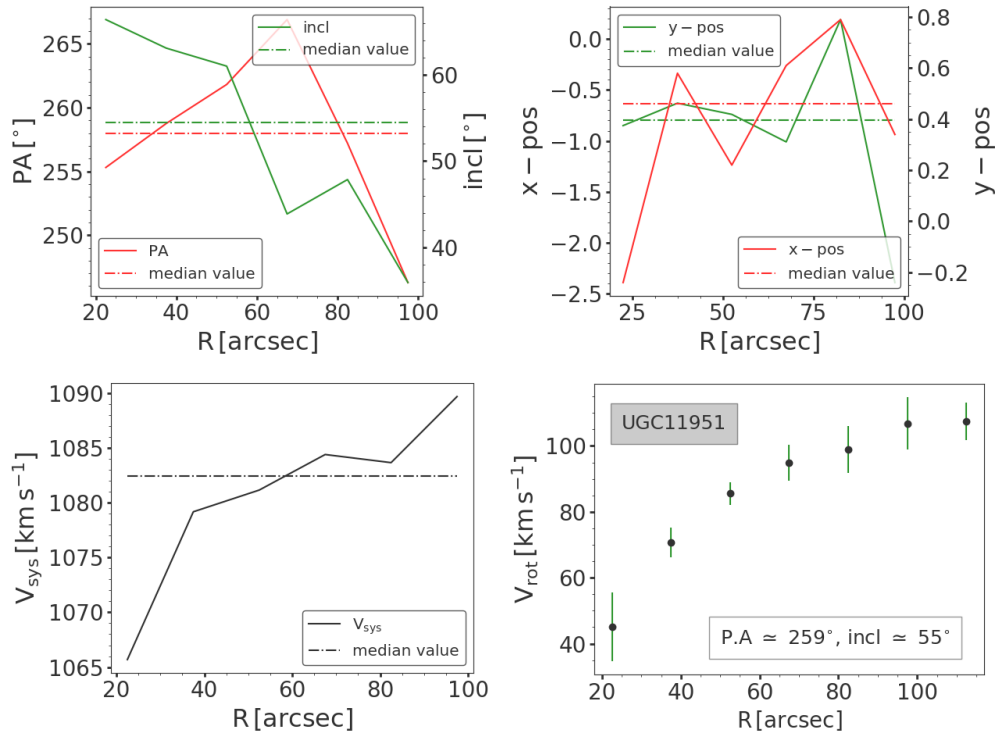


Figure 3.14: Full tilted ring model for UGC11951. See Figure 3.5 caption for full details.

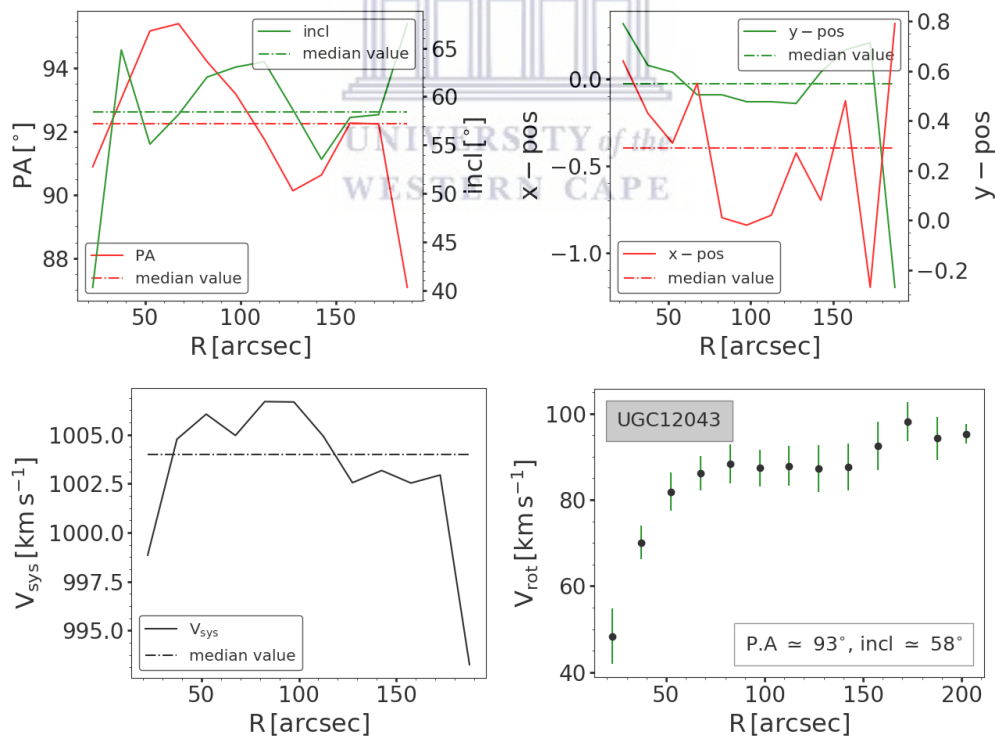


Figure 3.15: Full tilted ring model for UGC12043. See Figure 3.5 caption for full details.

Having constructed full tilted ring model for each galaxy, all rotation curves derived from this approach appeared to be rising quickly in their inner regions (e.g., UGC03546, UGC06786, UGC06787, UGC11269). Clearly, $H\alpha$ observations are required to resolve the velocity gradient in inner regions. In the outer regions some galaxies' rotation curves are declining (e.g., UGC02183, UGC03546, UGC11269). The reason to this decline is thought to occur in galaxies with a compact light distribution (Casertano and Van Gorkom, 1991). The uncertainty in the orientation parameters (position and inclination angle) arising from the tilted ring model in this work are well understood. In this work, a simple dynamic model for each galaxy was assumed where position and inclination angle were fixed at constant values. However, galaxies may not have constant inclination and position angle profiles. These potential errors are expected to have smaller contributions to rotation curves derived in this work. The sample in this work contained galaxies with rotation curves that look remarkably different from late-type galaxies, which usually rise slowly in the inner radii and then become flat at large radii. A dark matter halo is needed to constrain rotation velocities in the outer region while in the inner region luminous matter is required (Kent 1985; Côté et al. 2000).



3.6 Model-data comparisons

In order to assess the accuracy of the derived rotation curves, three different methods were used to compare the tilted ring models to the data.

3.6.1 Velocity field comparisons

The model velocity field for each galaxy in the sample was generated using tilted ring model presented in section 3.5. The HI velocity field models were generated using VELFI routine in GIPSY package and are shown in top right panels of Figures 3.16 - 3.26. In order to assess the accuracy of all model velocity fields, the bottom left panels in Figures 3.16 - 3.26 shows the residual maps. Bottom right panels of Figures 3.16 - 3.26 shows the distribution of the residual map values. For each galaxy, the residuals are typically Gaussian-distributed with a standard deviation less than $\sim 10 \text{ km s}^{-1}$. So the derived parameters fairly describe the kinematics of the observed galaxies precisely.

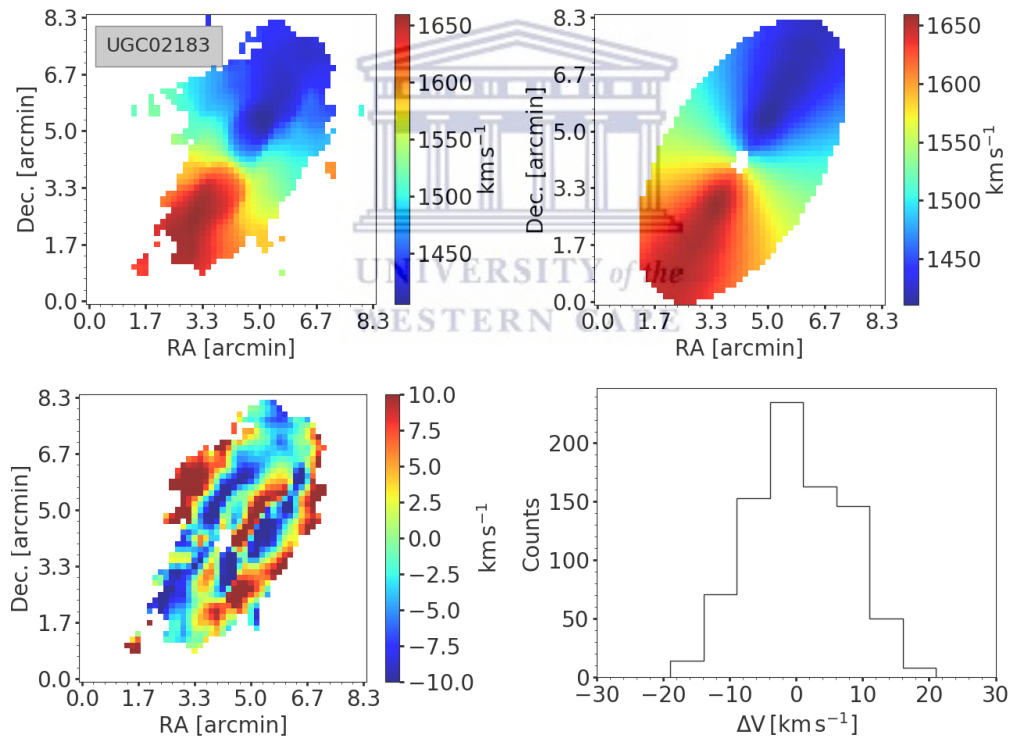


Figure 3.16: Comparison between observed and modelled HI velocity field for UGC02183. Top left panel: observed HI velocity field. Top right panel: model velocity field based on the tilted ring model generated for the galaxy. bottom left panel: residual map generated by subtracting the model HI velocity field from the observed HI velocity field. Bottom-right: distribution of residuals. Clearly, the distribution of residuals are nearly Gaussian and mostly contained within the order of few km s^{-1} .

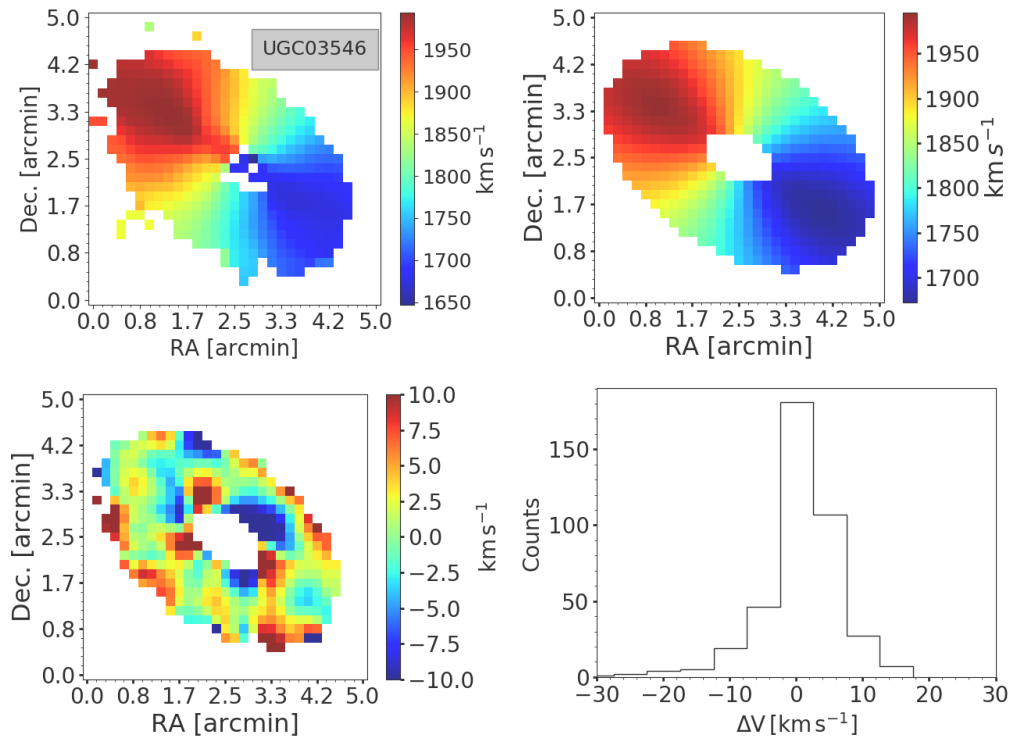


Figure 3.17: Comparison between observed and modelled HI velocity field for UGC03546. See Figure 3.16 caption for full details.

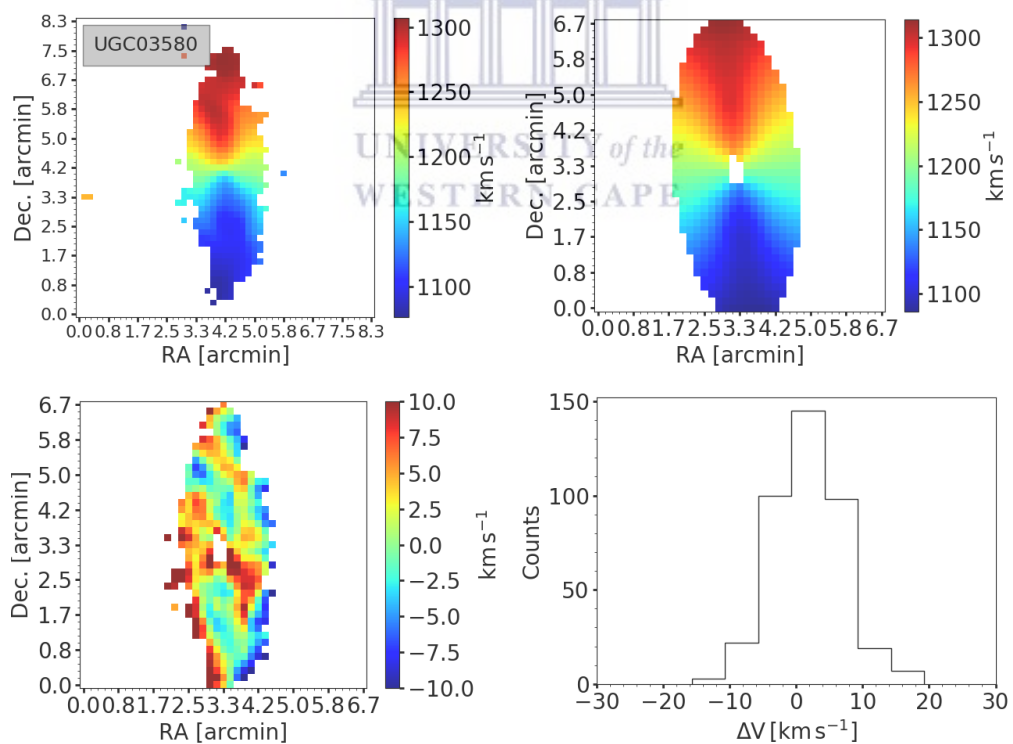


Figure 3.18: Comparison between observed and modelled HI velocity field for UGC03580. See Figure 3.16 caption for full details.

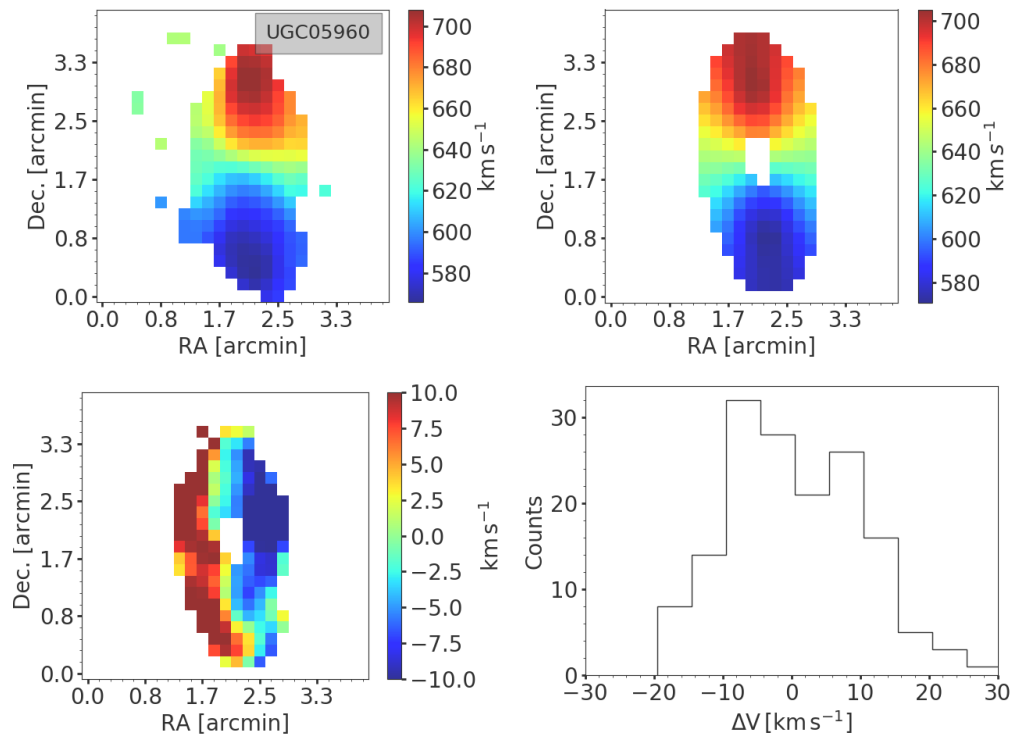


Figure 3.19: Comparison between observed and modelled HI velocity field for UGC05960. See Figure 3.16 caption for full details.

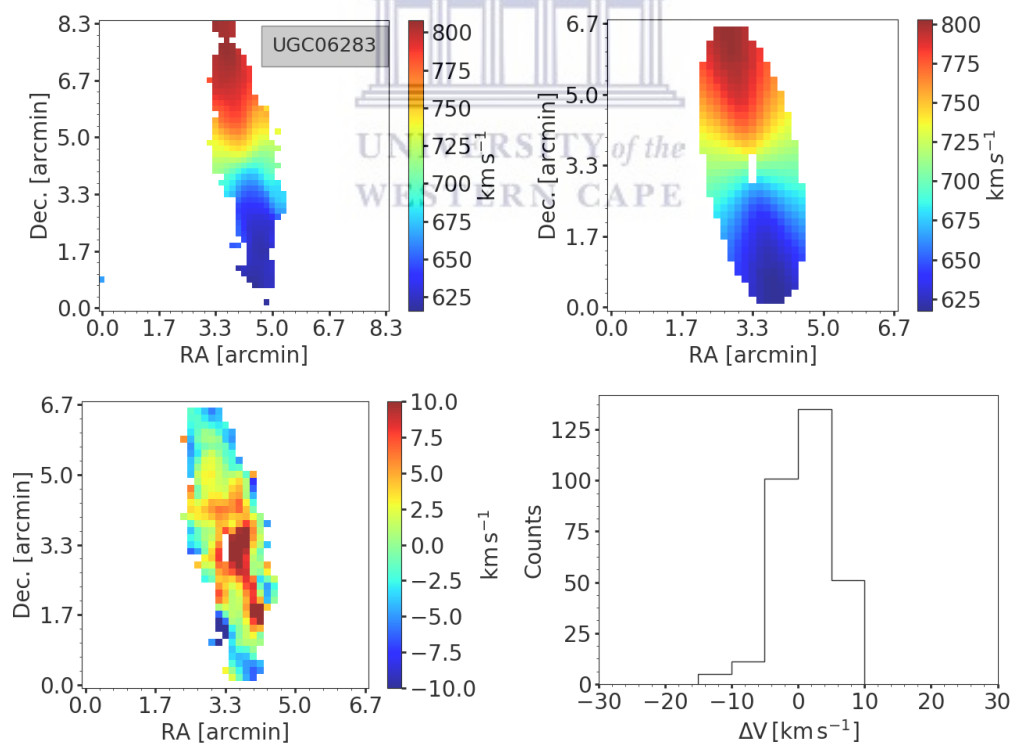


Figure 3.20: Comparison between observed and modelled HI velocity field for UGC06283. See Figure 3.16 caption for full details.

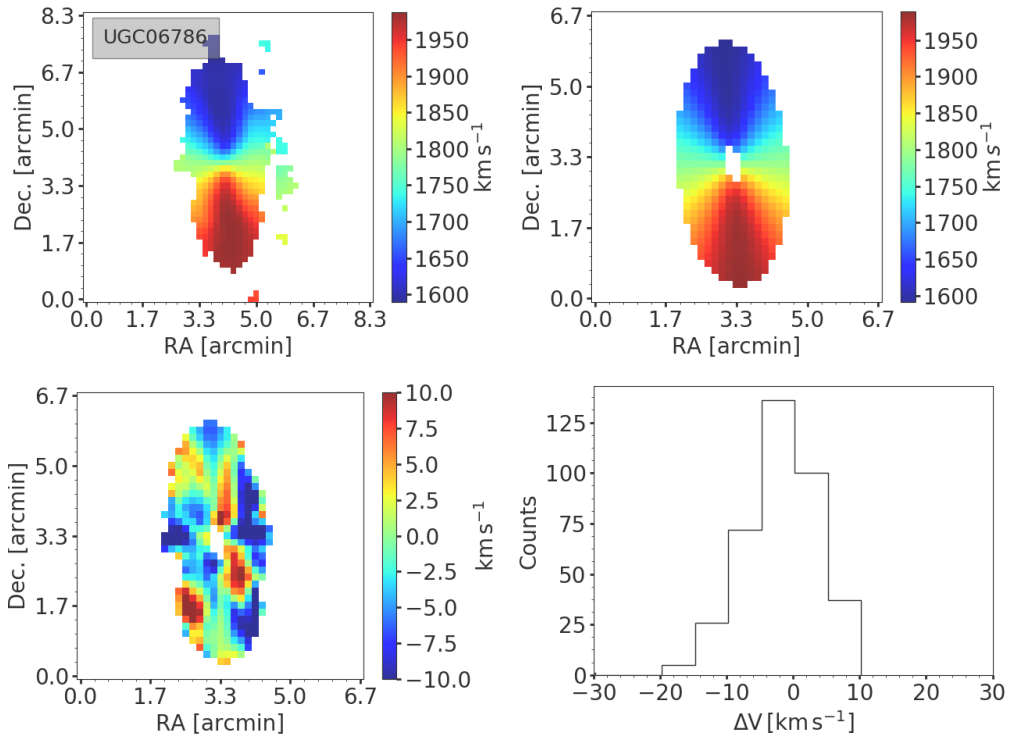


Figure 3.21: Comparison between observed and modelled HI velocity field for UGC06786. See Figure 3.16 caption for full details.

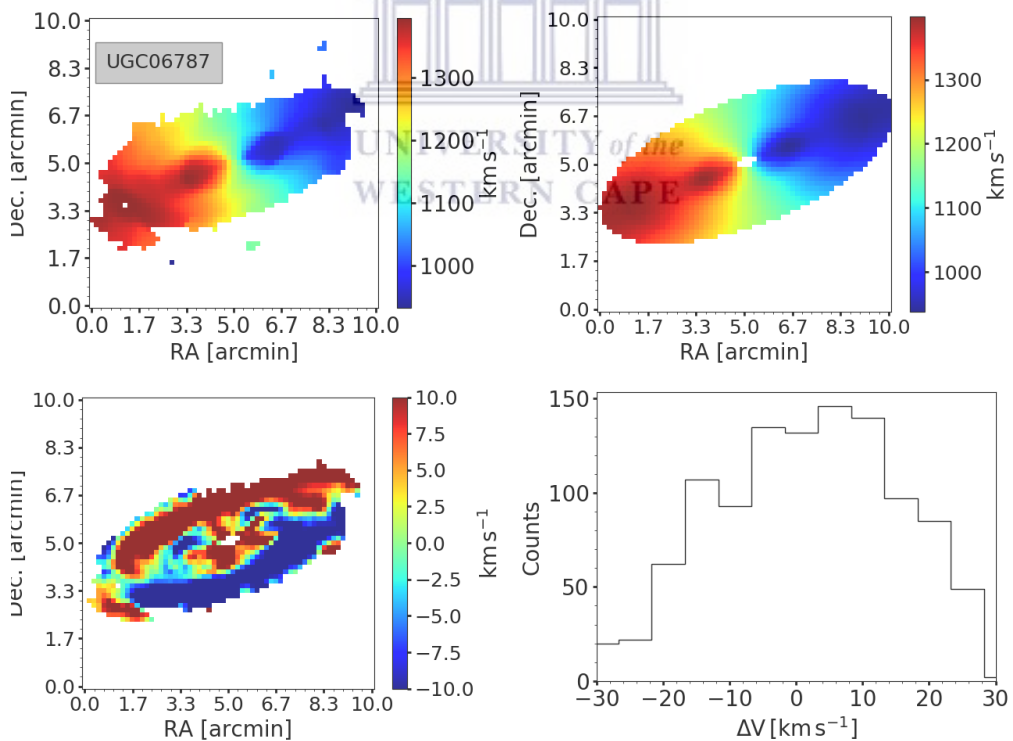


Figure 3.22: Comparison between observed and modelled HI velocity field for UGC06787. See Figure 3.16 for full details.

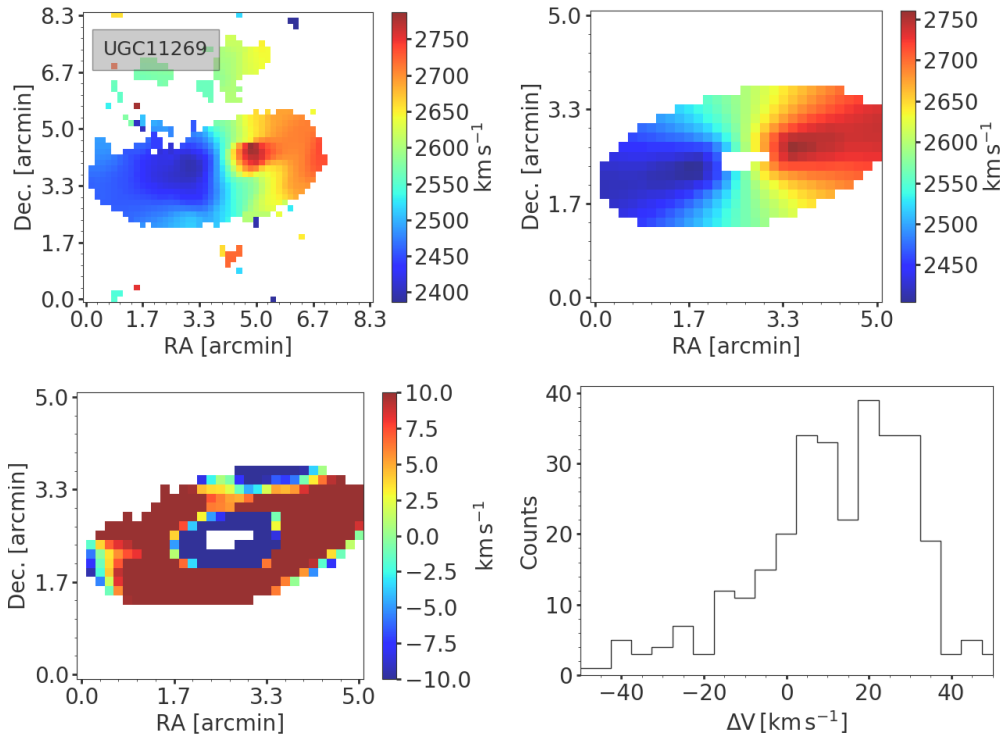


Figure 3.23: Comparison between observed and modelled HI velocity field for UGC11269. See Figure 3.16 caption for full details.

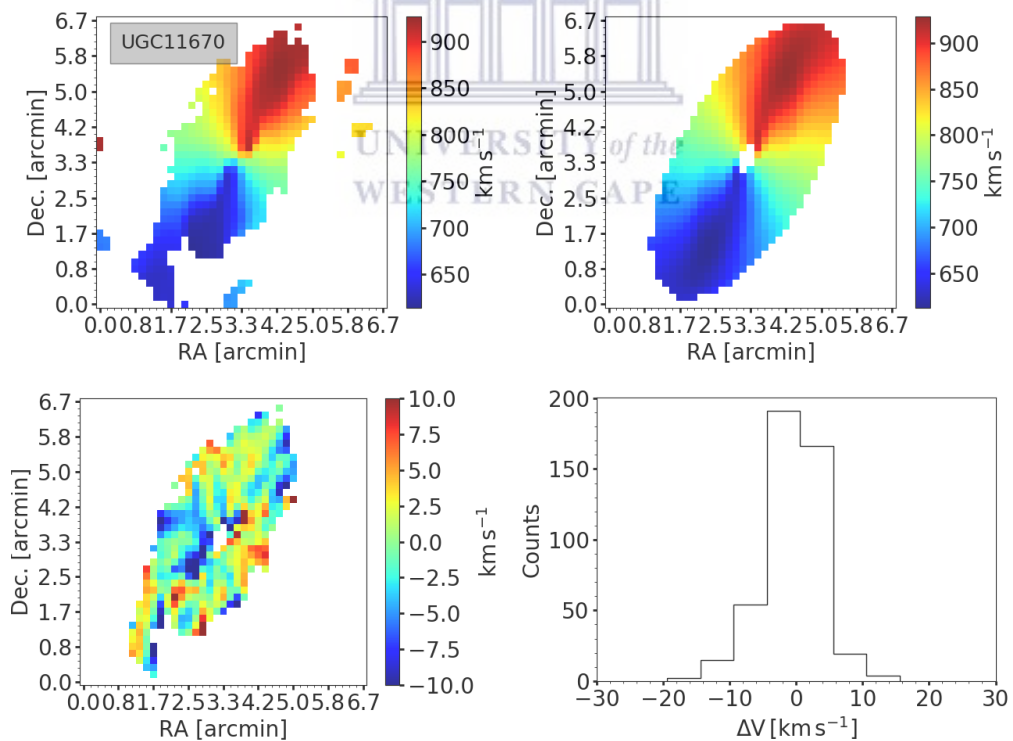


Figure 3.24: Comparison between observed and modelled HI velocity field for UGC11670. See Figure 3.16 caption for full details.

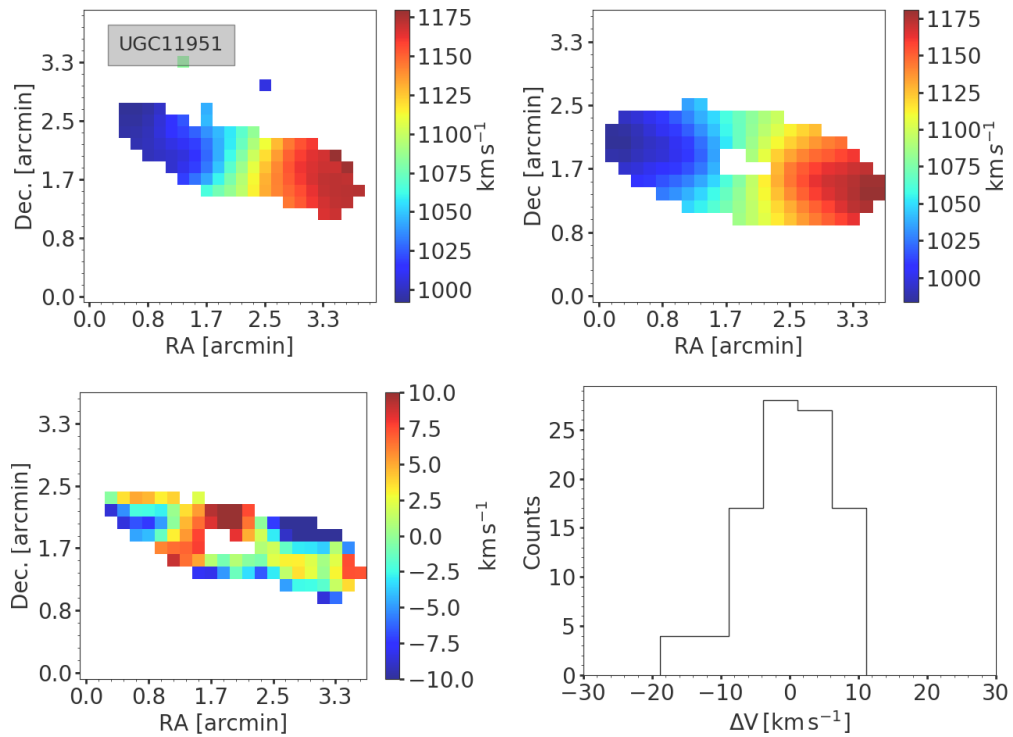


Figure 3.25: Comparison between observed and modelled HI velocity field for UGC11951. See Figure 3.16 caption for full details.

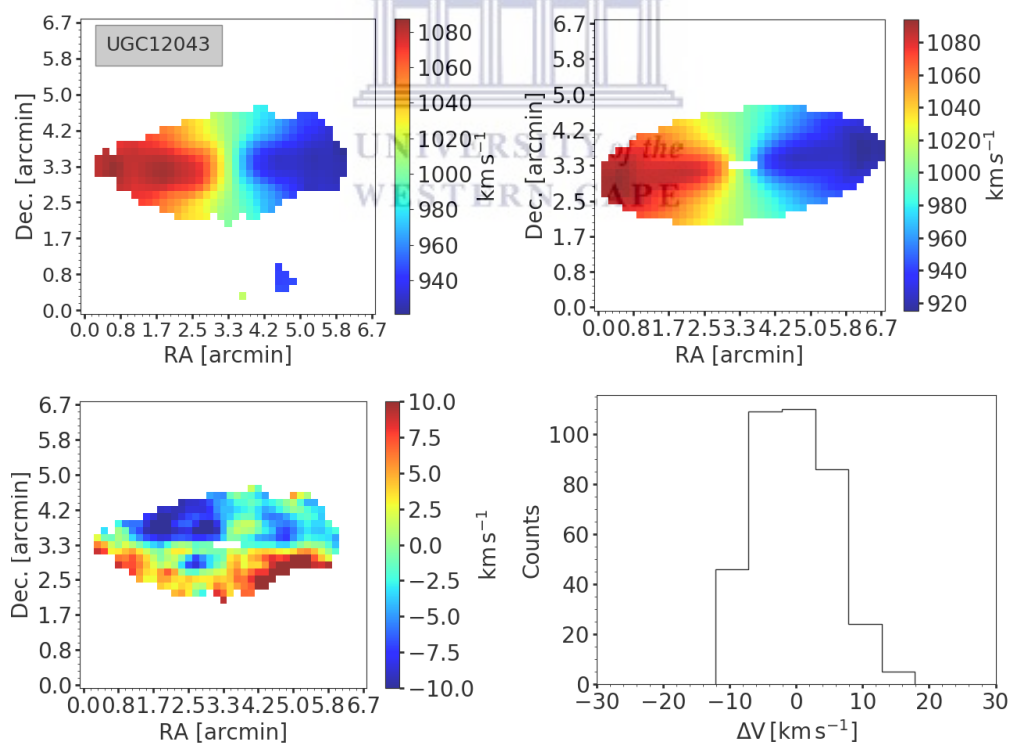
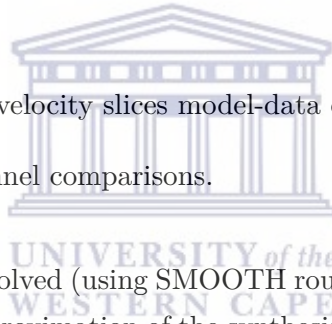


Figure 3.26: Comparison between observed and modelled HI velocity field for UGC12043. See Figure 3.16 caption for full details.

3.6.2 Three-dimensional comparisons

Similar to the ways in which the tilted ring models were used to generate model velocity fields, they were also used to generate full three-dimensional model cubes that were compared directly to the WHISP HI data cubes. In order to do this GALMOD routine in GIPSY was used (an axisymmetry is assumed). This routine constructs a model galaxy by randomly distributing small HI sub-clouds into the set of rings based on tilted ring model and HI mass surface density profile supplied by the user. The tilted ring model supplied by the user allows GALMOD to specify which channel every HI sub-cloud should be distributed to. The HI mass surface density profile of the galaxy (which the user specifies) allows GALMOD to specify which spatial pixel every single HI sub-cloud should be distributed to. The scale height perpendicular to the HI disk, column density, and velocity dispersion should also be provided by the user. For more detailed information, the reader is referred to <https://www.astro.rug.nl/~gipsy/tsk/galmod.dc1>. Surface density profiles used to model observations of the HI gas for each galaxy are shown in Figures B.1 - B.2 of Appendix B. For each galaxy the comparisons were performed in the following manner:

- Major axis position-velocity slices model-data comparisons;
- Full-channel-by-channel comparisons.



All model cubes were convolved (using SMOOTH routine in GIPSY; Van der Hulst et al. 1992) with a Gaussian approximation of the synthesised beam and directly compared on a channel-by-channel basis at seven different radial velocities: V_{sys} and $V_{\text{sys}} \pm \frac{i \cdot V_{\text{max}}}{3}$, where $i = 1, 2, 3$ and V_{max} is the maximum velocity from the measured HI rotation curve.

Shown in column 2 - 3 of Table 3.1 are the parameters used in GALMOD to model the three-dimensional distribution of HI in each galaxy. The scale height h of the HI layer for each galaxy was obtained using the method followed by Walter and Brinks (1999). In this case, the scale height is thought to be proportional to the velocity gas dispersion and inversely proportional to the square root of the density distribution of the HI disk. For the density distribution, $\rho(z, R) = 2\rho(0, R)\text{sech}(\frac{z}{z_0})$, a gas disk scale height can be expressed as:

$$z_0(R) = \frac{\sigma_{\text{gas}}}{\sqrt{2\pi G\rho(0, R)}}, \quad (3.10)$$

where σ_{gas} is gas velocity dispersion. In this work a constant value of 10 km s^{-1} for σ_{gas} was adopted. $\rho(0, R)$ gives total density in the plane of a galaxy's disk. At 1σ the scale height along the z -direction in Gaussian distributed can be approximated from the last measured radius as,

$$h = \frac{z_0}{\sqrt{2}}. \quad (3.11)$$

Shown in column 3 & 4 of Table 3.1 are scale heights obtained in units of arcsec and kpc, respectively.

Table 3.1: Parameters to model the HI observations for all galaxies. (1) UGC number, (2) Outer radius of HI disk in arcsec, (3) Scale height of the HI-layer in arcsec, (4) Scale height of the HI-layer in kpc.

UGC	R_{out} arcsec	h	
		arcsec	kpc
(1)	(2)	(3)	(4)
2183	285	12.20	1.27
3546	165	4.70	0.62
3580	225	9.80	0.91
5960	120	8.90	0.45
6283	210	12.0	0.70
6786	180	4.50	0.55
6787	330	7.50	0.69
11269	165	5.00	0.93
11670	240	8.20	0.50
11951	120	6.00	0.51
12043	210	12.3	0.92

Figure 3.27 shows three-dimensional comparisons for UGC02183. The three-dimensional comparisons for other galaxies are shown in Figures B.3 - B.12 of Appendix B.

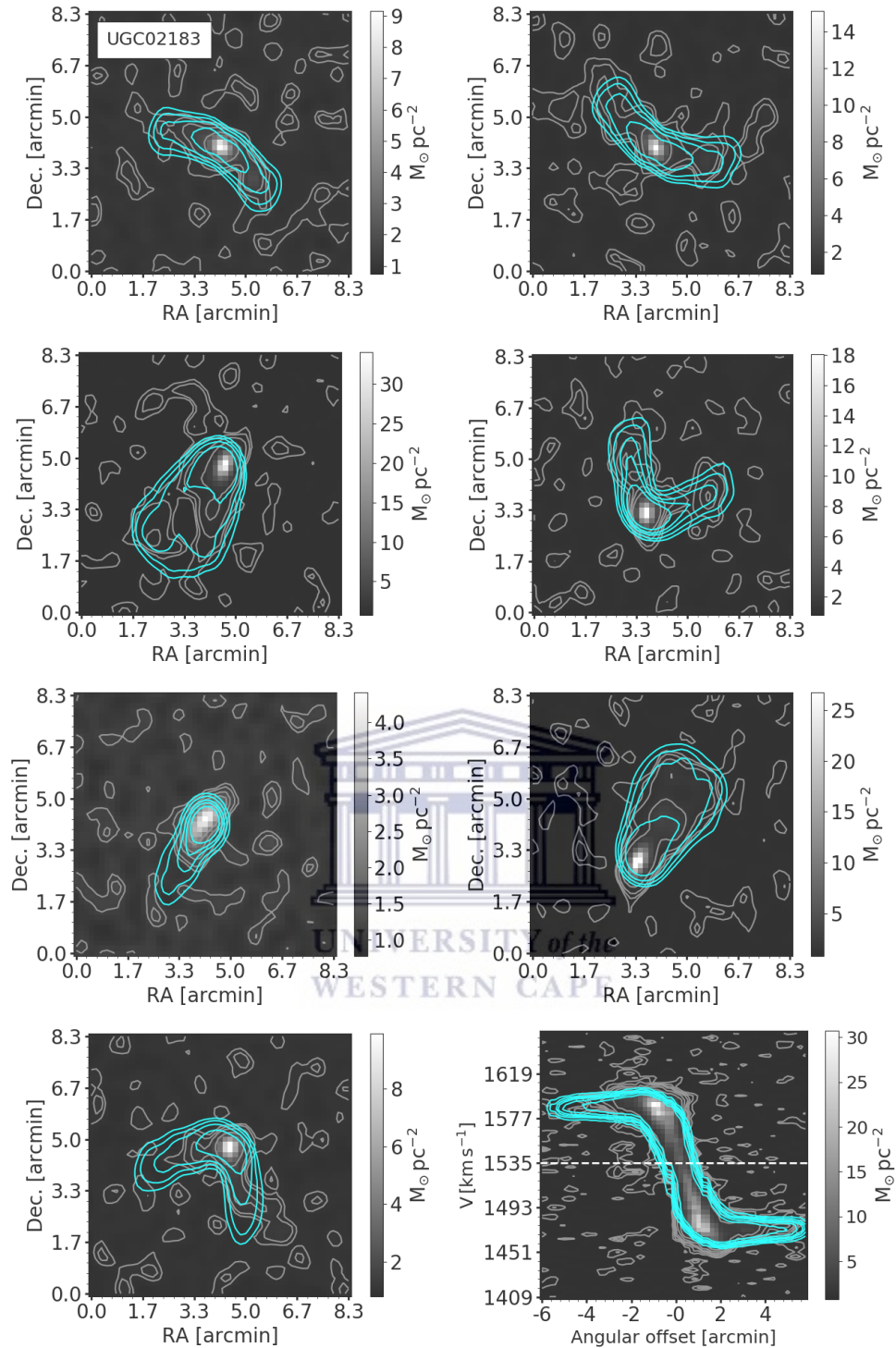


Figure 3.27: Channel maps comparison between WHISP data (grey scale and grey contours) and the model cubes generated using GALMOD (cyan contours). The contour levels are: 1σ , 2σ , 4σ , 6σ , 10σ , where σ is the noise level for each galaxy quantified in section 2.3 chapter 2. From top to bottom, left to right, the first seven panels shows the comparison at radial velocities of $V_{\text{sys}} \pm \frac{i \cdot V_{\text{max}}}{3}$, where $i = 0, 1, 2, 3$ and V_{max} is the maximum velocity from the measured rotation curve. The last panel shows the comparison for a position-velocity slice extracted along the major axis of the galaxy.

3.7 High-precision measurements of angular momentum

The detailed comparisons of our tilted ring models to the data (presented in section 3.6) confirm that the derived HI rotation curves are accurate representations of the galaxy kinematics. In this section, the rotation curves (presented in section 3.5) were used together with the measured baryonic mass surface density profiles (presented in section 3.3) to measure the angular momentum content of each galaxy. The total baryonic angular momentum J_b of each galaxy was measured using equation:

$$J_b = \int_0^{R_{\text{out}}} 2\pi R \cdot \Sigma_b(R) \cdot V_{\text{HI}}(R) \cdot R \cdot dR, \quad (3.12)$$

where $\Sigma_b(R)$ is azimuthally-averaged baryonic mass surface density distribution and V_{HI} is the HI rotation curve. Then the total baryonic angular momentum obtained by setting the upper and lower integration limits in Equation 3.12 to $15''$ and R_{out} , respectively. Where R_{out} is the outer-most radius. Then, the specific angular momentum (j_b) is defined as:

$$j_b = \frac{J_b}{M_b}. \quad (3.13)$$

All cumulative baryonic specific angular momentum profiles ($j_b(< R)$) measured in this work are shown as green curves in Figures 3.28 - 3.29.

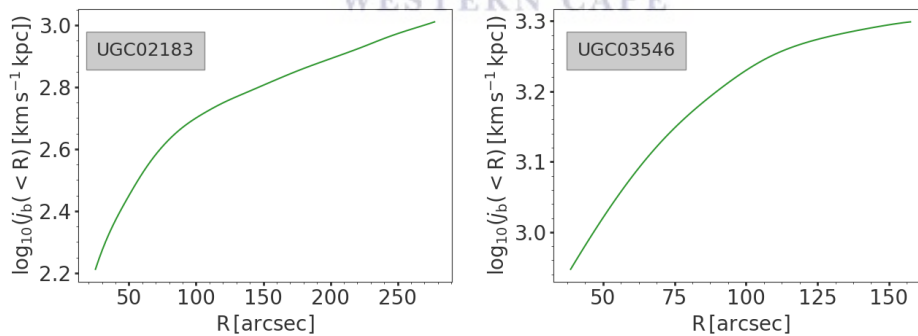


Figure 3.28: $j_b(< R)$ as a function of radius for each galaxy. All cumulative baryonic specific angular momentum profiles measured in this work are shown as green curves. $j_b(< R)$ rise slowly in the inner radius for each galaxy in this work. Clearly, all $j_b(< R)$ are converging but not fully converged at the outer-most radius.

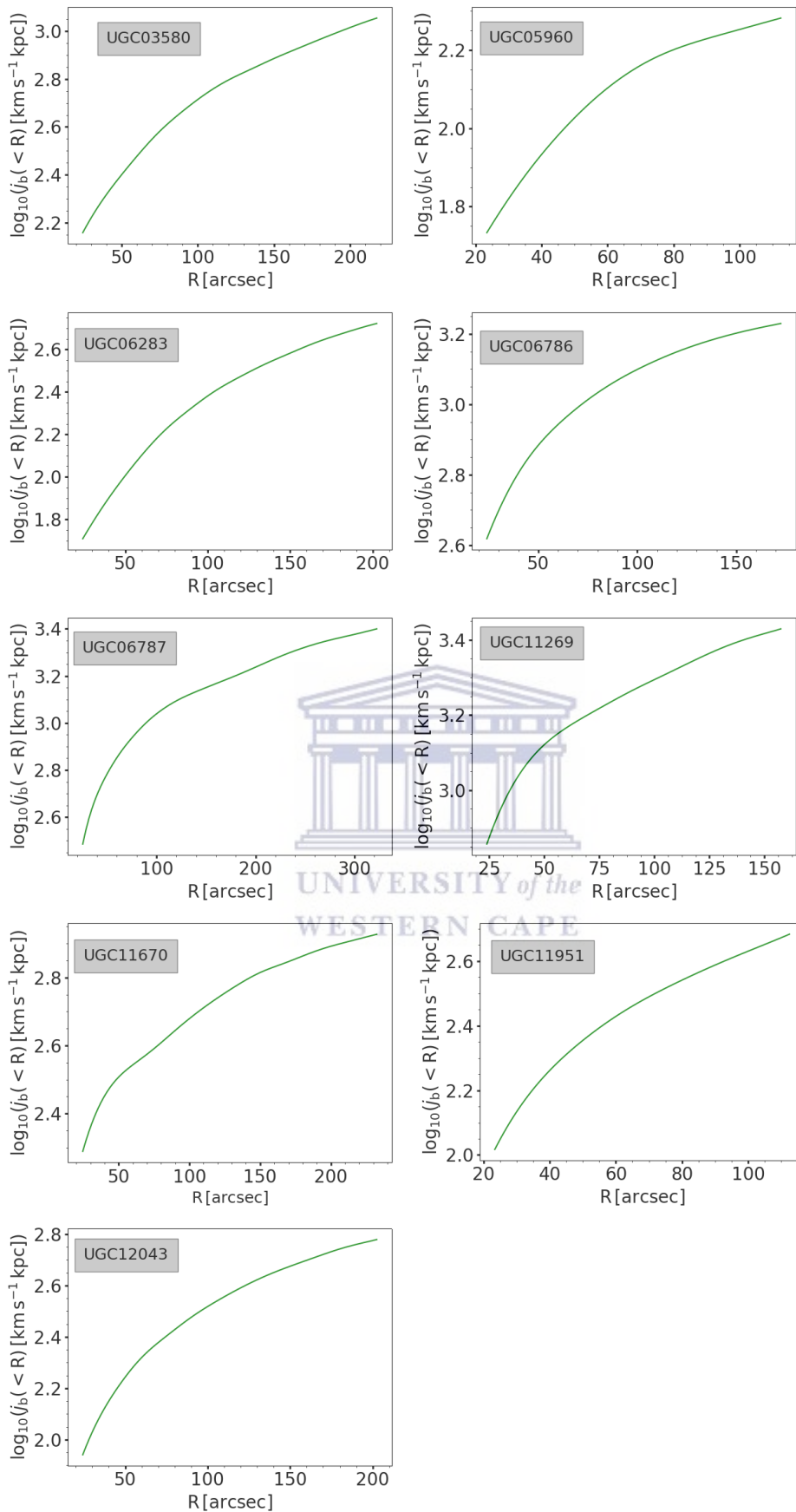


Figure 3.29: $j_b(<R)$ as a function of radius for each galaxy continued. See Figure 3.28 caption for full details.

Chapter 4

Results and discussion

Having constructed and presented the cumulative baryonic mass and specific angular momentum profiles in the previous chapter, this chapter focuses on using the profiles to study the distribution of our galaxy sample in the j_b versus M_b plane. The results are discussed in the context of other results in the literature.

In this work, the total angular momentum for each galaxy was measured at the outermost radius of the HI rotation curve (R_{out}). Shown in columns 2 - 6 of Table 4.1 is the actual measure of the total gas mass, total stellar mass, total baryonic mass, total baryonic angular momentum, and total baryonic specific angular momentum for each galaxy, respectively.

Table 4.1: High-precision measure of baryonic specific angular momentum in this work. (1) UGC number, (2) gas mass, (3) stellar mass, (4) baryonic mass, (5) Baryonic angular momentum, (6) baryonic specific angular momentum.

UGC	M_{gas} $10^9 M_{\odot}$	M_{\star} $10^9 M_{\odot}$	M_b $10^9 M_{\odot}$	$\log_{10}(J_b)$ $M_{\odot} \text{ km s}^{-1} \text{ kpc}$	$\log_{10}(j_b)$ $\text{km s}^{-1} \text{ kpc}$
(1)	(2)	(3)	(4)	(5)	(6)
02183	6.3	4.7	11.0	13.1	3.01
03546	4.6	18.4	23.0	13.7	3.30
03580	14.4	4.8	19.2	13.3	3.05
05960	1.9	0.5	24.1	11.7	2.28
06283	8.2	1.5	96.4	12.7	2.72
06786	10.0	26.4	36.3	13.8	3.23
06787	15.3	31.5	46.8	14.1	3.40
11269	25.5	27.1	52.7	14.2	3.43
11670	4.4	28.8	33.1	13.4	2.93
11951	6.7	3.6	10.3	12.7	2.68
12043	4.5	1.1	0.6	12.5	2.78

The specific angular momentum profiles shown in section 3.7 of chapter 3 quantify the angular momentum at different galactocentric radius. The integrals in section 3.7 rise gradually in the inner parts and do not converge at the outer-most radius. These lack of convergence may be due to the fact that the rotation curves used to generate j_b are not extrapolated out to a radius beyond R_{HI} (e.g., Elson 2017). However, extrapolating further could lead to adding uncertainty in the rotation curve. Obreschkow and Glazebrook (2014) claimed that HI mass surface density greater than $1 \text{ M}_{\odot} \text{ pc}^{-2}$ will decrease J_{HI} and j_{HI} by about 20% and 10%, respectively. While generating cumulative baryonic specific angular momentum profile for each galaxy, the rotation velocities of stars were assumed to be the same as that of the gas. Obreschkow and Glazebrook (2014) stated that the effect of uncertainties rise from this assumption contribute less than 10% to the stellar component of the specific angular momentum.

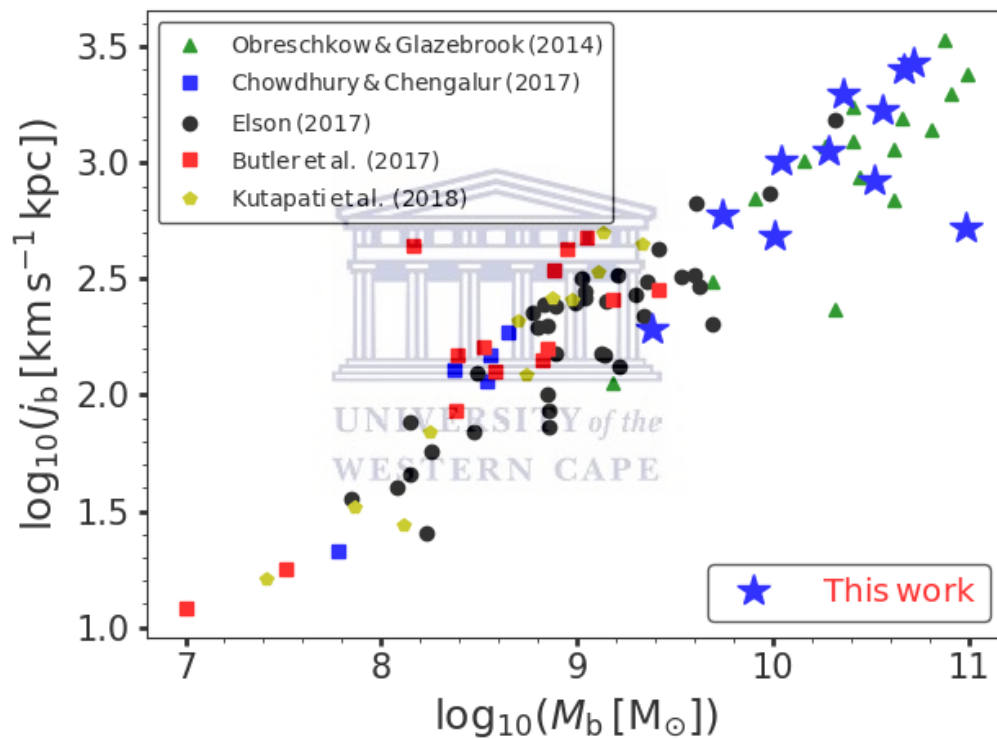


Figure 4.1: Specific baryonic angular momentum as a function of baryon mass for galaxies studied in this work (blue stars) and for various samples from the literature (indicated by the legend on the top left of the figure). The sample of galaxies in this study follows a trend followed by late-type galaxies and there is no significant offset between early-type galaxies and other late-type galaxies.

Figure 4.1 shows high-precision measurements of $j_b - M_b$ relation obtained in this work (indicated by blue stars) and also from other studies indicated according to the legend provided in top left corner in Figure 4.1. Green triangles represents the 16 spiral galaxies from THINGS studied by Obreschkow and Glazebrook (2014), (OG14). OG14 study was the first baryonic high-precision measurements to investigate the relation between

baryonic mass (M_b) and baryonic specific angular momentum (j_b) and bulge fraction (β) in a sample of late-type galaxies, and obtained strong correlations in these three parameters. Blue squares are gas-rich dwarf galaxies from [Chowdhury and Chengalur \(2017\)](#), (CC17). CC17 study focused on gas rich dwarfs observed as part of Giant Metrewave Radio Telescope (GMRT), and they claimed that over 3 orders of magnitude in baryonic mass dwarfs have higher specific angular momentum than the predicted relation of spirals. The results were interpreted in the sense that dwarfs form differently as compared to the spiral galaxies implying different evolution of angular momentum. Black circles are 37 WHISP late-type galaxies from [Elson \(2017\)](#), (E17). The sample comes from [Swaters et al. \(2009\)](#) containing those galaxies with inclination $\leq 75^\circ$. E17 study is consistent with the $j_b \propto M_b^{2/3}$ relation obtained and is in consistent theoretically with OG14 results. This sample spans a large range of mass, $10^8 \lesssim (M_b/M_\odot) \lesssim 10^{11}$. Red squares are 14 LITTLE THINGS dwarf galaxies from [Butler et al. \(2016\)](#), (B17). B17 found that their sample of low mass galaxies to deviates significantly from the expected spiral relation of $j_b \propto M_b^{2/3}$. The sample shows higher values of j_b than expected from the $j_b \propto M_b^{2/3}$ scaling relation of spiral galaxies. Their results were found to be consistent with the Λ CDM theory. Yellow polygons are 11 void dwarf galaxies from [Kurapati et al. \(2018\)](#). Their sample also shows higher values of j_b and are consistent with the dwarf relation obtained by [Butler et al. \(2016\)](#). Their results also show that the specific angular momentum increase at $\sim 10^{9.1} M_\odot$, which is a threshold below which galaxy disks are systematically thicker. They claimed that other physical processes, such as cold accretion, also play a role in the increase of specific angular momentum.

Blue stars in Figure 4.1 shows the determination of specific baryonic angular momentum and baryonic mass relation of early-type disk galaxies from the WHISP sample used in this work. A linear relation was fitted (in log-log space) to the data points from the WHISP sample on $j_b - M_b$ plane. The best-fit relation in this work was obtained by fitting first-order polynomial and found to be $j_b \propto M_b^\alpha$, with slope $\alpha = 0.46$ and y-axis intercept $\log_{10} q = -2.02$. Over a range $10^{9.2} \lesssim (M_b/M_\odot) \lesssim 11.0$ in baryonic mass, this work shows systematically higher values of j_b , similar to the results from the sample of dwarf irregular galaxies by [Butler et al. \(2016\)](#). A tight relation in specific baryonic angular momentum is observed with all galaxies in the sample lying in the same relation as early-type galaxies. However, an offset in high-precision measurements is not observed for early-type disk galaxies. The results in this work are consistent with spiral relation obtained by [Obreschkow and Glazebrook \(2014\)](#). The rest of the sections are dedicated to investigate and discuss various scenarios that could affect the distributions of the data points in the $j_b - M_b$ plane in this work.

4.1 Comparison between low- and high-precision measurements

Fall (1983), (F83) observed the clear separation between late- and early-type galaxies, based on low-precision measurements of the stellar angular momentum content. In order to test whether F83 results are dependent upon the low-precision nature of the measurements, this section aims to calculate low-precision angular momentum measurements for the galaxies used in this work, and then compare the measurements presented in Table 4.1. Obreschkow and Glazebrook (2014) shows that for an exponential disk $\Sigma(r) \propto \exp(-r/R)$ rotating at a constant circular velocity V , the angular momentum $j(r)$ is given by,

$$j(r) = \left[2 + \frac{(r/R)^2}{1 + r/R - \exp(r/R)} \right] R V. \quad (4.1)$$

Then in limit when $r \rightarrow \infty$, Equation 4.1 becomes,

$$j_b = 2\bar{R}_b V_{\text{flat}}. \quad (4.2)$$

Equation 4.2 shows specific angular momentum measure approximation used by F83, where \bar{R}_b is the exponential scale radius of the baryonic disk, V_{flat} is the constant circular velocity. The HI line widths, W_{50} , calculated in section 2.5 of chapter 2 and presented in column 7 of Table 2.3 were used to estimate V_{flat} using Equation,

$$W_{50} = 2V_{\text{flat}}\sin(i) \quad (4.3)$$

where i is an inclination angle of each galaxy listed in column 9 of Table 2.1. All velocities V_{flat} measured using Equation 4.3 in this work are listed in column 3 of Table 4.2.

In this work the exponential scale radius \bar{R}_b was estimated by fitting an exponential function to the baryonic mass surface density in the inner and outer radius for each galaxy. Shown as a blue curve in Figure 4.2 is an exponential function fitted to the azimuthally-averaged baryonic mass surface density. For this example, simple exponential is unable to fit the surface density densities of intermediate radii. However, most galaxies have their radial baryonic distribution reasonable well approximated by

an exponential function. All fitted exponential functions to the azimuthally-averaged baryonic mass surface density in this work are shown in Figures A.4 - A.7 of Appendix A. All the exponential scale radius for the baryonic disk \bar{R}_b obtained in this work are shown in column 2 of Table 4.2. Column 4 of Table 4.2 shows total baryonic specific angular momentum estimates measured using Equation 4.2.

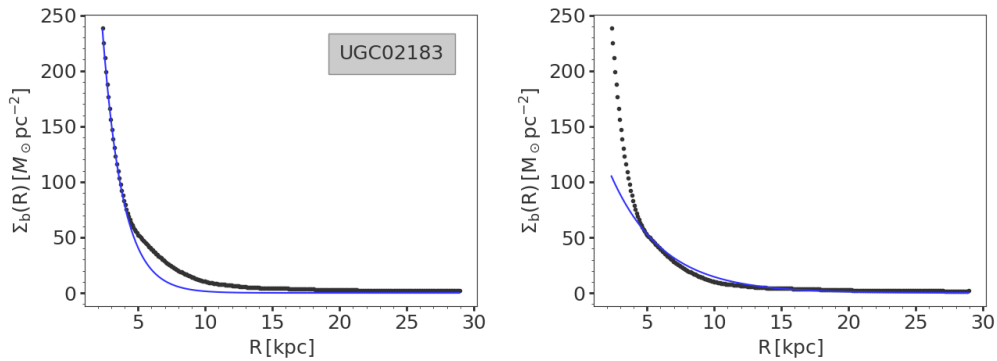


Figure 4.2: An example of baryonic mass surface density profile (black-filled circles) fitted with an exponential function (blue curve) in the inner (left panel) and outer radius (right panel) for UGC02183. Most galaxies have most of their HI mass surface density profiles well approximated by an exponential function.

Table 4.2: Low-precision measures of baryon specific angular momentum for this work. (1) UGC number, (2) estimate of exponential scale length obtained from fitted exponential function to the azimuthally-average baryonic mass surface density profile in the inner radius, (3) estimate of exponential scale length obtained from fitted exponential function to the azimuthally-average baryonic mass surface density profile in the outer-most radius, (4) estimate for constant circular velocity, (5) baryon specific angular momentum obtained using column 2, (6) baryon specific angular momentum obtained using column 3.

UGC	\bar{R}_b^{in} kpc	\bar{R}_b^{out} km s^{-1}	V_{flat} km s^{-1} kpc	$\log_{10}(\bar{j}_b^{\text{in}})$ km s^{-1} kpc	$\log_{10}(\bar{j}_b^{\text{out}})$
(1)	(2)	(3)	(4)	(5)	(6)
02183	1.50	3.87	150.0	2.65	3.06
03546	4.54	3.32	221.0	3.13	3.00
03580	2.01	8.60	117.0	2.67	3.30
05960	1.00	1.44	86.4	2.24	2.39
06283	1.39	5.32	102.0	2.45	3.03
06786	2.31	4.81	230.0	3.03	3.55
06787	1.58	5.56	269.0	2.93	3.30
11269	3.34	8.00	197.0	3.05	3.43
11670	1.10	3.60	171.0	2.57	3.09
11951	1.43	4.22	108.0	2.49	2.96
12043	1.26	4.77	95.6	2.38	2.99

Figure 4.3 shows comparisons between low- and high-precision measurements of specific baryonic angular momentum obtained in this work based on the inner disk scale lengths shown in column 2 of Table 4.2. These shows that high-precision values are always higher than low-precision values, but not with a factor 3 - 5 higher. It therefore cannot account for the lack of offset in the results obtained in this work. The red solid line in Figure 4.3 shows the best-fit to the data points obtained based on the inner disk scale lengths with the average vertical off-set ranging from 0.15 - 0.38 dex to the model indicated by a green solid line. All data points (black filled circles) in Figure 4.3 have a vertical off-set ranging from 0.04 - 0.47 dex to the green solid line.

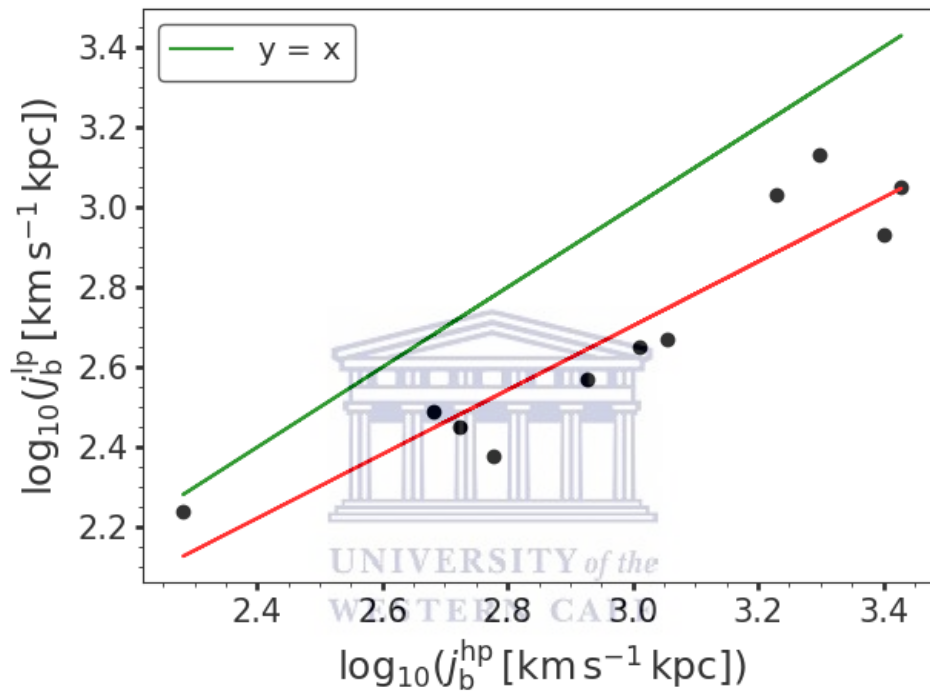


Figure 4.3: Low-precision j_b measurements as a function of high-precision measurements for the galaxies used in this work based on the inner disk scale lengths. The green line represents the line of equality, the red solid line is the best-fit 1st order polynomial through the data points. High-precision measurements are typically a factor of ~ 2 larger than low-precision measurements.

In Figure 4.4, comparisons between low- and high-precision measurements of specific baryonic angular momentum obtained in this work based on the outer disk scale lengths shown in column 3 of Table 4.2. In this case most high-precision values are higher than low-precision values, but not with a factor 3 - 5 higher. Also it therefore cannot account for the lack of offset in the results obtained in this work. The blue solid line in Figure 4.4 shows the best-fit to the data points obtained based on the outer disk scale lengths with the average vertical off-set ranging from 0.06 - 0.28 dex to the model indicated by a green solid line. All data points (black filled circles) in Figure 4.4 have a vertical off-set ranging from 0.0001 - 0.56 dex to the green solid line.

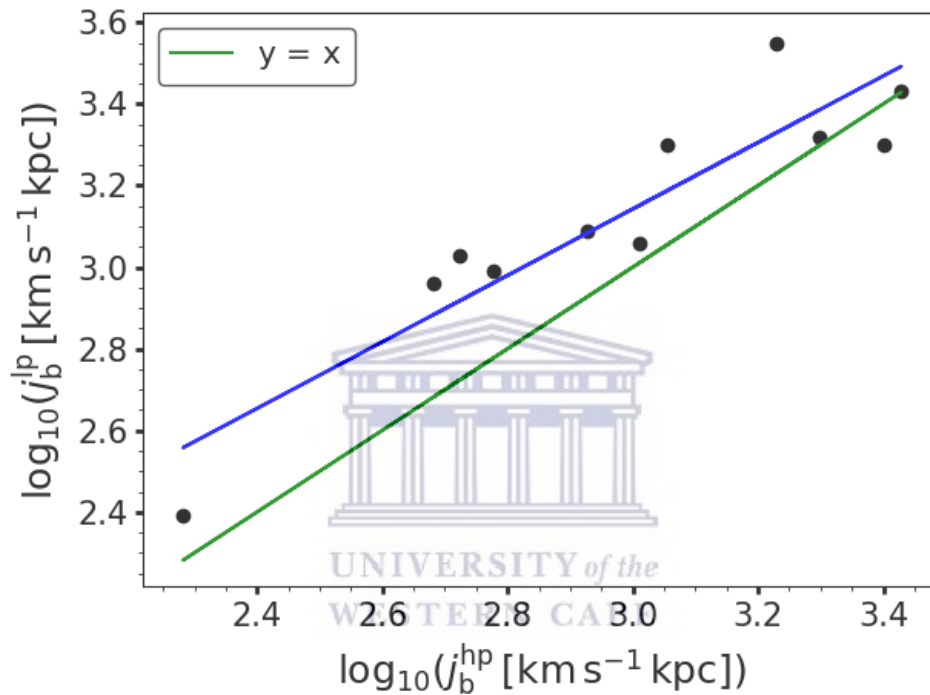


Figure 4.4: Low-precision j_b measurements as a function of high-precision measurements for the galaxies used in this work based on the outer disk scale lengths. The green line represents the line of equality, the blue solid line is the best-fit 1st order polynomial through the data points. Most high-precision measurements in this case are typically a factor of ~ 2 lower than low-precision measurements.

4.2 Inner HI rotation curves inaccuracies

Due to the relatively low resolution of the WHISP imaging, the rotation curves generated in this work may not accurately represent the true circular velocity of material at inner radii. Noordermeer et al. (2005) claimed that early-type galaxies used in this work are characterised by a large velocity gradient in their inner radii.

The optical rotation curves presented by Noordermeer et al. (2007) could unfortunately not be obtained to incorporate into the analysis of this work. Therefore, in this section, a simplistic model will be made to estimate the effects of beam smearing (e.g., Verheijen 1997) on j_b measurements.

Assume an exponential thin disk such that the azimuthally-averaged baryonic mass distribution is given by,

$$\Sigma_b(R) = A \cdot e^{(-r/B)} \quad (4.4)$$

where A and B are constants representing the central mass surface density and the disk scale length. The total baryonic mass is given by,

$$M_b(< R) = \int_0^R \Sigma_b(R) \cdot 2\pi R \cdot dR. \quad (4.5)$$

Then combining Equation 4.4 and 4.5 and evaluate the integral gives,

$$M_b(< R) = 2\pi \cdot A \cdot B[B - (B + R)e^{-R/B}] \quad (4.6)$$

From Newton's law, this mass distribution correspond to the rotation curve of the form,

$$V(R) = \sqrt{\frac{M(< R) \cdot G}{R}}, \quad (4.7)$$

where $M(< R)$ is the total mass contained within radius R and G is the gravitational constant. Then combining Equation 4.6 and 4.7, gives the rotation curve of an exponential thin disk:

$$V1(R) = \sqrt{\frac{2\pi \cdot A \cdot B \cdot G[B - (B + R)e^{-R/B}]}{R}} \quad (4.8)$$

If we assume a rotation curve of the form given by equation 4.8, the velocities of all radii smaller than a distance C can be decreased by including a factor $(1 - e^{-R/C})$:

$$V2(R) = V1(R)(1 - e^{-R/C}), \quad (4.9)$$

where C is a constant. For a typical galaxy, assuming a set of values $A = 600 M_{\odot} \text{pc}^2$, $B = 3 \text{kpc}$ and a radius of 30kpc . Doing so emulates the effects of beam smearing on the rotation curve.

Left panels in Figure 4.5 - 4.2 shows two rotation curves $V1(R)$ and $V2(R)$ indicated as a black and green curve, respectively. $V2(R)$ is a slightly modified version of $V1(R)$ and it is generated from equation 4.8, when $C = B, \frac{B}{2}, \frac{B}{3}$ for top left, middle left, bottom left panel. Right panels in Figure 4.5 - 4.2 shows the total angular momentum profiles at three different values of C , respectively. It is clear that inner rotation curve inaccuracies does affect angular momentum measurements by small amount since most angular momentum is contained at outer radii. The percentage differences in angular momentum measured in the outer radius (black and green curves) are 0.035%, 0.004%, 0.001% for $C = B, \frac{B}{2}, \frac{B}{3}$, respectively.

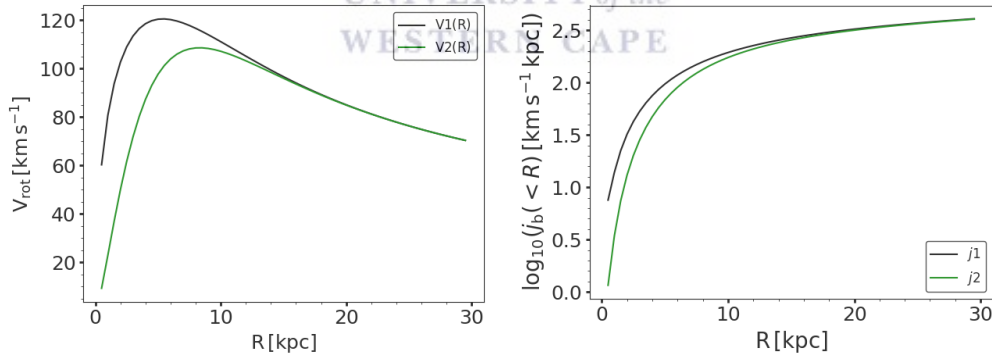


Figure 4.5: Shown as black and green curves in left panels are rotation curves that rises quickly and slowly in inner radii, respectively. Shown in right panels as black and green curves are high-precision measurements of total baryonic angular momentum obtained using rotation curves that rise quickly and slowly, respectively. It is clear that the difference in baryonic angular momentum obtained from rotation curves that rises quickly and slowly in the inner radii is negligible.

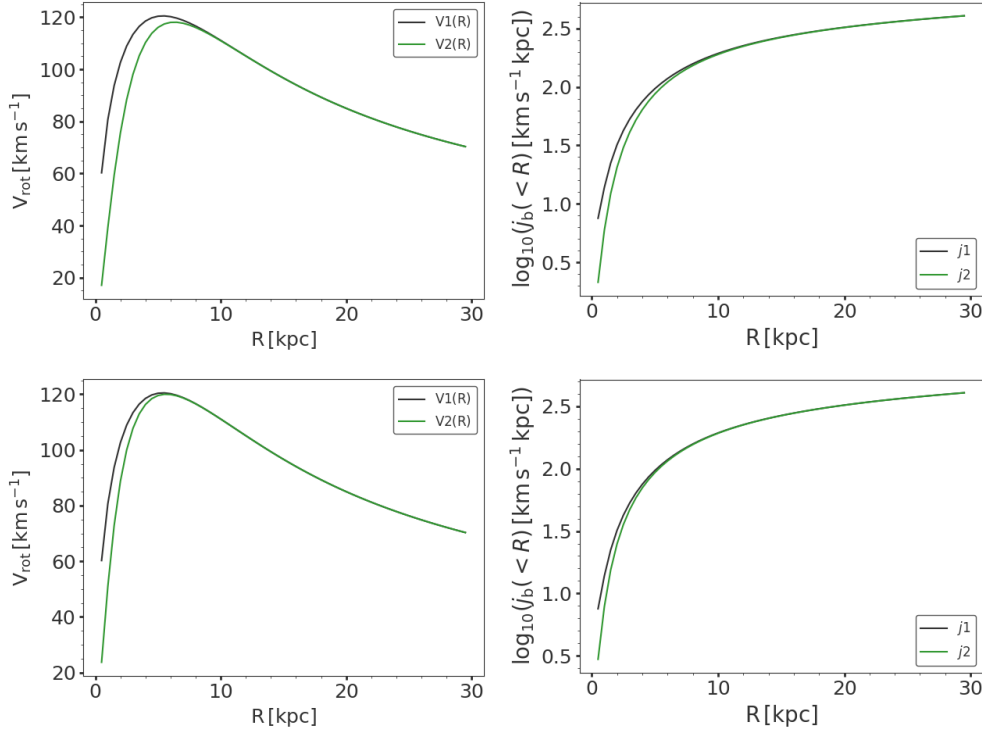


Figure 4.6: Quantifying the effects of inner HI rotation curve inaccuracies continued. See Figure 4.5 caption for full details.

4.3 Investigating uncertainties on baryonic specific angular momentum from the stellar contribution

This section will investigate the effect of uncertainties from the stellar contribution into the total angular momentum of each galaxy. Recall, an assumed mass-to-light ratio of $0.47 M_{\odot}/L_{\odot}$ (e.g., [McGaugh and Schombert \(2014\)](#)) was adopted in measuring the stellar contribution to the total angular momentum for each galaxy in this work. Listed in columns 2-4 of Table 4.3 are j_b estimates based on 0.235 and $0.705 \frac{M_{\odot}}{L_{\odot}}$ to those based on $0.47 \frac{M_{\odot}}{L_{\odot}}$. Both scenarios doesn't lead to a factor 3 -5 in the j_b estimates. So mass-to-light ratio value of $0.47 \frac{M_{\odot}}{L_{\odot}}$ cannot be the reason for the lack of the offset in the results obtained in this work.

Table 4.3: Investigating the effect of uncertainties from the stellar contribution into the total angular momentum of each galaxy. (1) UGC number, (2) estimate of stellar contribution to j_b when mass-to-light ratio is $0.235 \frac{M_\odot}{L_\odot}$, (3) $0.470 \frac{M_\odot}{L_\odot}$, (4) $0.705 \frac{M_\odot}{L_\odot}$.

UGC	$j_b^{0.235}$ km s ⁻¹ kpc	$j_b^{0.47}$ km s ⁻¹ kpc	$j_b^{0.705}$ km s ⁻¹ kpc
(1)	(2)	(3)	(4)
02183	3.04	3.01	2.98
03546	3.32	3.30	3.29
03580	3.08	3.05	3.03
05960	2.29	2.28	2.27
06283	2.74	2.72	2.71
06786	3.23	3.23	3.21
06787	3.46	3.40	3.37
11269	3.47	3.43	3.40
11670	2.95	2.93	2.92
11951	2.71	2.68	2.66
12043	2.79	2.78	2.76

Shown in Figure 4.7 is the comparison of specific barionic angular momentum measurements obtained in this work when mass-to-light ratio is $0.235 M_\odot/L_\odot$ (red stars) and $0.47 M_\odot/L_\odot$ (blue stars) and $0.705 M_\odot/L_\odot$ (black stars).

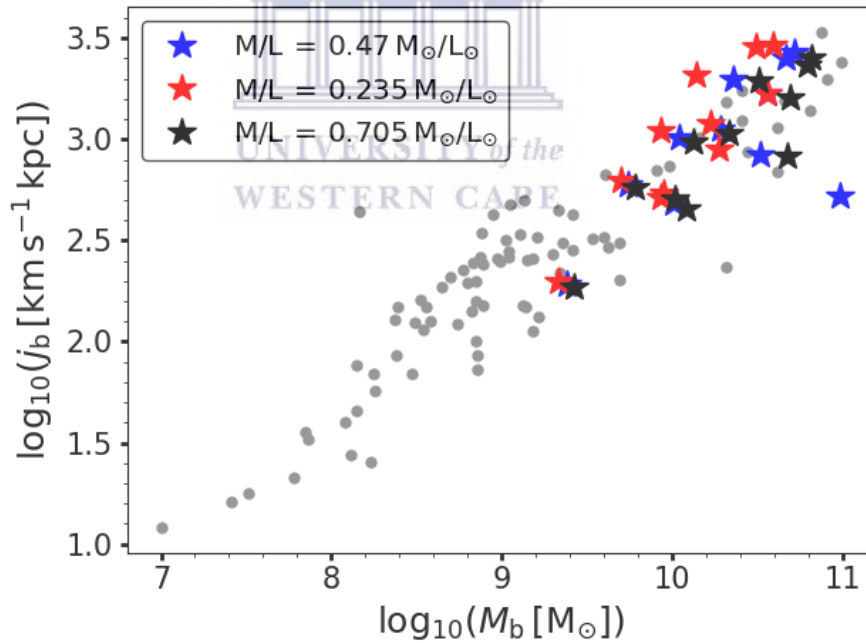


Figure 4.7: Specific baryonic angular momentum as a function of baryonic mass. Blue, red, black stars show specific baryonic angular momentum measurements when assumed mass-to-light ratio equal to 0.47, 0.235, 0.705 M_\odot/L_\odot , respectively. grey filled-circles are results from the literature shown according to the top left legend in Figure 4.1. The distribution of data points doesn't change much in the $j_b - M_b$ plane. The legend in the top left corner shows various values of mass-to-light ratio.

Figure 4.8 shows gas fraction as a function of stellar mass for all galaxies in this work. Half of galaxies in the sample are gas dominated. The specific baryonic angular momentum measurements in this work are less sensitive to the constant assumed of stellar mass-to-light ratio variable adopted for all galaxies, as clearly depicted by Figure 4.8.

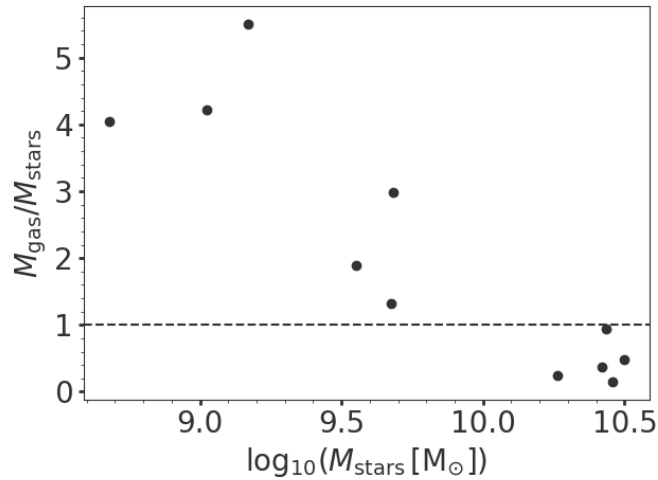


Figure 4.8: Gas fraction as a function of stellar mass for all galaxies in this work. Total gas fraction in this study is $M_{\text{HI+He}} = 1.324 \times M_{\text{HI}}$. 6 galaxies in the sample ($10^{8.5} < M_{\star}/M_{\odot} < 10^{9.7}$) in this study are gas dominated and 5 galaxies ($10^{10.2} < M_{\star}/M_{\odot} < 10^{10.6}$) are gas deficiency.

4.4 Difference between this work and Fall (1983)

The results in this work (blue stars shown in Figure 4.1) shows that high-precision study of baryonic angular momentum content of early-type disk galaxies lie systematically in the same relation followed by late-type galaxies on the $j_b - M_b$ plane. Fall (1983), (F83) was a low-precision study of the stellar angular momentum component of early- and late-type galaxies. An offset observed by F83 may not exist for baryonic high-precision measurements. It is not surprising that the intermediate morphological type of galaxies in this work lie in different relation in the $j_{\star} - M_{\star}$ plane as obtained by F83. F83 study was based on a large sample containing lots of spiral and elliptical galaxies, so in this work the offset between two types of galaxies was not expected in the $j_b - M_b$ plane. The method used in this work and F83 is totally different in several ways:

- Only stellar components were considered to probe the total angular momentum content of galaxies in F83. In this work baryons (gas + stars) were considered to probe the angular momentum content of galaxies.
- Low-precision measurements of angular momentum content of early-type galaxies in F83 were studied. High-precision measurements of angular momentum content of early-type disk (intermediate morphological type) galaxies were studied in this work.

The sample in this work unfortunately does not overlap with F83 sample. It would be simplistic to find one galaxy from F83 sample to incorporate into the analysis of this work.



Chapter 5

Summary and conclusion

In conclusion, this work uses a sample of 11 nearby early-type disk galaxies to investigate the relation between specific baryonic angular momentum as a function of baryonic mass (Fall relation) spanning a range, $9.4 \lesssim \log_{10}(M_b/M_\odot) \lesssim 11.0$. The measurements were based on neutral hydrogen (HI) kinematics data from the WHISP survey at 30 arcsec resolution and $3.4\ \mu\text{m}$ WISE data. To accurately model well-resolved HI kinematics of each galaxy used in this work, intermediately inclined ($40^\circ < i < 75^\circ$) with an HI diameter greater than 6 beams (180 arcsec) were recovered from a large sample of early-type disk galaxies studied by [Noordermeer et al. \(2005\)](#). In order to investigate $j_b - M_b$ relation, all HI data products (total HI intensity maps, HI velocity fields, HI velocity dispersion maps) and HI rotation curves required for this study were re-derived in this work. These data products were re-derived by parameterising the WHISP HI data cubes by fitting a single Gaussian to every line profile with peak amplitude greater than 3σ . HI rotation curves were re-derived by fitting tilted ring models to the HI velocity fields using a routine called ROTCUR ([Van der Hulst et al. \(1992\)](#)). To assess the accuracy of our derived HI rotation curves, dynamical models were generated to compare the tilted-ring models to the data. HI total intensity maps were used to derive radial HI mass surface density profiles by azimuthally-averaged flux density in concentric rings. These HI mass surface density profiles (the presence of helium gas and other metals were also accounted) were combined with stellar mass surface density to give the baryonic mass surface density profiles. These baryonic mass surface density profiles were used together with the measured HI rotation curves to derive the specific angular momentum of galaxies. The angular momentum for each galaxy was measured at the outer-most radius. Then the results in this work shows that early-type disk galaxies lie in the same relation followed by various samples of late-type galaxies in the $j_b - M_b$ plane.

A linear relation was fitted (in log-log space) to the WHISP data sample in this work and the best-fit relation was found to be, $j_b \propto M_b^\alpha$, with slope $\alpha = 0.46$ and y-intercept $\log_{10} q = -2.02$. The baryonic relation in this work has a shallower slope than other relations. In this work no evidence found for an offset in baryonic angular momentum content of early-type galaxies as claimed by Fall (1983). Various scenarios that could affect the distributions of points in the $j_b - M_b$ plane were investigated in the context of other results in the literature, such as:

- Comparison between low- and high-precision measurements. In this case high-precision measurements are typically ~ 2 larger than low-precision measurements based on inner disk scale lengths presented in section 4.1 of Chapter 4. Likewise; most high-precision measurements are typically a factor of ~ 2 lower than low-precision measurements based on outer disk scale lengths presented in section 4.1 of Chapter 4. The difference between the two measurements cannot account for the lack of an offset in this work.
- Inner HI rotation curves inaccuracies. Due to the relatively low resolution of the WHISP imaging, a simplistic models were made to estimate the effects of beam smearing on j_b measurements. It was found that the effect of beam smearing cannot account the j_b measurements, hence cannot account for the lack of offset in this work.
- Uncertainty from stellar contribution to the angular momentum. More galaxies in the sample are gas-dominated and less sensitive to stellar mass-to-light ratio ($\frac{M}{L}$) as shown by Elson (2017). However a constant value of $\frac{M}{L}$ variable was kept fixed at $0.47 \frac{M_\odot}{L_\odot}$ in estimating the stellar mass of each galaxy. Two cases were investigated when $\frac{M}{L}$ variable was set constant at $0.235 \frac{M_\odot}{L_\odot}$ and $0.705 \frac{M_\odot}{L_\odot}$. The contribution of the uncertainty from the stellar component to the total angular momentum of each galaxy could not account for the lack of an offset in j_b measurements in this work.

5.1 Future prospects

HI distribution and dynamics studied in this thesis are limited to a resolution of 30 arcsec from the WHISP survey. The low-resolution from the WHISP observations used in this work; clearly does not resolve the inner HI distribution of galaxies in the sample as indicated in section 2.4 of chapter 2. However, the results presented here are important in understanding and unveiling dynamical processes that drive the properties of galaxies.

Having new surveys such as the MeerKAT HI Observations of Nearby Galactic Objects (MHONGOOSE; De Blok et al. 2017), MeerKAT International GHz Tiered Extragalactic Exploration (MIGHTEE; Taylor and Jarvis (2017)) and MeerKAT Fornax (see, Serra et al. 2017) will provide resolved HI detection. Over a broad range of galaxy in the nearby universe with HI masses from $\sim 10^6$ to $\sim 10^{11} M_{\odot}$ and morphologies, MHONGOOSE will probe extremely deep observations in a sample of 30 galaxies down to HI column density below $\sim 10^{18} \text{ cm}^{-2}$ at resolution of 30 arcsec (see, De Blok et al. 2017). This sensitivity will also be achieved by MIGHTEE survey in a large sample consisting of ~ 270 sources; especially for systems with HI masses lower than $\sim 10^8 M_{\odot}$ and ~ 15 sources below $10^7 M_{\odot}$ (see, Taylor and Jarvis 2017). MeerKAT Fornax survey will study HI morphology of resolved galaxies down to a column density of $\sim 10^{18} \text{ cm}^{-2}$ at a resolution of $\sim 10 \text{ kpc}$ in most massive cluster within 20 Mpc in the southern hemisphere. This survey is anticipated to give insight to the physical process that drive the evolution of galaxy in very dense region of the cosmic web and galaxy cluster; including gas accretion, gas stripping etc Serra et al. (2017). Observations from these surveys will extend the analysis of this work by accurately constraining inner and outer HI rotation curves of galaxies.



Appendix A

In order to assess the overall accuracy of the fitted Gaussians the reduced chi-squared statistic has been used to quantify the goodness of the Gaussian fit. The left panels in Figures A.1 - A.3 shows the distribution of the reduced chi-squared values. The center panels shows the spatial distribution of the reduced chi-squared values; and right panels shows HI total intensity maps.

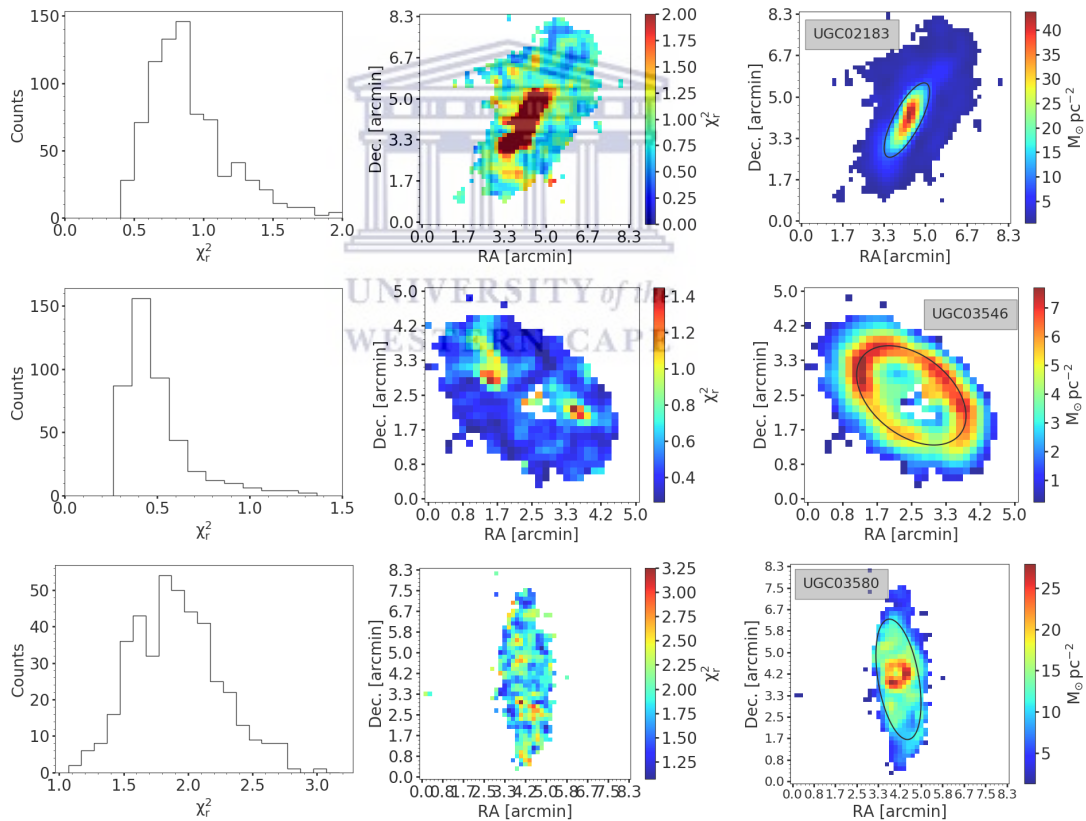


Figure A.1: Illustrations of the overall accuracy of the fitted Gaussians in HI data cubes. Left panel shows the distribution of spatial χ_r^2 , middle panel shows χ_r^2 map, right panel shows HI total intensity map.

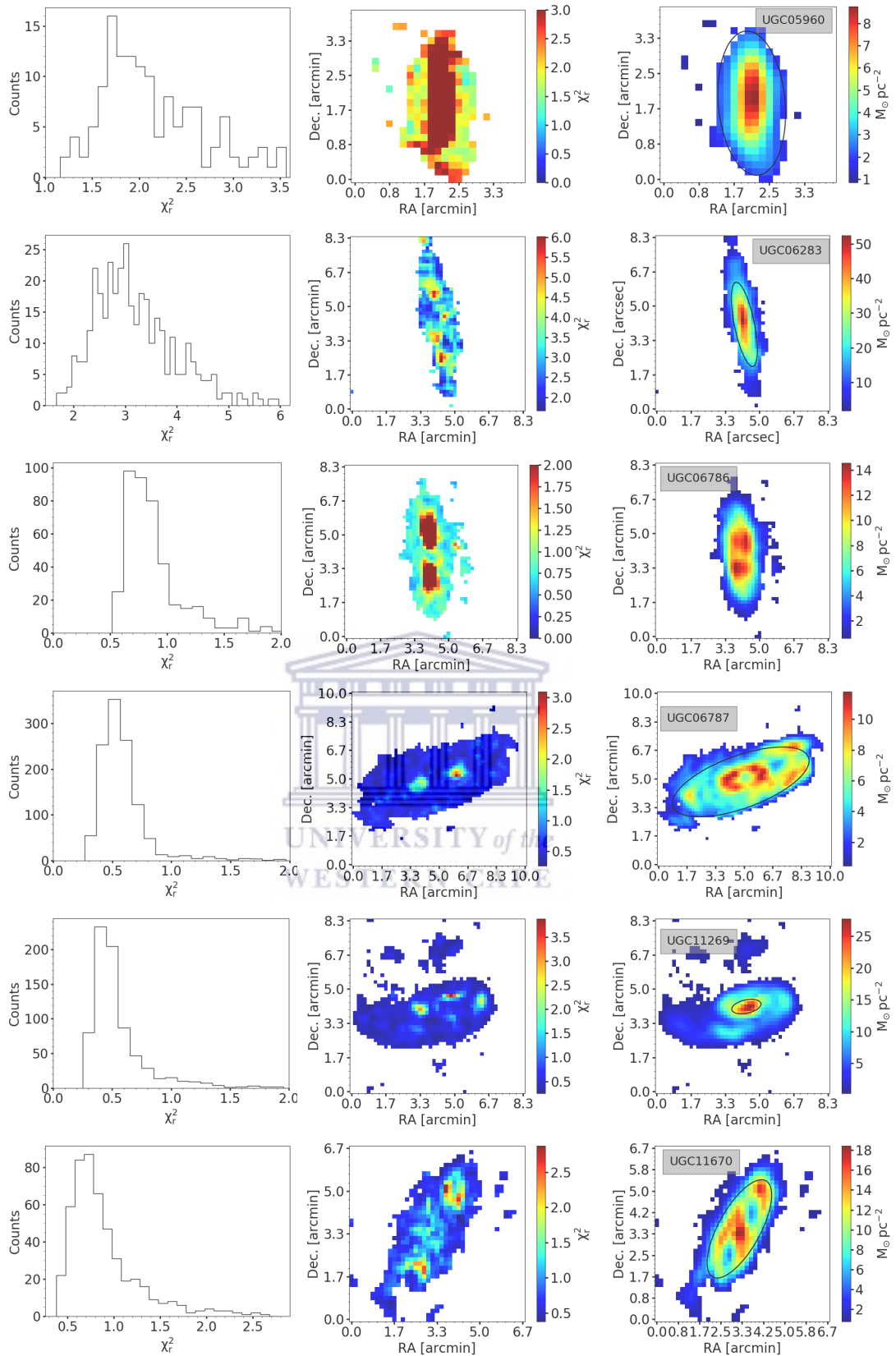


Figure A.2: Overall accuracy of the fitted Gaussians continued. See Figure A.1 caption for full details.

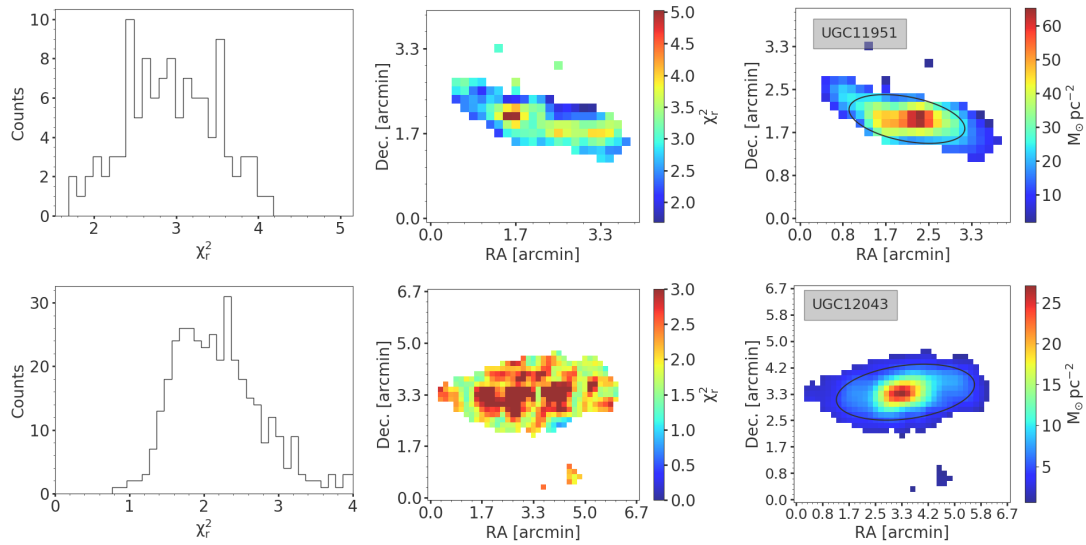


Figure A.3: Overall accuracy of the fitted Gaussians continued. See Figure A.1 caption for full details.

A.1 Baryonic mass surface density fitted with an exponential function

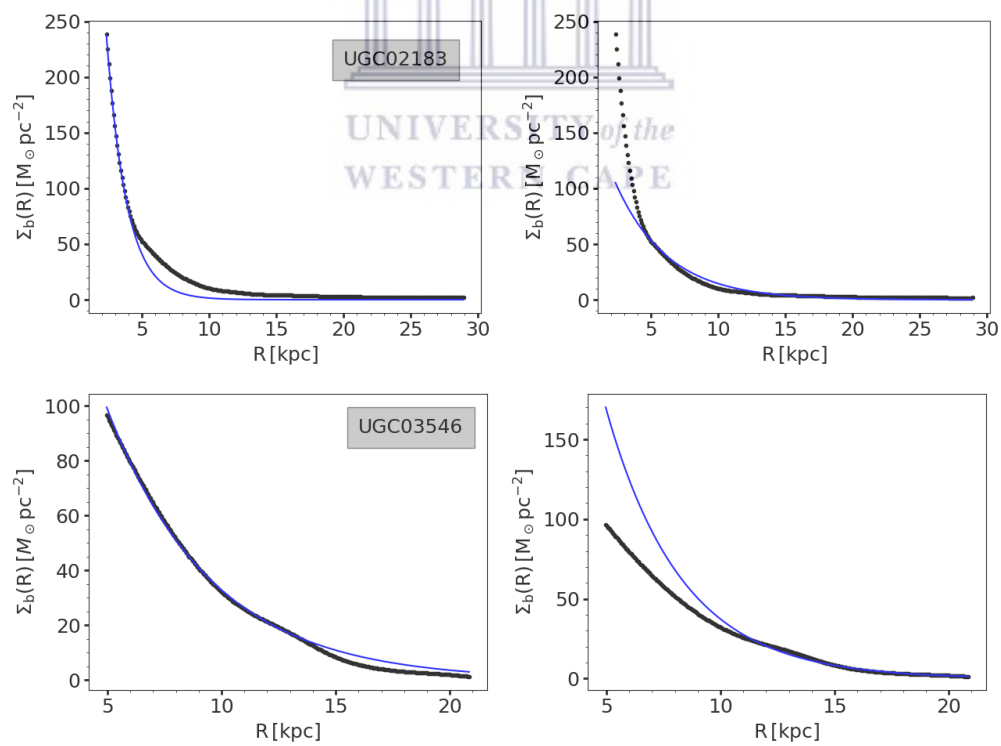


Figure A.4: Baryonic mass surface density profile (black-filled circles) fitted with an exponential function (blue curve) in the inner (left panel) and outer radius (right panel). Most galaxies have most of their HI mass surface density profiles well approximated by an exponential function.

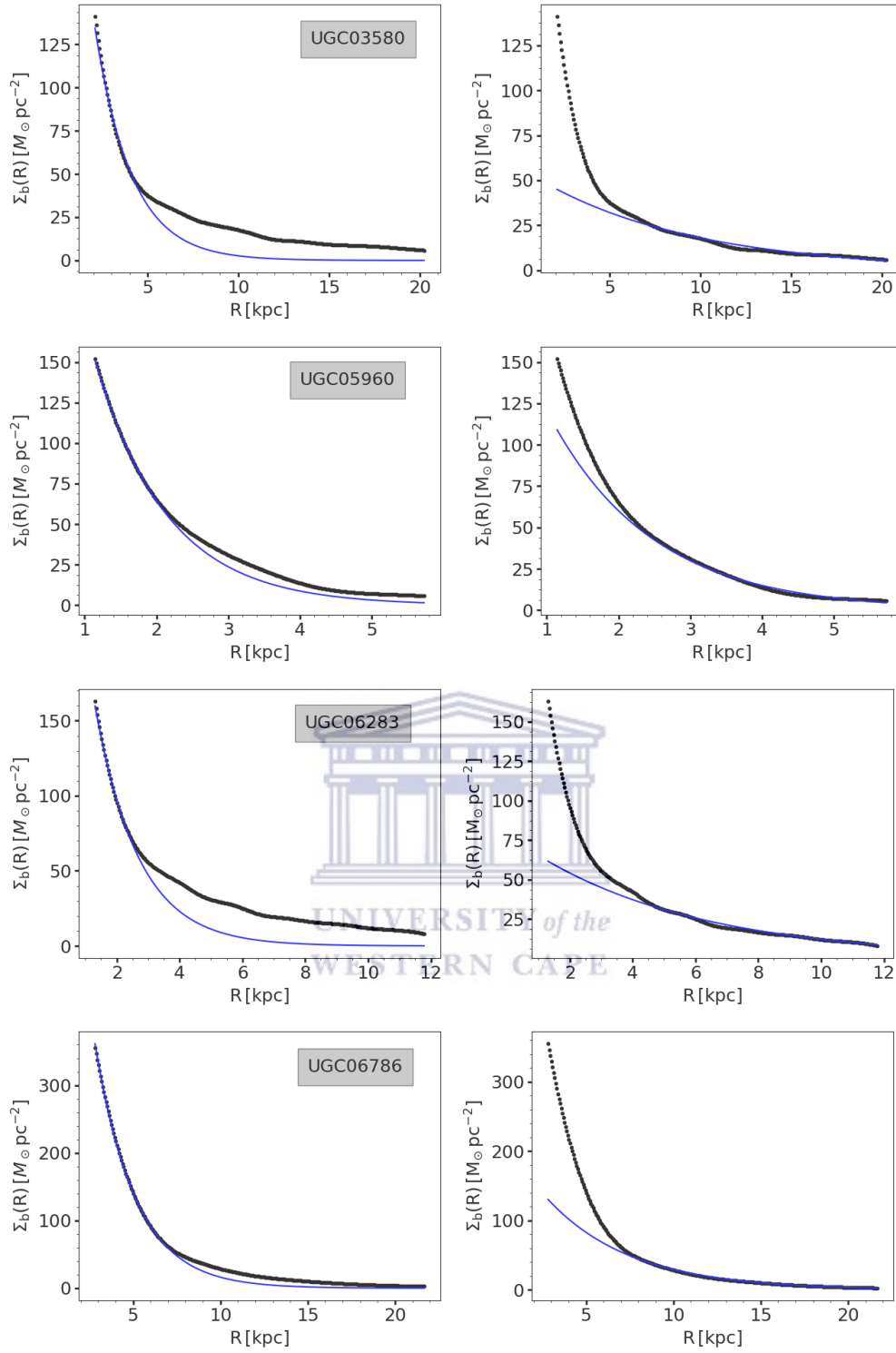


Figure A.5: Baryonic mass surface density fitted with an exponential function continued. See Figure A.4 caption for full details.

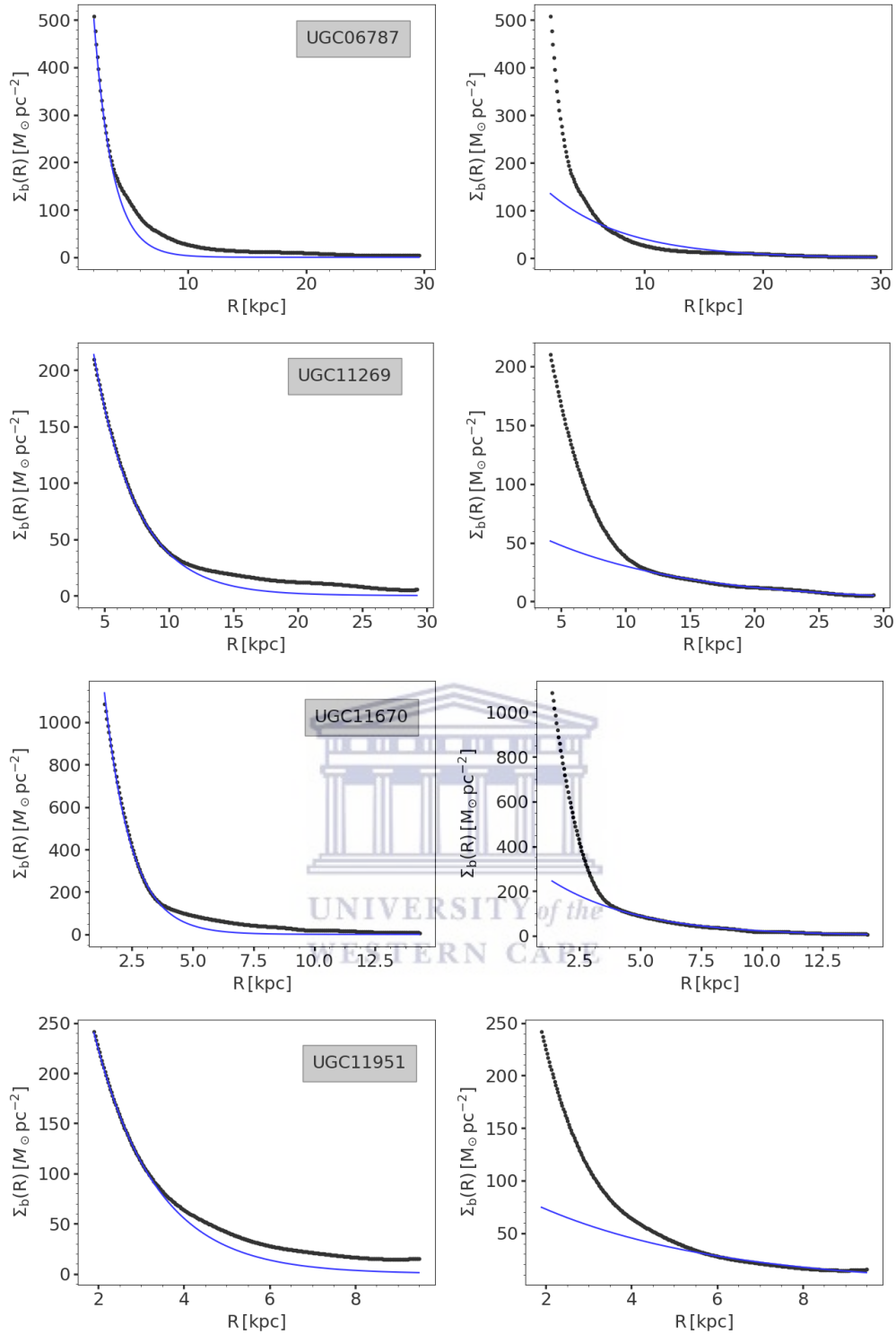


Figure A.6: Baryonic mass surface density fitted with an exponential function continued. See Figure A.4 caption for full details.

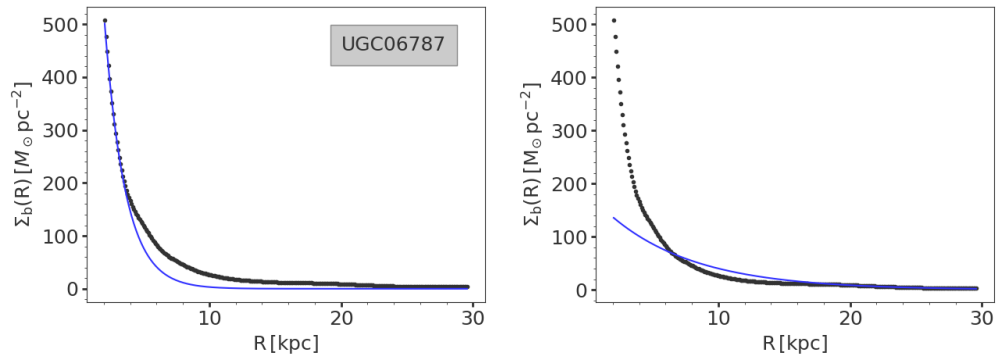


Figure A.7: Baryonic mass surface density fitted with an exponential function continued. See Figure A.4 caption for full details.



Appendix B

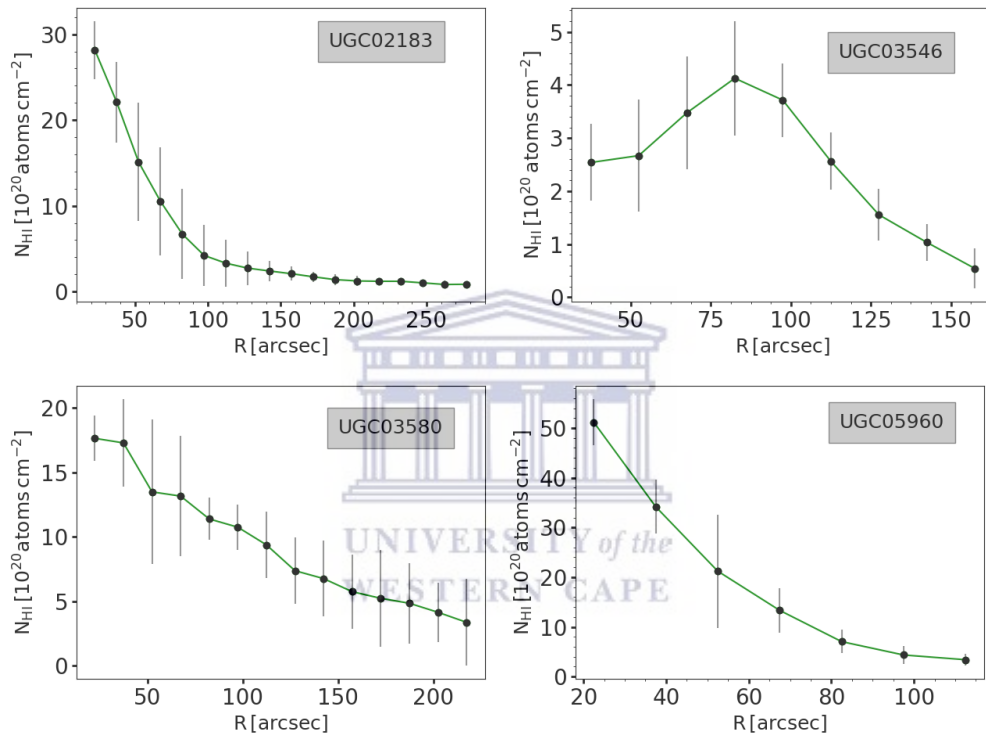


Figure B.1: Filled black circles represents an average HI column density in a ring of width 15 arcsec. Grey error bars represented the difference between the 75th and 25th percentile of the data in a ring. These profiles were used with the tilted ring model using GALMOD routine in GIPSY in order to generate full three-dimensional model cubes that are comparable to the data.

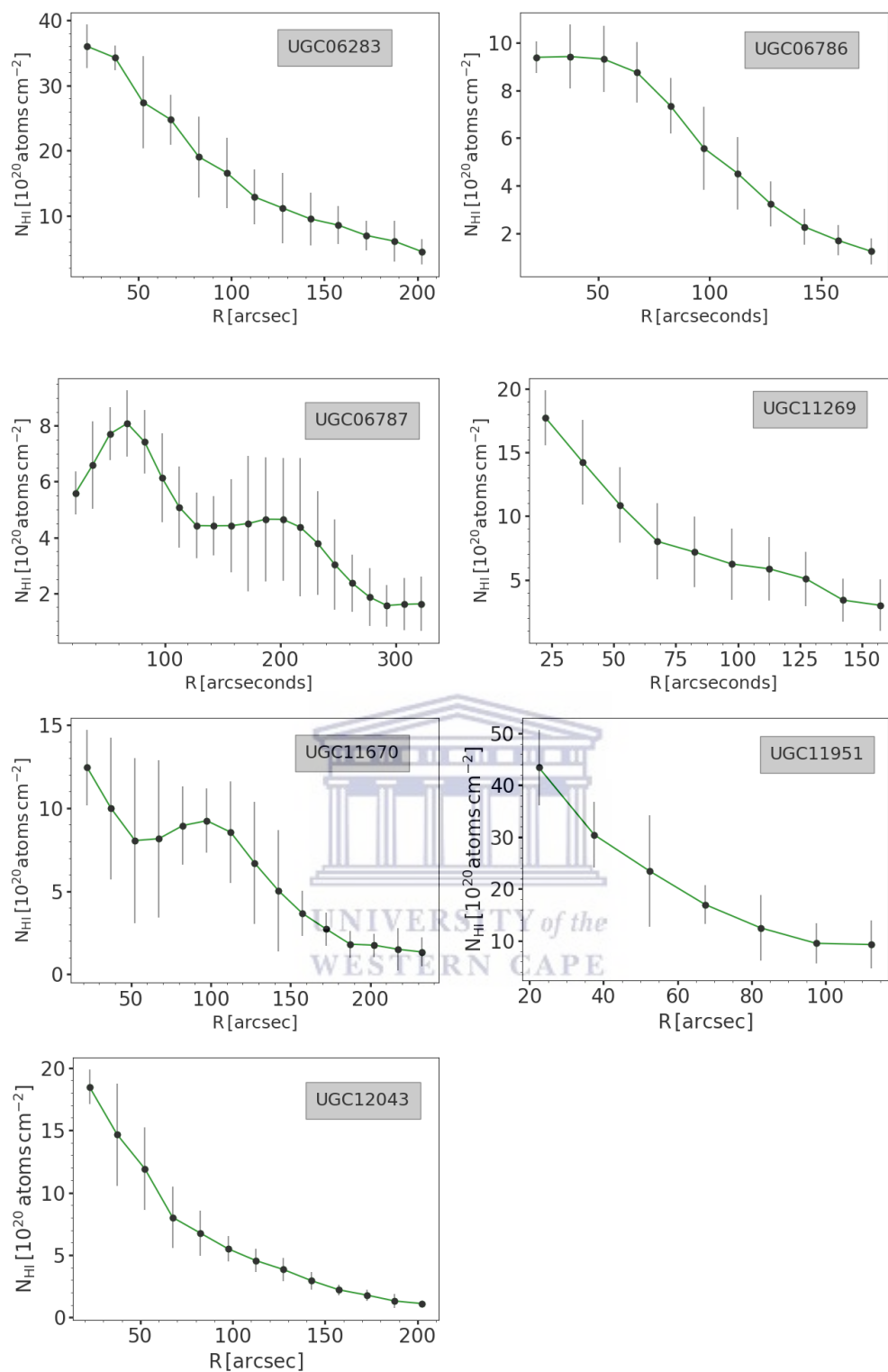


Figure B.2: HI column density profiles continued. See Figure B.1 caption for full details.

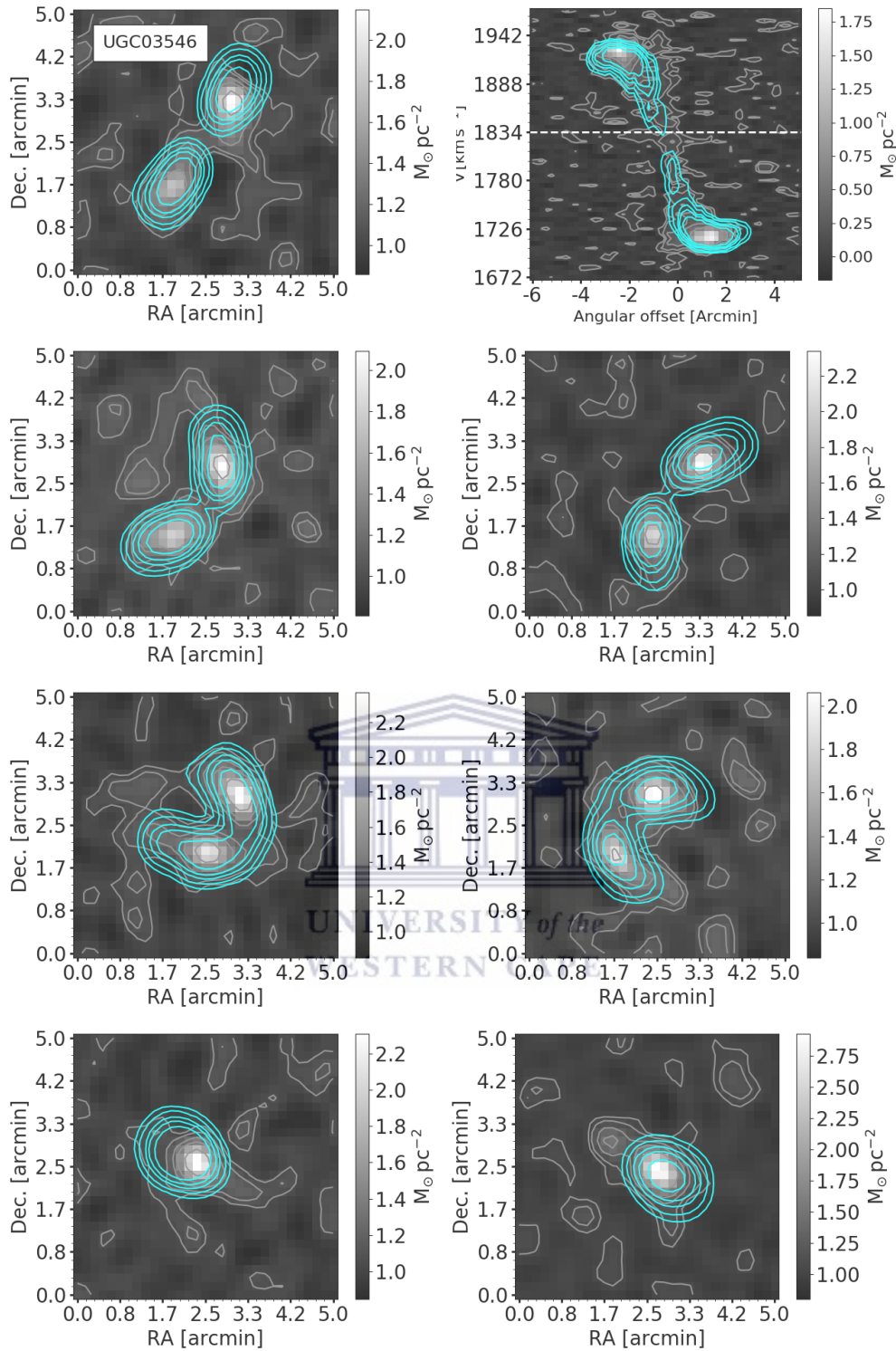


Figure B.3: Channel maps comparison between WHISP data (grey scale and grey contours) and the model cubes generated using GALMOD (cyan contours). The contour levels are: 1σ , 2σ , 4σ , 6σ , 10σ , where σ is the noise level for each galaxy quantified in section 2.3 chapter 2. From top to bottom, left to right, the first seven panels shows the comparison at radial velocities of $V_{\text{sys}} \pm \frac{i \cdot V_{\text{max}}}{3}$, where $i = 0, 1, 2, 3$ and V_{max} is the maximum velocity from the measured rotation curve. The last panel shows the comparison for a position-velocity slice extracted along the major axis of the galaxy.

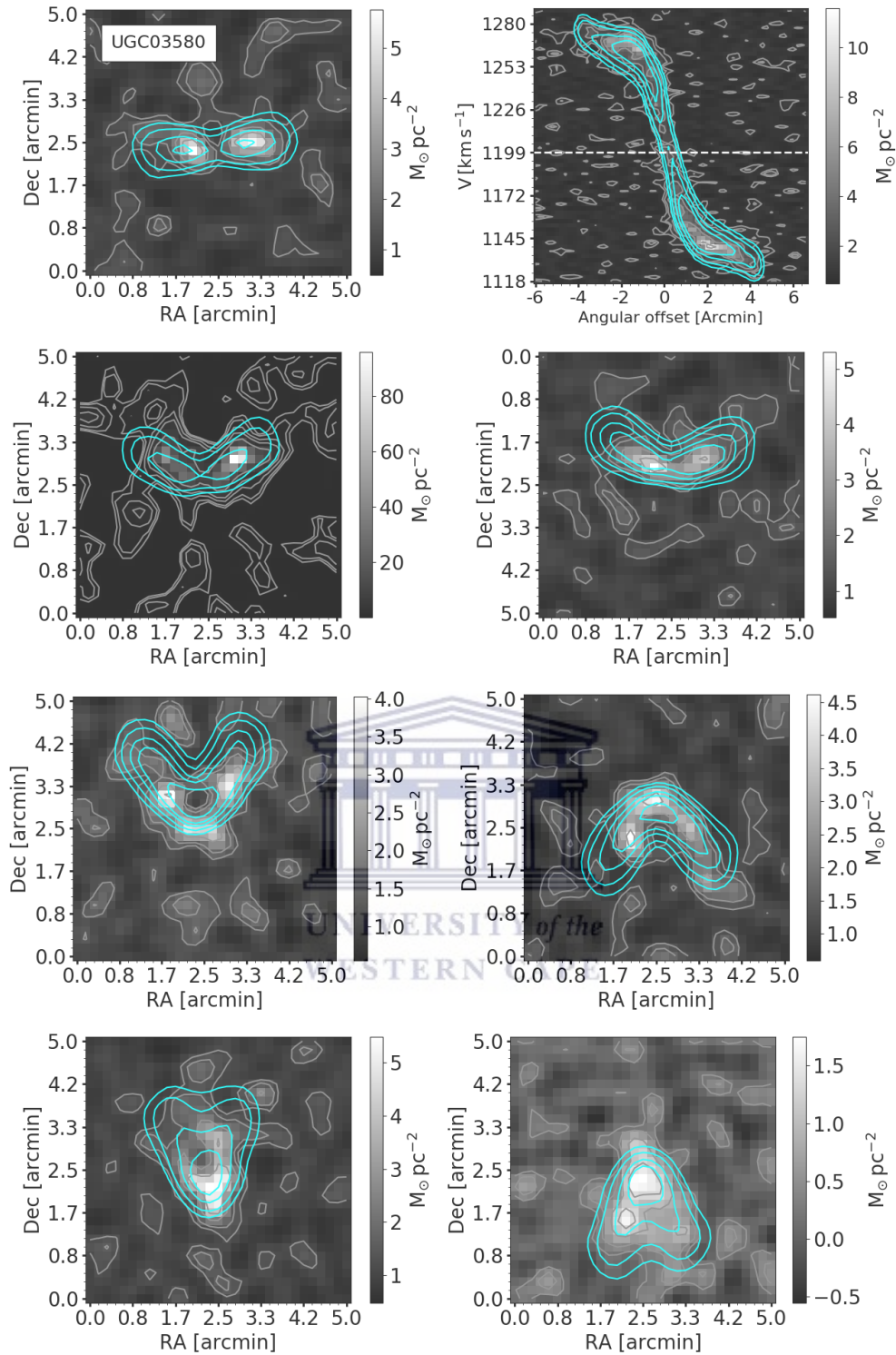


Figure B.4: Model-data comparison for UGC03580: channel maps & pv-slices. See Figure B.3 caption for full details.

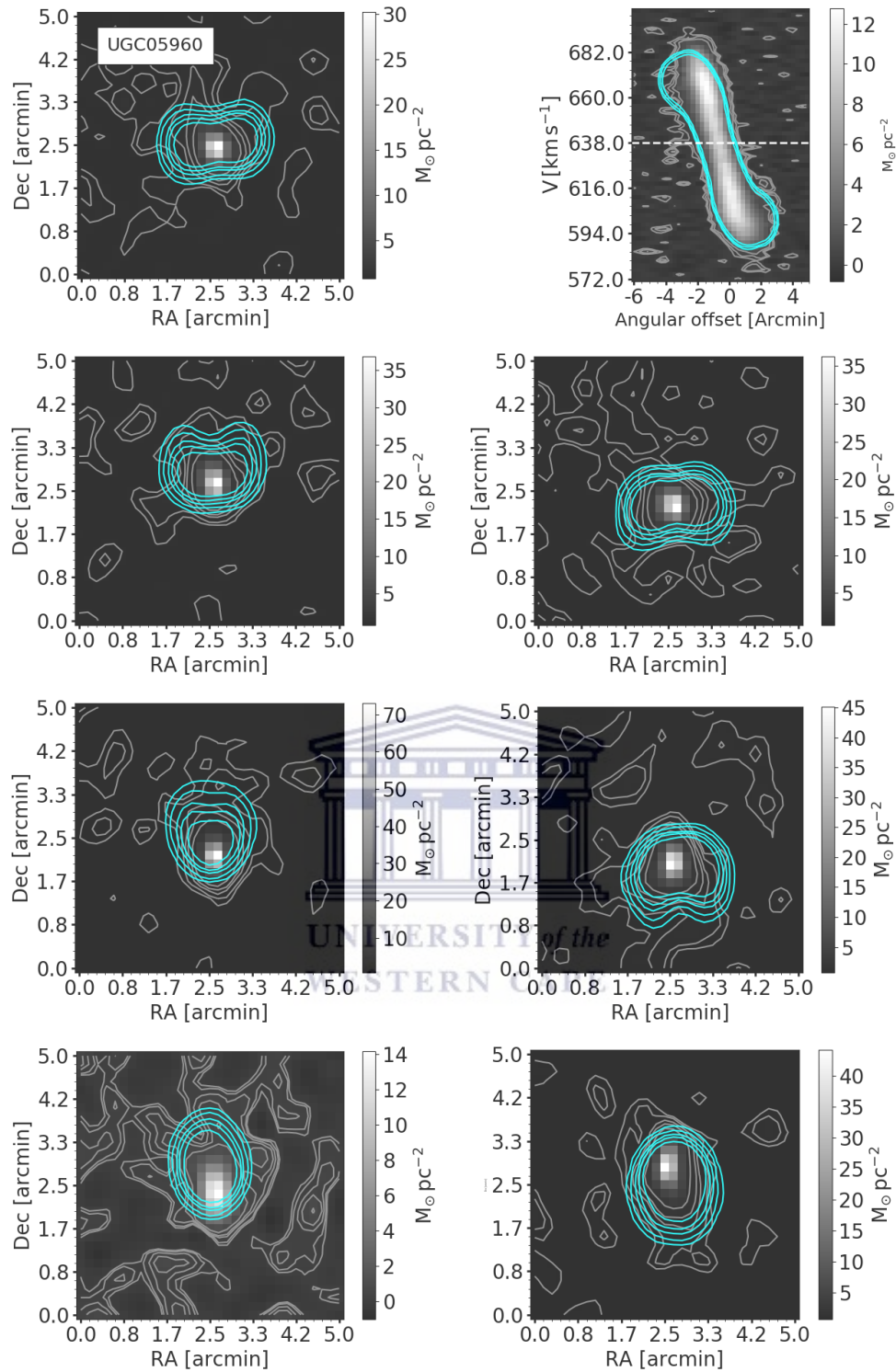


Figure B.5: Model-data comparison for UGC05960: channel maps & pv-slices. See Figure B.3 caption for full details.

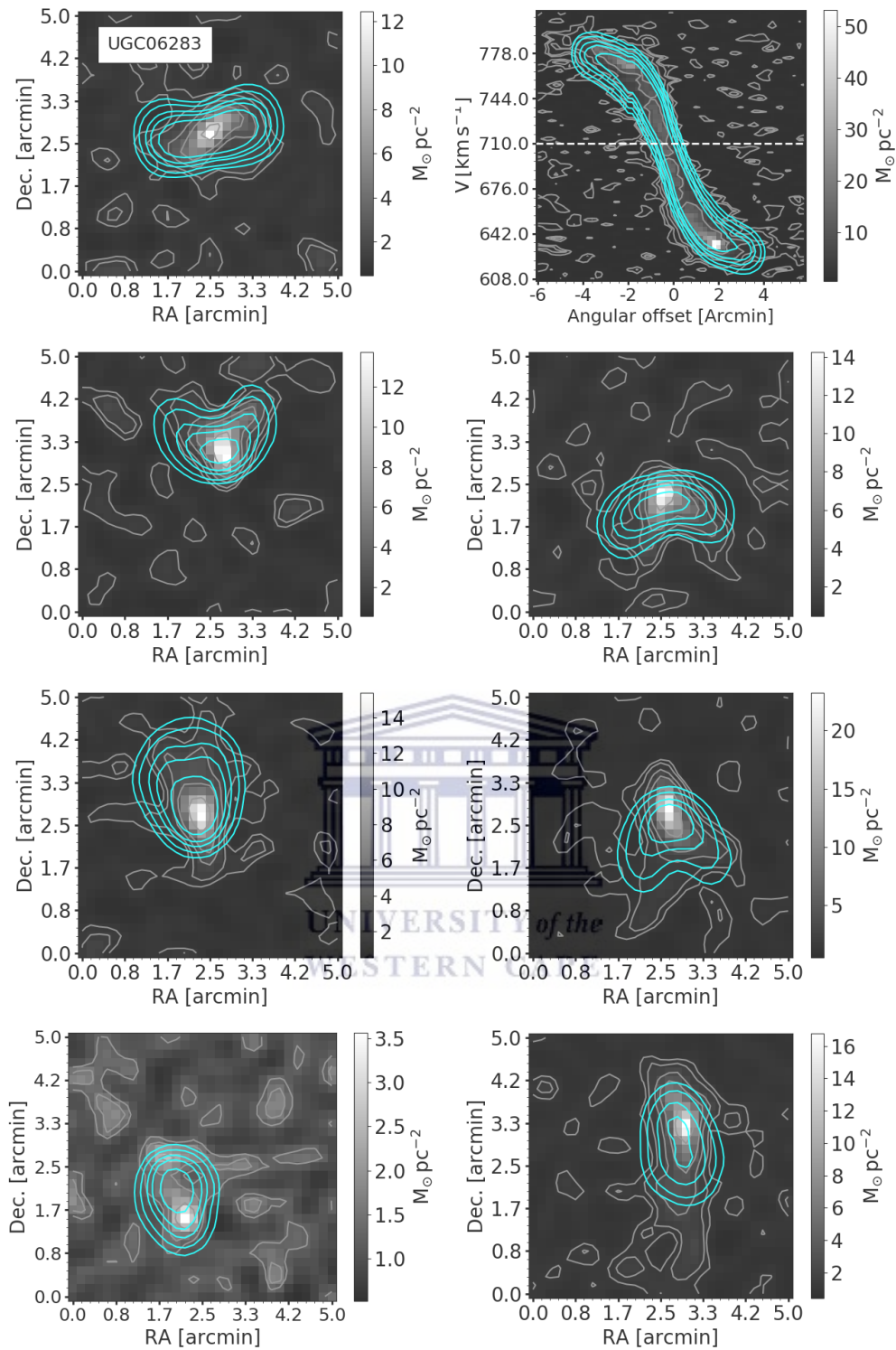


Figure B.6: Model-data comparison for UGC06283: channel maps & pv-slices. See Figure B.3 caption for full details.

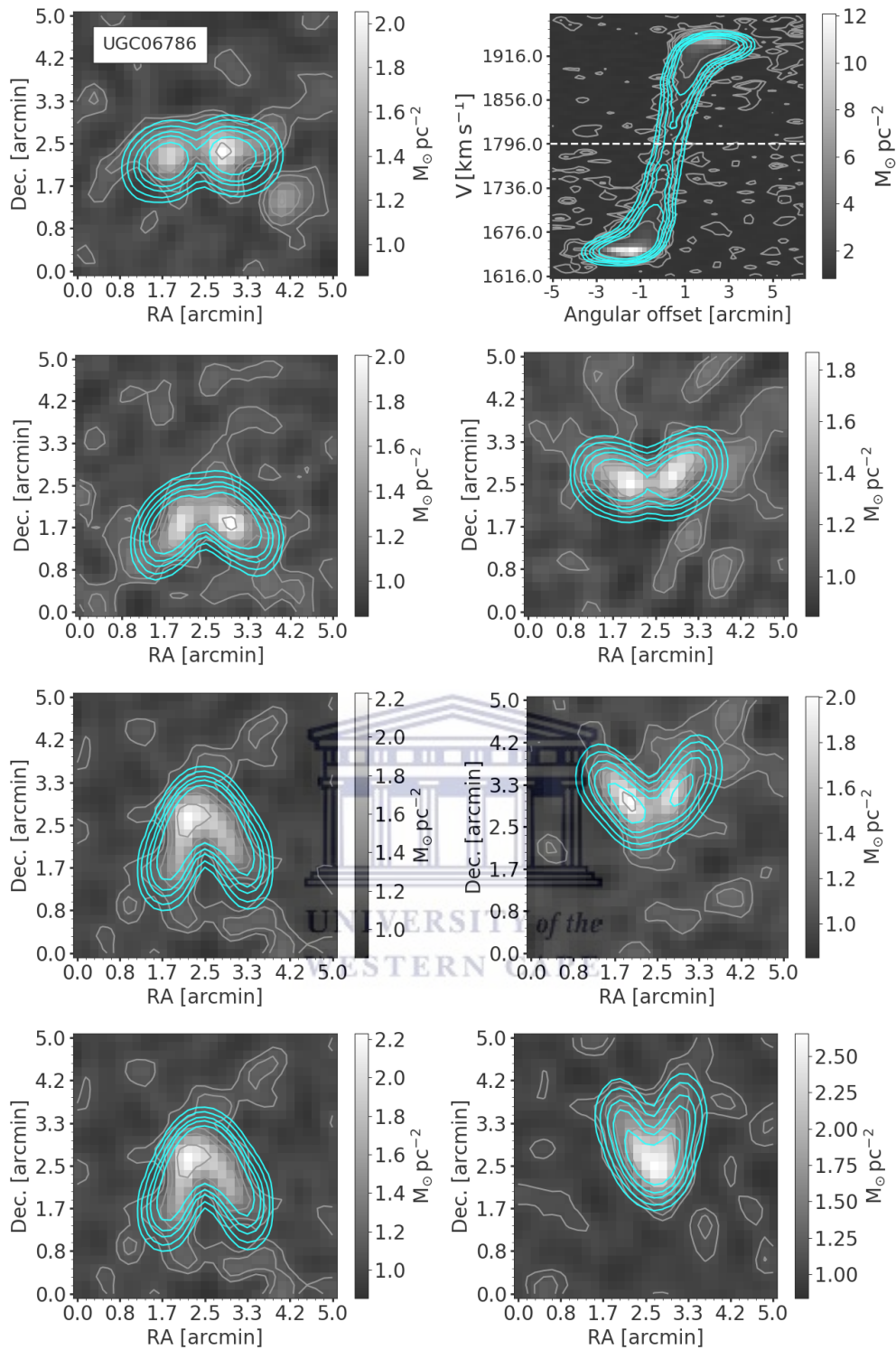


Figure B.7: Model-data comparison for UGC06786: channel maps & pv-slices. See Figure B.3 caption for full details.

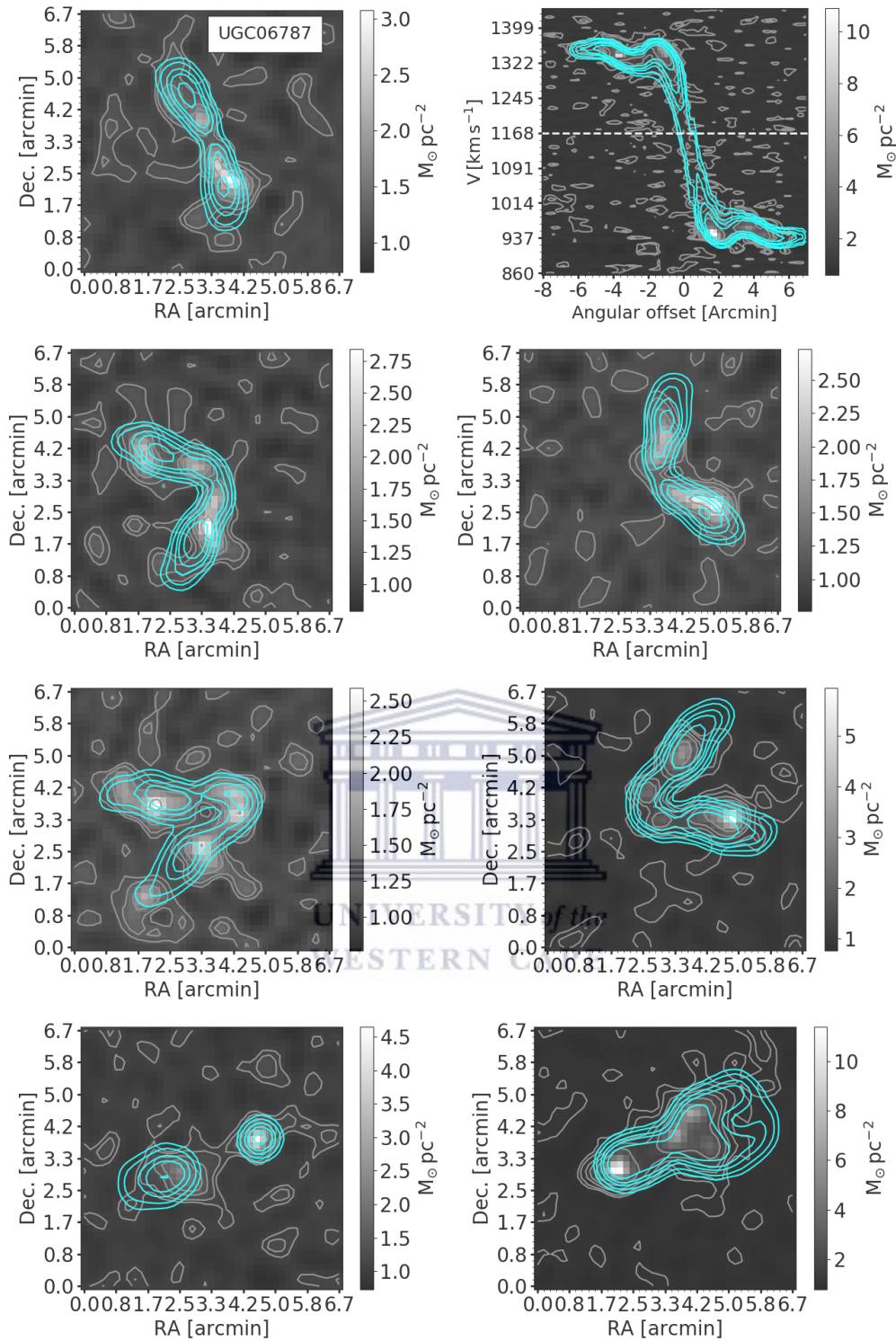


Figure B.8: Model-data comparison for UGC06787: channel maps & pv-slices. See Figure B.3 caption for full details.

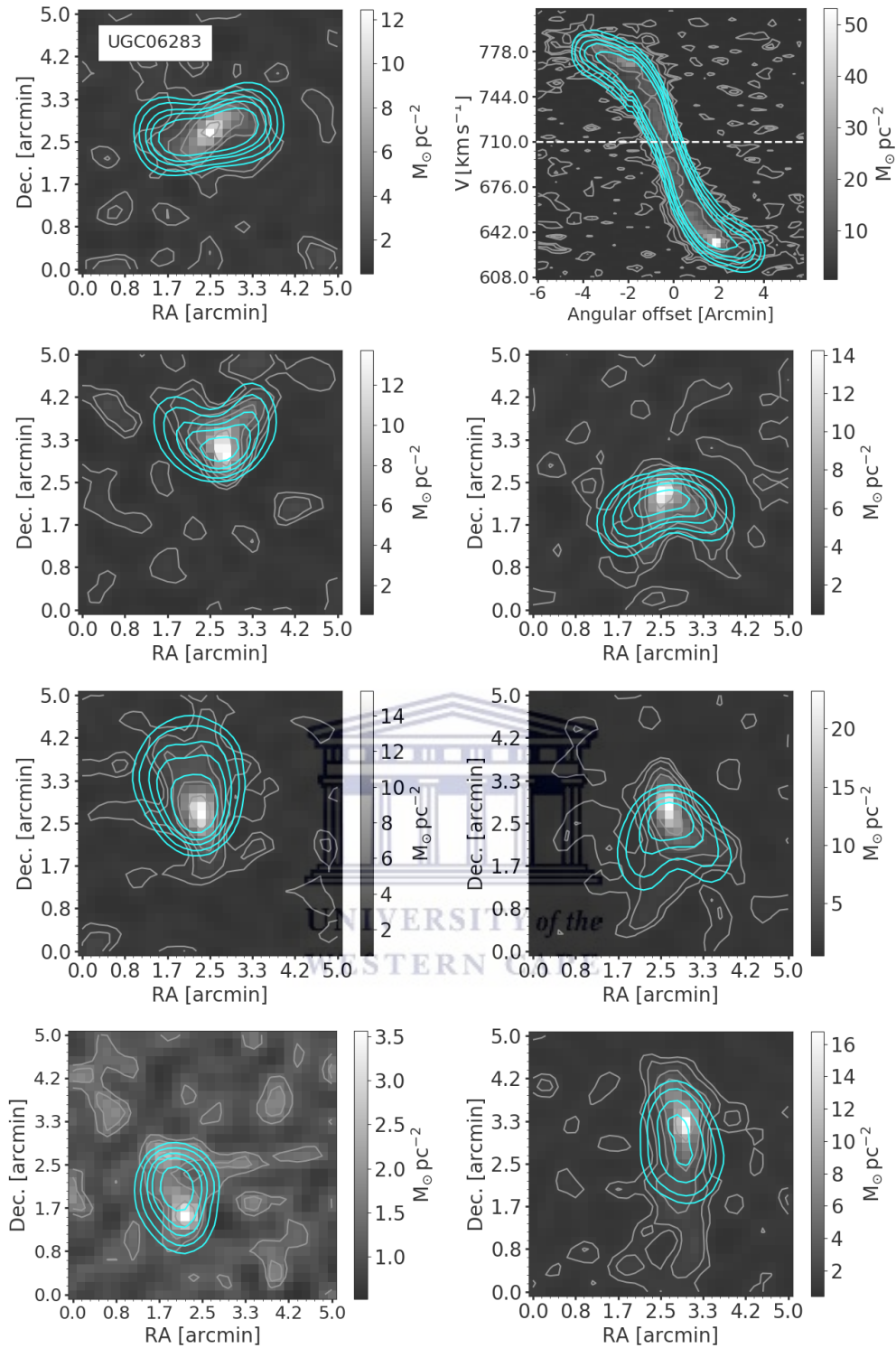


Figure B.9: Model-data comparison for UGC06283: channel maps & pv-slices. See Figure B.3 caption for full details.

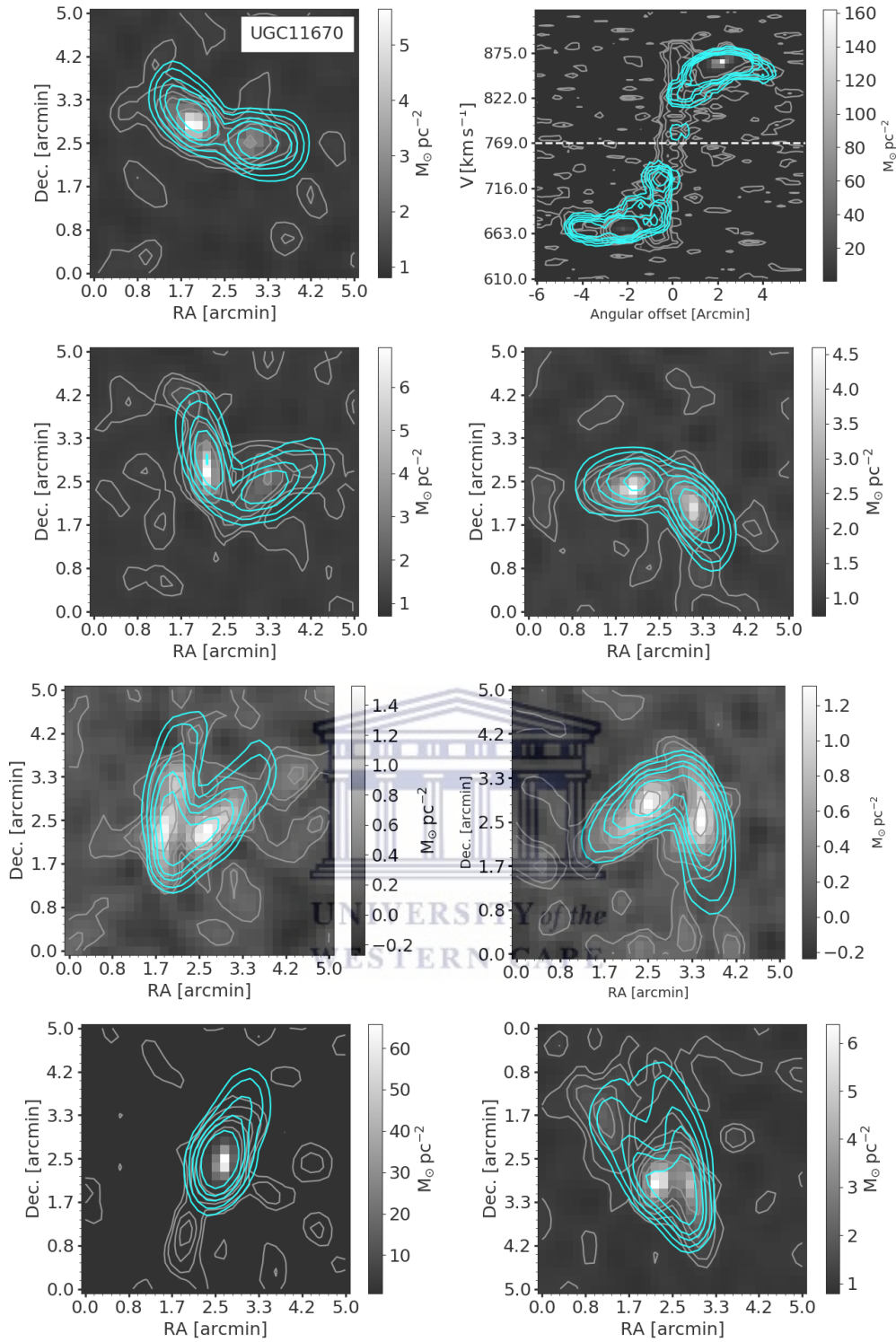


Figure B.10: Model-data comparison for UGC11670: channel maps & pv-slices. See Figure B.3 caption for full details.

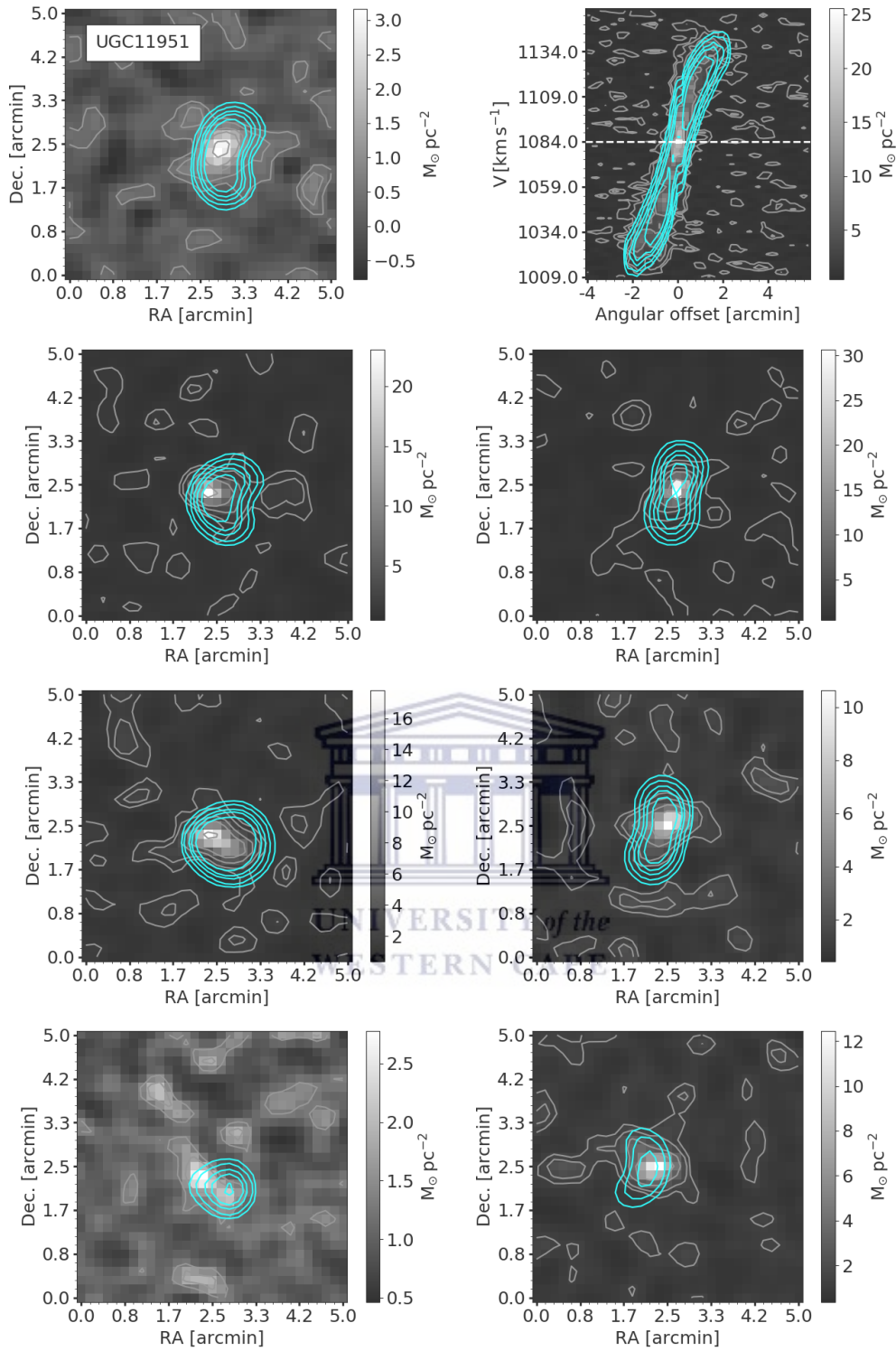


Figure B.11: Model-data comparison for UGC11951: channel maps & pv-slices. See Figure B.3 caption for full details.

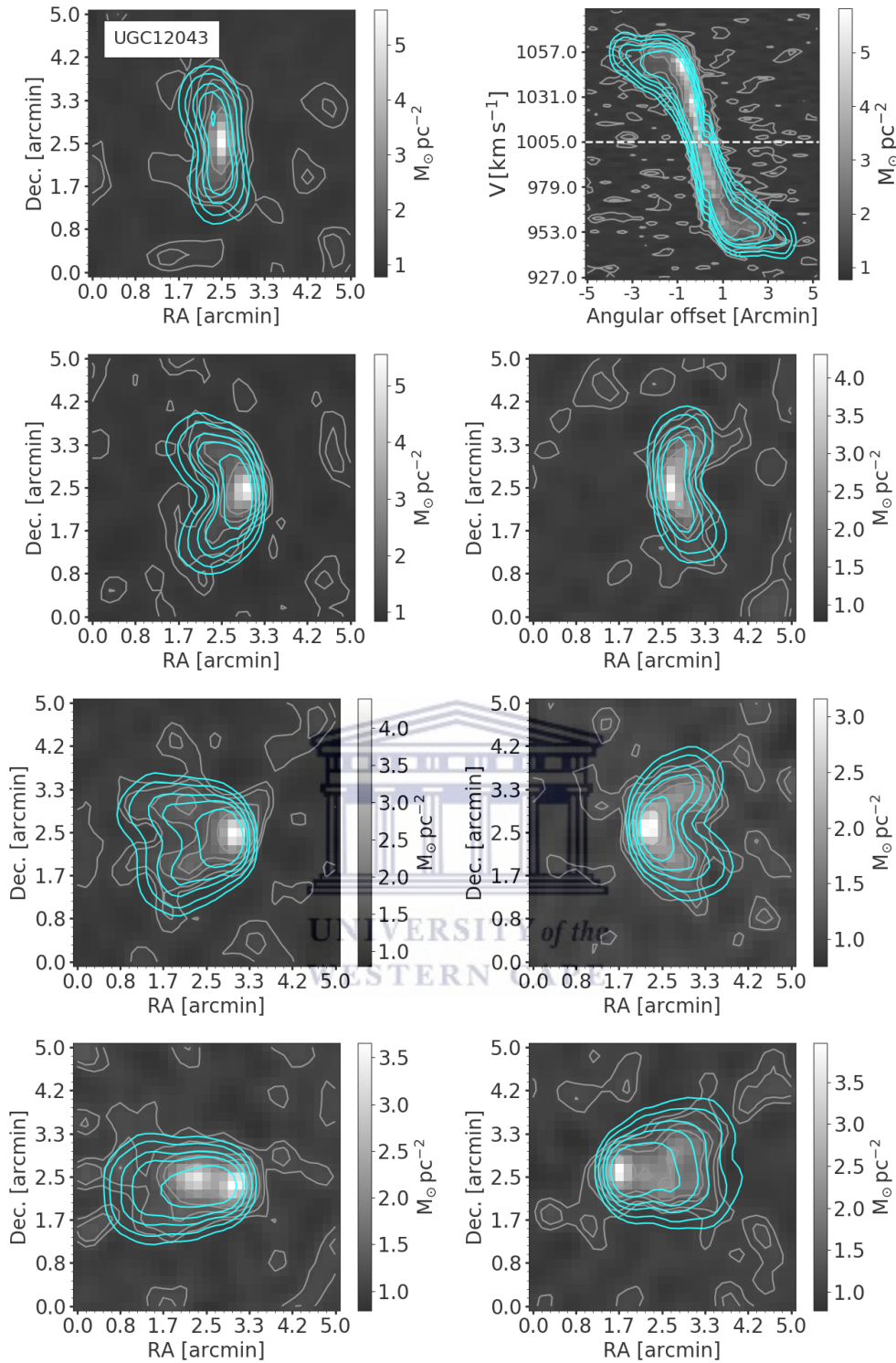


Figure B.12: Model-data comparison for UGC12043: channel maps & pv-slices. See Figure B.3 caption for full details.

Bibliography

- Abraham, R. G. and van den Bergh, S. (2001), ‘The morphological evolution of galaxies’, *Science* **293**(5533), 1273–1278.
- Butler, K. M., Obreschkow, D. and Oh, S.-H. (2016), ‘Angular momentum of dwarf galaxies’, *The Astrophysical Journal Letters* **834**(1), L4.
- Casertano, S. and Van Gorkom, J. (1991), ‘Declining rotation curves-the end of a conspiracy?’, *The Astronomical Journal* **101**, 1231–1241.
- Chowdhury, A. and Chengalur, J. N. (2017), ‘Angular momentum content in gas-rich dwarf galaxies’, *Monthly Notices of the Royal Astronomical Society* **467**(4), 3856–3863.
- Cluver, M., Jarrett, T. H., Hopkins, A. M., Driver, S., Liske, J., Gunawardhana, M., Taylor, E., Robotham, A., Alpaslan, M., Baldry, I. et al. (2014), ‘Galaxy and mass assembly (gama): mid-infrared properties and empirical relations from wise’, *The Astrophysical Journal* **782**(2), 90.
- Côté, S., Carignan, C. and Freeman, K. C. (2000), ‘The various kinematics of dwarf irregular galaxies in nearby groups and their dark matter distributions’, *The Astronomical Journal* **120**(6), 3027.
- De Blok, W., Adams, E., Amram, P., Athanassoula, E., Bagetakos, I., Balkowski, C., Bershady, M., Beswick, R., Bigiel, F., Blyth, S.-L. et al. (2017), ‘An overview of the mHongoose survey: Observing nearby galaxies with MeerKAT’, *arXiv preprint arXiv:1709.08458* .
- Elson, E. (2017), ‘The relation between specific baryon angular momentum and mass for a sample of nearby low-mass galaxies with resolved H I kinematics’, *Monthly Notices of the Royal Astronomical Society* **472**(4), 4551–4562.
- Fall, S. M. (1983), Galaxy formation: some comparisons between theory and observation, in ‘Symposium-International Astronomical Union’, Vol. 100, Cambridge University Press, pp. 391–399.

- Fall, S. M. and Romanowsky, A. J. (2013), ‘Angular momentum and galaxy formation revisited: effects of variable mass-to-light ratios’, *The Astrophysical Journal Letters* **769**(2), L26.
- Izotov, Y., Thuan, T. and Guseva, N. (2014), ‘A new determination of the primordial he abundance using the he i $\lambda 10830$ \AA emission line: cosmological implications’, *Monthly Notices of the Royal Astronomical Society* **445**(1), 778–793.
- Kamphuis, J., Sijbring, D. and Van Albada, T. (1995), ‘Global hi profiles of spiral galaxies’, *arXiv preprint astro-ph/9511024* .
- Kent, S. M. (1985), ‘Ccd surface photometry of field galaxies. ii-bulge/disk decompositions’, *The Astrophysical Journal Supplement Series* **59**, 115–159.
- Kormendy, J. (1990), Did elliptical galaxies form by mergers or by dissipative collapse?, *in* ‘Dynamics and Interactions of Galaxies’, Springer, pp. 499–502.
- Kurapati, S., Chengalur, J. N., Pustilnik, S. and Kamphuis, P. (2018), ‘Angular momentum of dwarf galaxies’, *Monthly Notices of the Royal Astronomical Society* .
- McGaugh, S. S. and Schombert, J. M. (2014), ‘Color-mass-to-light-ratio relations for disk galaxies’, *The Astronomical Journal* **148**(5), 77.
- Noordermeer, E., Van Der Hulst, J., Sancisi, R., Swaters, R. and Van Albada, T. (2005), ‘The westerbork hi survey of spiral and irregular galaxies-iii. hi observations of early-type disk galaxies’, *Astronomy & Astrophysics* **442**(1), 137–157.
- Noordermeer, E., Van Der Hulst, J., Sancisi, R., Swaters, R. and Van Albada, T. (2007), ‘The mass distribution in early-type disc galaxies: declining rotation curves and correlations with optical properties’, *Monthly Notices of the Royal Astronomical Society* **376**(4), 1513–1546.
- Obreschkow, D. and Glazebrook, K. (2014), ‘Fundamental mass-spin-morphology relation of spiral galaxies’, *The Astrophysical Journal* **784**(1), 26.
- Peebles, P. (1969), ‘Origin of the angular momentum of galaxies’, *The Astrophysical Journal* **155**, 393.
- Rogstad, D., Lockhart, I. and Wright, M. (1974), ‘Aperture-synthesis observations of hi in the galaxy m83’, *The Astrophysical Journal* **193**, 309–319.
- Romanowsky, A. J. and Fall, S. M. (2012), ‘Angular momentum and galaxy formation revisited’, *The Astrophysical Journal Supplement Series* **203**(2), 17.

- Serra, P., de Blok, W., Bryan, G., Colafrancesco, S., Dettmar, R.-J., Frank, B., Govoni, F., Józsa, G., Kraan-Korteweg, R., Loubser, S. et al. (2017), ‘The meerkat fornax survey’, *arXiv preprint arXiv:1709.01289* .
- Steinmetz, M. and Navarro, J. F. (2002), ‘The hierarchical origin of galaxy morphologies’, *New Astronomy* **7**(4), 155–160.
- Swaters, R., Sancisi, R., Van Albada, T. and Van Der Hulst, J. (2009), ‘The rotation curves shapes of late-type dwarf galaxies’, *Astronomy & Astrophysics* **493**(3), 871–892.
- Taylor, A. R. and Jarvis, M. (2017), Mightee: The meerkat international ghz tiered extragalactic exploration, in ‘IOP Conference Series: Materials Science and Engineering’, Vol. 198, IOP Publishing, p. 012014.
- Toomre, A. and Toomre, J. (1972), ‘Galactic bridges and tails’, *The Astrophysical Journal* **178**, 623–666.
- Van der Hulst, J., Terlouw, J., Begeman, K., Zwitter, W., Roelfsema, P., Worrall, D., Biemesderfer, C. and Barnes, J. (1992), Astronomical data analysis software and systems i, in ‘ASP Conf. series’, number 25, p. 131.
- Van der Hulst, J., Van Albada, T. and Sancisi, R. (2001), The westerbork hi survey of irregular and spiral galaxies, whisp, in ‘Gas and Galaxy Evolution’, Vol. 240, p. 451.
- Verheijen, M. (1997), The ursa major cluster of galaxies: TF-relations and dark matter, PhD thesis. date submitted:1997 Rights: University of Groningen.
- Verheijen, M. A. (2001), ‘The ursa major cluster of galaxies. v. hi rotation curve shapes and the tully-fisher relations’, *The Astrophysical Journal* **563**(2), 694.
- Walter, F. and Brinks, E. (1999), ‘Holes and shells in the interstellar medium of the nearby dwarf galaxy ic 2574’, *The Astronomical Journal* **118**(1), 273.
- Walter, F., Brinks, E., De Blok, W., Bigiel, F., Kennicutt Jr, R. C., Thornley, M. D. and Leroy, A. (2008), ‘Things: The hi nearby galaxy survey’, *The Astronomical Journal* **136**(6), 2563.